



Universidad de Concepción  
Dirección de Postgrado  
Facultad de Ciencias Físicas y Matemáticas  
Programa de Doctorado en Ciencias Físicas

# **Merging Systems in Isolated Environments**

## **(Galaxias Cercanas Colisionando en Ambientes Aislados)**

Tesis para optar al grado de Doctor  
en Ciencias Físicas

POR

**Paula Erika Jocelyn Calderón Castillo**

**Concepción - Chile  
Diciembre 2018**

Profesor Guía: Neil Mark Nagar  
Departamento de Astronomía  
Facultad de Ciencias Físicas y Matemáticas  
Universidad de Concepción

*To my Family and Friends ...*



---

# Agradecimientos

I would like to thank Dr. Neil Nagar for being my supervisor and helping us in our unique situation. I also would like to thank Dr. Sukyoung Yi for accepting me in his group at Yonsei, and being so welcoming and helpful during my PhD. Additionally, I would like to thank Dr. Rodrigo Reeves for always being so kind and for accepting being part of my committee. To Neil, Sukyoung, and Rodrigo, thank you for being so helpful in revising and commenting on my thesis.

Special thanks to every person who accompanied me in my journey, who were always beside me in this tough but rewarding adventure / Agradecimientos especiales a cada persona que me ha acompañado en este viaje, quienes han estado junto a mí en esta empinada, empedrada, pero también satisfactoria aventura.

Primero me gustaría agradecer a mi familia. A mi hermano, *Miguel Arturo, miTo*, que llegó a mi existencia a revolucionar mis objetivos de vida. Siempre te lo he dicho, agradezco que hayas llegado a mi vida, siempre la llenas de fuerza, esperanza, enseñanzas, amor y perseverancia. Agradezco estar junto a ti y ver cómo creces. A mi hermana, *Estefanía*, muchas gracias por todo el apoyo y ánimo que siempre me has dado. Me enorgullece ser tu hermana y estaré siempre junto a ti. A mis padres, *Miguel y Erika*, por todo el apoyo que me han dado, ahora y a lo largo de mi vida. Les agradezco todo lo que me han enseñado. A mis sobrinos, *Benji, Cris y Salvi*, gracias por ser siempre tan amorosos conmigo. Mi querida familia, los amo hasta el infinito y más allá.

I would like to thank to my "new" family. To *Rory*, thank you for always being there for me, for accepting me as your life partner and for accompanying me in all the different experiences we have gone through together these last 9 years. My PhD would had being a tougher journey without you. I love you from here to the CMB and beyond.

To *Jan and Pete*, for being so caring of me and encouraging me every time. To *Rowan*, for always being so kind to me. To *Kate*, for being so thoughtful and supportive. I really appreciate all that you guys do for us. Thank you.

No pueden faltar mis especiales agradecimientos a mis amigos de la vida. A *Pame R.*, por ser tú, por estar ahí cuando lo he necesitado, por nuestros horarios coincidentes y necesarias conversaciones. A *Gustavo*, por sus consejos, experiencias y ayuda estratégica, gracias por el ánimo y apoyo siempre. A *Pame*, por sus consejos y particulares conversaciones, siempre se disfrutan y aprendo de ellas. A *Reneé*, por sus consejos y palabras de ánimo que siempre me han ayudado. A *Pame y Reneé*, por compartir su hogar conmigo y hacerme sentir como en casa y a *Gali*, por ser un cargador de pilas irremplazable. A *Clau*, por sus consejos, conversaciones y oncecitas, gracias por compartir tu vida y familia conmigo. A *Gaby*, por sus palabras y juntas esporádicas, que siempre me dejan animada. A *Fabi*, gracias por tu apoyo, ayuda y preocupación. A *Vania*, por

su preocupación, ánimo y cariño. A *Guille*, por su ánimo y buena onda, siempre. To *Hyein* (혜인), thank you for always being so kind and willing to help, thank you for sharing your friendship with me. 감사합니다 ~ . A *Jeanette*, gracias por siempre estar ahí, por hacerme sentir mejor siempre que he estado media triste. Gracias por tratarme y preocuparse por mí como si fuéramos familia, ya que así también yo la considero. A todos ellos, gracias por su ánimo y apoyo incondicional. Los quiero a montones, amigos de la vida.

To *Luca and Barbara*, thank you for your support and for being always so kind to me. Thank you for helping me in my PhD process. To *Barbara*, thank you for being so enthusiastic to work with me, I really appreciate it. To *Luca*, thank you for your help on my first first-author paper, I'm not sure I would have survived until now without your help. Thank you both for being such great friends.

To *André*, thank you for your advice and for our long and deep conversations, I always enjoy them.

A *Roger*, muchas gracias por siempre darme los mejores consejos en el tiempo que más los he necesitado.

A *Mary, Cristián, Maty y Cona*, muchas gracias por todo su cariño y hospitalidad. Los quiero un montón, ahora y siempre.

To *Tom*, for his supportive and encouraging words. Thank you for your help and friendship.

To *Yu-Yen*, thank you for being so kind since the beginning and willing to help me in everything I needed.

A *Sole y Marce*, muchísimas gracias por toda su ayuda y por siempre hacer lo posible para que todo funcione.

Agradezco el financiamiento recibido de CONICYT a través de la Beca Doctorado Nacional, la cual recibí durante la mayor parte de mi doctorado.

# Resumen

Ya es de conocimiento general que ciertas galaxias masivas aumentan su tasa de formación estelar (SFR por sus siglas en inglés) al pasar por procesos de colisión con galaxias de tamaños similares. Estos aumentos pueden ser de hasta 100 veces la SFR de galaxias no perturbadas, pero con la misma masa estelar ( $M_*$ ). Estudios anteriores encontraron que el tamaño de esta alza en formación estelar (SF) está relacionada con la morfología y la distancia a la que se encuentra la galaxia compañera. Esta misma tendencia se observa en la fracción de galaxias con AGN, donde mientras más cerca se encuentre la galaxia compañera, mayor será la fracción de galaxias con AGN encontrada.

Nuestro objetivo principal es analizar esta alza de SF y fracción de AGN acorde a su evolución en el proceso de colisión, usando una secuencia más acorde con las etapas cronológicas del proceso. Además, otro de nuestros propósitos es determinar la relación entre el alza en SF en galaxias colisionando y la morfología de éstas.

Aprovechando los valores de  $M_*$  y SFR de  $\sim 600$  galaxias cercanas ( $z < 0.1$ ) colisionando, obtenidos en este estudio, calculamos la distancia que tiene cada una de nuestras galaxias en proceso de colisión con la Secuencia Principal de formación estelar (MS por sus siglas en inglés,  $sSFR/sSFR_{MS}$ ). Nos referimos a esta distancia como "SF mode". Luego, analizamos como la SF mode varía a lo largo del proceso de colisión, dependiendo de la morfología y la  $M_*$ . Asimismo, analizamos el contenido de AGN en nuestras galaxias usando múltiples diagnósticos, unos basados en fracciones de líneas de emisión y otro basado en colores de WISE.

Observamos que, generalmente, las galaxias en proceso de colisión muestran un SF mode gobernado por su propia morfología. Esto significa que, galaxias espirales tienden a tener altos SF mode, mientras galaxias extremadamente perturbadas (HD por sus siglas en inglés) muestran aún más altos SF mode (las respectivas medianas son: +0.8 dex y +1.0 dex sobre la MS). De forma contraria, galaxias elípticas y lenticulares muestran los más bajos SF mode, como es de esperar para este tipo de morfología. Aún así, estas galaxias muestran SF mode más elevados comparados con galaxias elípticas y lenticulares que no están en proceso de colisión. Por ejemplo, la mediana del SF mode para este tipo de galaxias está dentro del límite de  $1-\sigma$  desde la MS; y esto se observa incluso antes que las galaxias se hayan fusionado, formando un solo objeto. En general, observamos que el SF mode tiende a aumentar gradualmente mientras las galaxias avanzan en el proceso de colisión. Además, encontramos que la fracción de galaxias con AGN tiende a disminuir a lo largo del proceso.

En conclusión, encontramos que el proceso de colisión ayuda a aumentar la SF en galaxias de todas las morfologías. Para galaxias elípticas y lenticulares, esto podría sugerir que algo de

gas existe antes del proceso, el cual es incitado para formar estrellas por las interacciones tidales. Además, como esta alza en SFR continúa a lo largo del proceso de colisión, sugiere que este aumento tiene un periodo de duración largo, contrario a lo predicho por simulaciones. Por otro lado, la disminución en la fracción de galaxias con AGN podría sugerir que el gas que alimenta el agujero negro supermasivo, sólo cae al agujero en etapas tempranas del proceso, generando un impacto mucho menor en las etapas de fusión (tardías). Es importante notar que la baja fracción de galaxias con AGN puede deberse a la obscuración por polvo en las galaxias, aunque no observamos cambios en la tasa de polvo, ni en la etapa del proceso de colisión.



# Abstract

It is now well known that certain massive galaxies undergo enormous enhancements in their star formation rate (SFR) when they undergo major mergers, as high as 100 times the SFR of unperturbed galaxies of the same stellar mass ( $M_*$ ). Previous works found that the size of this boost in star formation (SF) is related to the morphology of and the proximity to the companion. The same trend has also been observed for AGN fraction, where galaxies which are closer together tend to have higher AGN fractions.

Our main goal is to analyse the SF enhancement and AGN fraction evolution during the merger process, using a more timeline-like merger sequence. Additionally, we aim to determine the relation between the SF enhancement in mergers and the morphology of the galaxies involved.

Taking advantage of the  $M_*$  and SFR of  $\sim 600$  nearby ( $z < 0.1$ ) isolated mergers obtained in this study, we calculate the distance of each of our galaxies from the star-forming main sequence (MS,  $sSFR/sSFR_{MS}$ ), which we refer to as the SF mode. We then analyse how the SF mode varies during the merger process, as a function of morphology and  $M_*$ . Additionally, we analyse the AGN content of our mergers, using multiple diagnostics based on emission line ratios and WISE colours.

We observe that, overall, merging galaxies show a SF mode that is governed by their morphology. Spirals typically show high SF mode values while highly-disturbed (HD) galaxies are generally even more enhanced (median values of +0.8 dex and +1.0 dex above the MS, respectively). On the contrary, elliptical and lenticular galaxies show the lowest SF modes, as expected. However, even they show SF enhancement compared to their unperturbed counterparts. For example, their median SF mode is just within the  $1-\sigma$  scatter of the MS, and this can occur even before the galaxies have coalesced. We see a trend for SF mode to gradually increase with increasing merger stage and we also find that the fraction of AGN observed during the merger process seem to decline towards late merger stages.

We find that mergers can significantly enhance SF in galaxies of all morphologies. For early-type galaxies, this could suggest that some gas was present prior to the merger which may be triggered to form stars by the tidal interaction. As the SF enhancement continues throughout the merger process, this suggests that the enhancement may be a long-lived event, contrary to the short star bursts seen in some models. On the other hand, the decline in AGN fraction could suggest that gas feeding of the super-massive black hole only occurs at early times and has little impact on the SF at later times. The decline in AGN fraction could also be a consequence of dust obscuration but we do not observe a change in dust fraction with merger stage.

# Contents

<b>Agradecimientos</b>	<b>iii</b>
<b>Resumen</b>	<b>v</b>
<b>Abstract</b>	<b>vii</b>
<b>List of Figures</b>	<b>xi</b>
<b>List of Tables</b>	<b>xiv</b>
<b>Motivation</b>	<b>xv</b>
<b>1 Introduction</b>	<b>1</b>
1.1 The Process of Galaxy Merging . . . . .	1
1.1.1 Star Formation Enhancement predicted by Merger Simulations . . . . .	3
1.2 The SFR- $M_*$ plane and the Main Sequence of Star Formation . . . . .	9
1.2.1 Star Formation Mode . . . . .	12
1.3 Dependence on Companion Distance and the Morphology . . . . .	12
1.4 Stellar Mass and Star Formation Rate Estimators . . . . .	16
1.4.1 Photometry using SExtractor . . . . .	18
1.4.2 SED fitting using MAGPHYS . . . . .	18
1.5 Identifying AGNs . . . . .	19
<b>2 Multi-band Photometry, Classification, Stellar Masses, and Star Formation Rates</b>	<b>24</b>
2.1 Introduction . . . . .	24
2.2 Sample and Data . . . . .	24
2.2.1 Sample Selection . . . . .	24
2.2.2 Imaging Data . . . . .	26
2.3 Results . . . . .	26
2.3.1 Galaxy and Merger Sequence Classification . . . . .	27
2.3.2 Galaxy Photometry: Problems and Solutions . . . . .	29
2.3.3 MAGPHYS: SED fitting to obtain $M_*$ and SFR of mergers . . . . .	37
2.3.4 $M_*$ and SFR comparison to other catalogs . . . . .	38
2.3.5 Testing common estimators of $M_*$ and SFR . . . . .	43
2.3.6 The Colour-Morphology Relation . . . . .	47
2.3.7 The Main Sequence and the specific star formation rate . . . . .	48



<b>3</b>	<b>Evolution of Star Formation and Accretion Activity during the Merging Process</b>	<b>51</b>
3.1	Introduction . . . . .	51
3.2	Data . . . . .	51
3.2.1	The Sample . . . . .	51
3.2.2	Merging galaxies properties . . . . .	53
3.3	Results . . . . .	53
3.3.1	Stellar Masses . . . . .	53
3.3.2	Evolution during the Merger Process: movement in the Main Sequence . . . . .	55
3.3.3	SF mode dependence on the companion's morphology . . . . .	60
3.3.4	Evolution during the Merger Process: SMBH activation . . . . .	66
<b>4</b>	<b>Discussion and Conclusions</b>	<b>73</b>
4.1	Multi-band Photometry . . . . .	73
4.2	Stellar Masses and Star Formation Rates Estimates . . . . .	74
4.3	WISE colours and sSFR . . . . .	75
4.4	SF mode and SMBH activation during the Merger Process . . . . .	75
<b>5</b>	<b>Future Work</b>	<b>78</b>
<b>6</b>	<b>Merging Systems in Isolated Environments. The Catalogue</b>	<b>79</b>
6.1	Description of the Catalogue . . . . .	79
	<b>Bibliography</b>	<b>81</b>
	<b>Appendices</b>	<b>87</b>
<b>A</b>	<b>Morphology Classification</b>	<b>88</b>
A.1	Examples of morphology . . . . .	88
<b>B</b>	<b>Survey Parameters</b>	<b>90</b>
B.1	Photometric Parameters used for the Photometry . . . . .	90
<b>C</b>	<b>Examples of Apertures</b>	<b>91</b>
C.1	Examples of Apertures depending on different SExtractor parameters . . . . .	91
<b>D</b>	<b>Testing for dependence on the Flux differences with Catalogues</b>	<b>96</b>
D.1	Testing for dependencies . . . . .	96

---

<b>E</b>	<b>MAGPHYS SED fits</b>	<b>98</b>
E.1	MAGPHYS SED fits . . . . .	98
<b>F</b>	<b>Testing for dependencies in <math>M_*</math> and SFR differences with Catalogues</b>	<b>101</b>
F.1	Testing for dependencies . . . . .	101
<b>G</b>	<b>Testing for SF mode dependence on Stellar Mass</b>	<b>103</b>
G.1	Stellar Mass bins . . . . .	103
<b>H</b>	<b>Testing for dependence on the Stellar Mass ratio of the merging galaxies</b>	<b>106</b>
H.1	Major and Minor Mergers . . . . .	106
<b>I</b>	<b>Comparison of AGN Identifiers</b>	<b>108</b>
I.1	Comparison of AGN Identifiers . . . . .	108

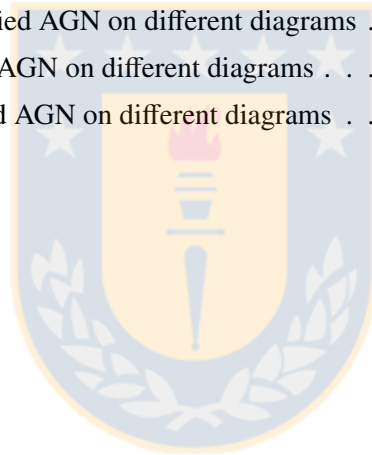


# List of Figures

1	HST images of merging galaxies . . . . .	xvi
1.1	Elliptical galaxy formed by a merger process . . . . .	2
1.2	Spiral galaxy formed by a merger process . . . . .	3
1.3	Star formation histories of simulated major mergers with and without a bulge . . . . .	4
1.4	Star formation histories of simulated minor mergers with and without a bulge . . . . .	4
1.5	Simulations of mergers with and without a black hole . . . . .	5
1.6	Star formation history and black hole growth in Di Matteo et al. (2005)'s simulations . . . . .	6
1.7	Star formation history for different mergers simulated by Di Matteo et al. (2008) . . . . .	7
1.8	Star formation history for different mergers simulated by Park et al. (2017) . . . . .	8
1.9	SFH and accretion for different mergers simulated by Park et al. (2017) . . . . .	9
1.10	Main Sequence . . . . .	10
1.11	Images of galaxies . . . . .	11
1.12	Main Sequence and compact ULIRGs . . . . .	11
1.13	ULIRG fraction according to the distance to and the morphology of its companion . . . . .	13
1.14	SFR, $M_*$ , and sSFR according to the distance to and the morphology of its companion . . . . .	14
1.15	SFR excess according to the distance to its companion . . . . .	15
1.16	AGN excess according to the distance to its companion . . . . .	15
1.17	SED fitting . . . . .	19
1.18	BPT diagnostic diagrams . . . . .	20
1.19	HeII diagnostic diagrams . . . . .	21
1.20	WISE colour-colour diagram . . . . .	22
2.1	Redshift Distribution . . . . .	25
2.2	$r$ -band Absolute Magnitude Distribution . . . . .	26
2.3	Morphology Distribution . . . . .	27
2.4	The Merger Sequence . . . . .	28
2.5	Merger Stage Distribution . . . . .	29
2.6	W1 radius Comparison . . . . .	29
2.7	Different mergers need different photometry . . . . .	30
2.8	Changing the sky-threshold and n-deblending I . . . . .	32
2.9	Example of aperture sizes from different surveys compared to our measurements . . . . .	33
2.10	Flux comparison with GALEX . . . . .	34
2.11	Flux comparison with SDSS and WISE <i>mpro</i> . . . . .	35
2.12	Flux comparison with SDSS and WISE <i>gmag</i> . . . . .	36

2.13	Flux comparison coloured by the radii ratio . . . . .	36
2.14	Stellar Mass and Star Formation Rate distribution . . . . .	37
2.15	$M_*$ and SFR comparison to limited filters . . . . .	38
2.16	$M_*$ and SFR comparison to catalogues . . . . .	39
2.17	SEDs of galaxies with the largest differences to CHANG+15 . . . . .	42
2.18	$M_*$ comparison to CLUVER14 . . . . .	44
2.19	$M_*$ comparison to B03 and T11 . . . . .	45
2.20	SFR comparison to CLUVER14 . . . . .	46
2.21	SFR comparison to the literature . . . . .	47
2.22	WISE colour-colour diagram . . . . .	48
2.23	The SFR- $M_*$ plane . . . . .	49
2.24	The sSFR - WISE colour relation for mergers . . . . .	50
3.1	$M_*$ distribution at each merger stage . . . . .	54
3.2	$M_*$ ratio distribution . . . . .	55
3.3	SFR- $M_*$ plane separated by morphology and merger stage . . . . .	56
3.4	SF mode distribution in each merger stage . . . . .	57
3.5	SF mode distribution in each merger stage separated by morphology . . . . .	59
3.6	Primary's SF mode compared to Secondary's SF mode . . . . .	61
3.7	Primary's SF mode compared to Secondary's SF mode when Primary and Secondary have the same morphology . . . . .	62
3.8	SF mode by Component and morphology . . . . .	63
3.9	SF mode by Component and morphology for Major and Minor mergers . . . . .	65
3.10	Methods to identify AGN . . . . .	67
3.11	AGN fraction at each merger stage . . . . .	68
3.12	AGN fraction at each merger stage from each method . . . . .	70
3.13	BPTs of the merging galaxies hosting an AGN included in the VCV catalogue . . . . .	71
3.14	HeII line diagnostics of the merging galaxies hosting an AGN included in the VCV catalogue . . . . .	71
3.15	Percentages of merging galaxies hosting an AGN at different merger stages . . . . .	72
3.16	AGNs in the SFR- $M_*$ plane . . . . .	72
A.1	Examples of the morphology classification . . . . .	89
C.1	Changing the sky-threshold and n-deblending II . . . . .	92
C.2	Changing the sky-threshold and n-deblending III . . . . .	93
C.3	Changing the sky-threshold and n-deblending IV . . . . .	94

C.4	Changing the sky-threshold and n-deblending V . . . . .	95
D.1	Flux comparison to catalogues coloured by morphology . . . . .	97
E.1	Examples of SED fittings using MAGPHYS . . . . .	99
E.2	Examples of SED fittings using MAGPHYS... continued . . . . .	100
F.1	$M_*$ ans SFR comparison to CHANG15 coloured by merger stage and photometry flag	102
G.1	SF mode at each merger stage separated by $M_*$ bin . . . . .	104
G.2	SF mode for Primary and Secondary separated by $M_*$ bin . . . . .	105
H.1	Primary's SF mode compared to Secondary's SF mode for Major and Minor mergers	107
I.1	BPT-NII-identified AGN on different diagrams . . . . .	109
I.2	BPT-SII-identified AGN on different diagrams . . . . .	110
I.3	HeII-identified AGN on different diagrams . . . . .	111
I.4	WISE-identified AGN on different diagrams . . . . .	112



# List of Tables

- 2.1 List of the best fit parameters . . . . . 41
- 6.1 Columns description of the Catalogue . . . . . 80
- B.1 Table of relevant parameters from Surveys . . . . . 90



## Motivation



Galaxies that are interacting show the most spectacular images observed in our Universe. One of the first catalogues of these remarkable objects was constructed by Halton Arp in 1966, the famous "Atlas of Peculiar Galaxies". His catalogue includes merging systems with one very perturbed object and two or more galaxies interacting. The Hubble Space Telescope (HST) has been observing these objects for years now. Here, I show some of the most breathtaking images found in the HST website.

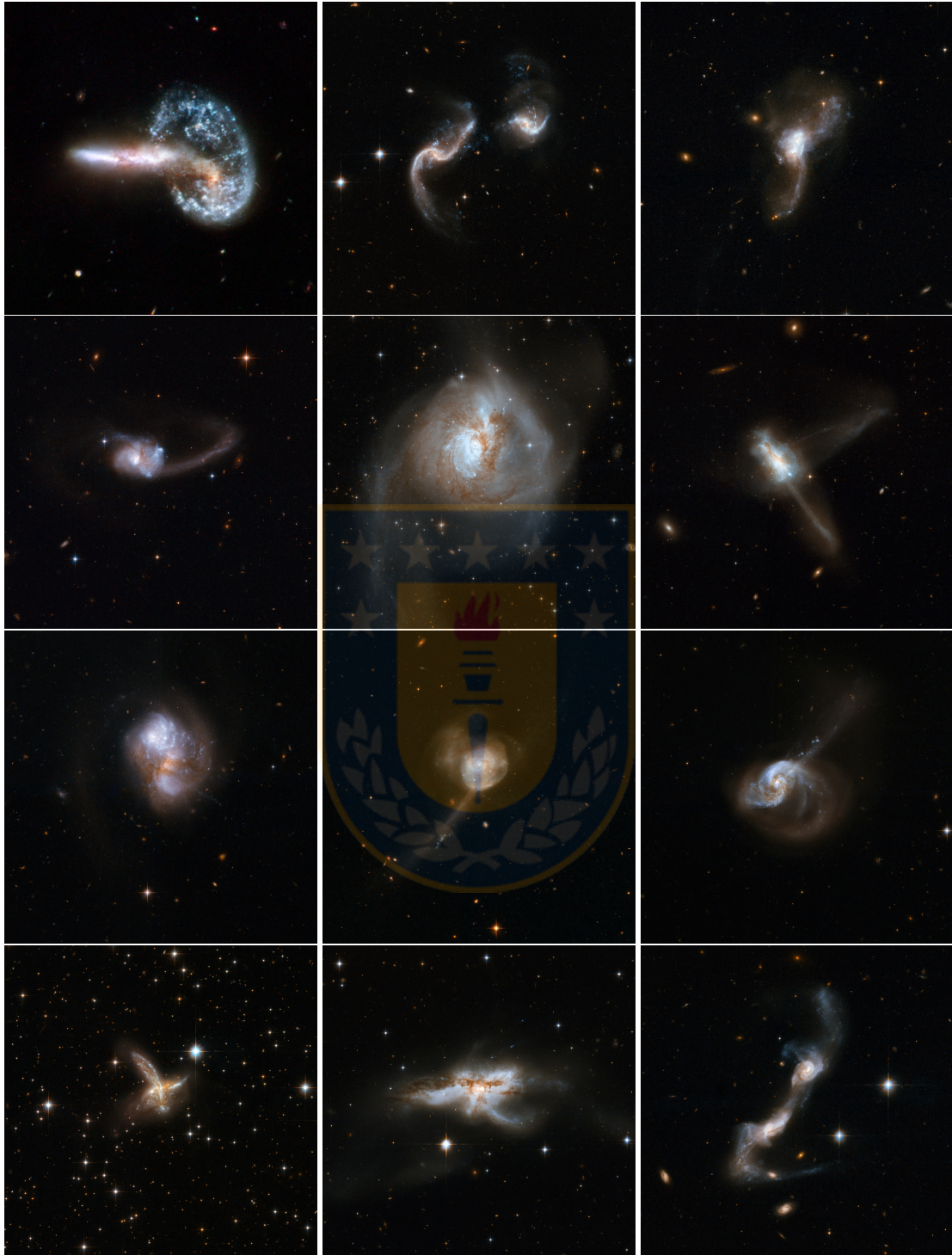
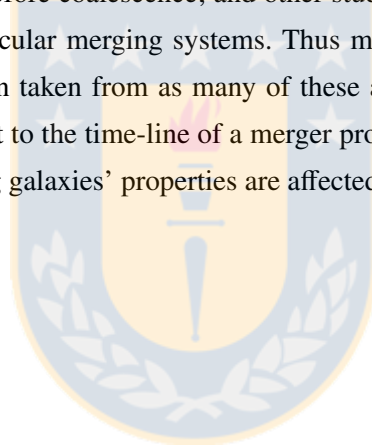


Figure 1 Images taken from the HST website showing selected merging galaxy systems observed with the HST.



As galaxies pass through each other, the battle commences. They begin changing shape, extending their spiral arms to form tidal tails, a bridge of stars and gas suddenly connects the galaxies for an instant. As they struggle to part ways, gravity unites them once again, they pass through each other, over and over again. Now, the objects that were spiral galaxies once, seem to be on their way to form something new, combining their prior qualities and adding some more to this new cosmic composition.

How these cosmic compositions were created and how they evolve has been one of the most interesting topics I have crossed paths with in my scientific learning experience. There have been several simulation studies about merging galaxies and how the process affect these objects in a time-line sequence. However, the observational studies of the evolution during the merger process have typically used the distance between the galaxies as a proxy for the merger stage, but the distance might not be an accurate chronological course as galaxies decrease and increase their separation many times before coalescence; and other studies determine the plausible merger process for only a few particular merging systems. Thus my interest on investigating the available information that has been taken from as many of these astonishing objects as possible, with an approach more consistent to the time-line of a merger process. This, in order to better understand how some of the merging galaxies' properties are affected during this process.



# 1

## Introduction

For long time now, astronomers have studied galaxy evolution and until this day, this is still one of the main topics in Astrophysical research. More than 40 years ago, the first theories about galaxy formation were starting to be established.

Thus, now it is extensively acknowledged that galaxies evolve and grow in stellar mass ( $M_*$ ) following the hierarchical model, where objects form by mergers between less massive objects. Furthermore, it is well known that massive ellipticals and massive spirals can be formed by collisions between two smaller spiral galaxies (Toomre & Toomre, 1972; Springel & Hernquist, 2005).

These transformations in morphology also take place in parallel with changes in colour (Larson & Tinsley, 1978),  $M_*$ , star formation rate (SFR), dust and gas content, metallicity, and also super-massive black hole (SMBH) activity. Galaxies experience all of these changes throughout the merging process.

### 1.1 The Process of Galaxy Merging

Galaxies are highly affected by the environments they inhabit. As Dressler (1980) showed many decades ago, the fraction of elliptical, lenticular and spirals/irregular galaxies is determined by the galaxy density of the environment they are embedded. The fraction of spiral galaxies is higher in the field compared to groups and clusters, while the fraction of elliptical galaxies increases with increasing environmental density and these galaxies are barely seen in the field in the nearby Universe. On the other hand, Butcher & Oemler (1978) found that more spirals are found in clusters at high-redshift compared to low-redshift clusters. Following the hierarchical model, these results suggest that spiral galaxies are transformed as they populate denser and denser environments.

Moreover, observations and simulations show that groups and clusters of galaxies contain very hot gas, the so-called intracluster medium (ICM), which can reach temperatures of multimillion Kelvin (Rhee et al., 2017) for large ( $10^{14-15}M_\odot$ ) clusters. When late-type galaxies fall into the

cluster's potential well, the ICM can remove the atomic gas of the galaxy. This process is known as "ram-pressure stripping" (Gunn & Gott, 1972; Chung et al., 2007; Jáchym et al., 2007). When the interaction between the galaxy and the ICM is not sufficiently strong to strip its atomic disk gas, it can still strip some of its warm, ionized gas (McCarthy et al., 2008; Font et al., 2008). This process is called "starvation" (Larson et al., 1980). On the other hand, mergers in groups and clusters are less frequent compared to field galaxies, since the velocities inside a group/cluster are so high ( $\sim 750$ - $1000$  km/s), galaxies tend to pass through each other without coalesce. These high-speed tidal encounters in groups and clusters cause galaxies to lose mass. This process is known as "harassment" (Moore et al., 1998) and it is highly dependent on the orbit that the galaxies have when interacting (Smith et al., 2010, 2013, 2015). Nevertheless, galaxies still merge in groups and clusters if they have the right relative velocities.

In order to better understand the merger process alone, we decided to study merging galaxies in isolation, where we observe only one or maximum two interacting galaxies. Thus, we can consider the mentioned environmental effects as negligible. Several studies have been done on merging galaxies. These studies show that as galaxies approach each other, their gas starts to be disturbed and disrupted, and may even be transferred to their companion, creating tidal tails and bridges. Additionally, gas is funneled towards their centers, which triggers star formation (SF) and can also activate their SMBH. This process can enhance the SF of galaxies (Larson & Tinsley, 1978) and this enhancement is found to depend on many of the properties of the merging galaxies, such as the  $M_*$  ratio between the two components, the bulge to total luminosity ratio (B/T), the gas and dust content, the orbital parameters of the collision, and the occurrence of AGN feedback (Mihos & Hernquist, 1994a,b; Di Matteo et al., 2005; Hopkins et al., 2008; Di Matteo et al., 2008; Park et al., 2017).

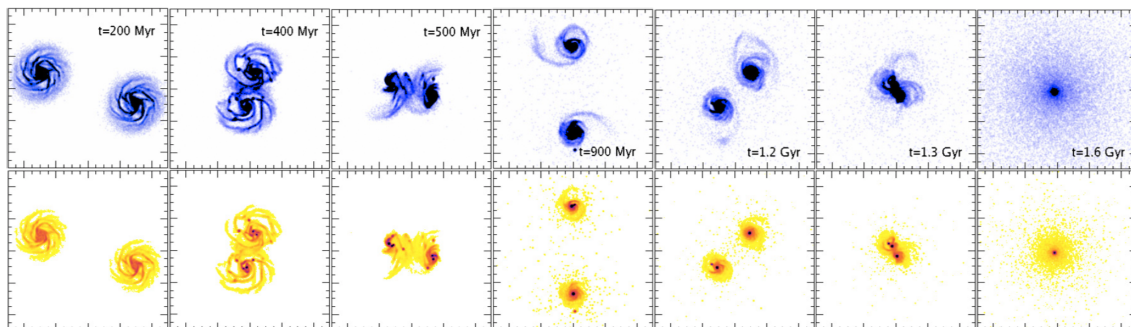


Figure 1.1 Elliptical galaxy formed by a merger process. Timelapse of two gas-rich spiral galaxies merge forming an elliptical galaxy. Gas and stars are shown in the top and bottom panels, respectively. *Snapshots are taken from Di Matteo et al. (2008)*

Figures 1.1 and 1.2 show simulations of two different merger processes. The gas and the stars can be seen on the top and bottom panels, respectively. The first process consists of two gas-rich spiral galaxies, which merge forming an elliptical galaxy. The second process consists of one gas-rich spiral and another spiral without gas, which merge forming a more massive spiral galaxy. The snapshots are taken from Di Matteo et al. (2008)'s simulations.

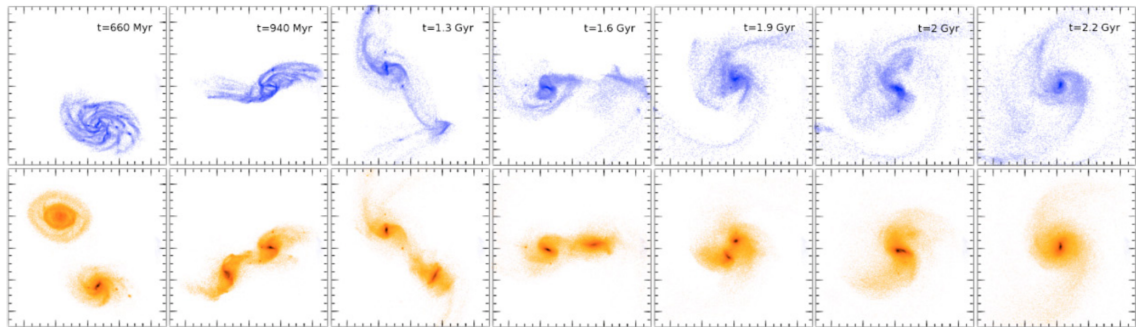


Figure 1.2 Spiral galaxy formed by a merger process. Timelapse of two spiral galaxies (one gas-rich and one gas-poor) merging to form an spiral galaxy. Gas and stars are shown at the top and bottom panels, respectively. *Snapshots are taken from Di Matteo et al. (2008)*

### 1.1.1 Star Formation Enhancement predicted by Merger Simulations

Simulations of mergers have been studied mainly in isolation, where the set of parameters only include the galaxies' properties and the collision orbital parameters. Thus, no detailed properties of their cosmological surroundings are considered, allowing us to understand the merging process separately from environmental effects. Nonetheless, since a few decades ago, simulators have found that there are some properties we do not fully understand and that these can make a large difference in the merging process results. For example, Mihos & Hernquist (1994a,b) studied how the star formation of merging galaxies are affected when they have a bulge or not. They also separate their simulations depending on the mass ratio between the galaxies. For merging galaxies with similar mass (major mergers), they found that galaxies without a bulge develop bars in the centers soon after the first passage, these bars allow great amounts of gas to flow towards the center triggering short but significant starbursts. This does not occur in merging galaxies with a bulge as the bulge stops the inflow of gas, not allowing the starburst to happen at this stage. However, a strong starburst occurs as the galaxies coalesce.

Figure 1.3 shows the star formation rate relative to a non-merging galaxy over the full timeline of merger process for merging galaxies with a bulge (thick line) and without a bulge (thin line). Following the bulgeless galaxies (thin line), we can see that at the first passage between the galaxies ( $T \sim 40$ ) the SFR is enhanced 20-30 times the SFR of non-merging galaxies. In this manner,

galaxies use their gas quickly ( $\sim 1.5 \times 10^8$  yr), thus, starburst are not observed after the first passage. On the other hand, galaxies with a bulge (thick line) do not show a high star formation at this stage, as the bulge helps to stabilise the gas, but at final coalescence these mergers show a rise in SFR of 70 times the SFR of non-merging galaxies. This powerful starburst lasts for only  $5 \times 10^7$  yr.

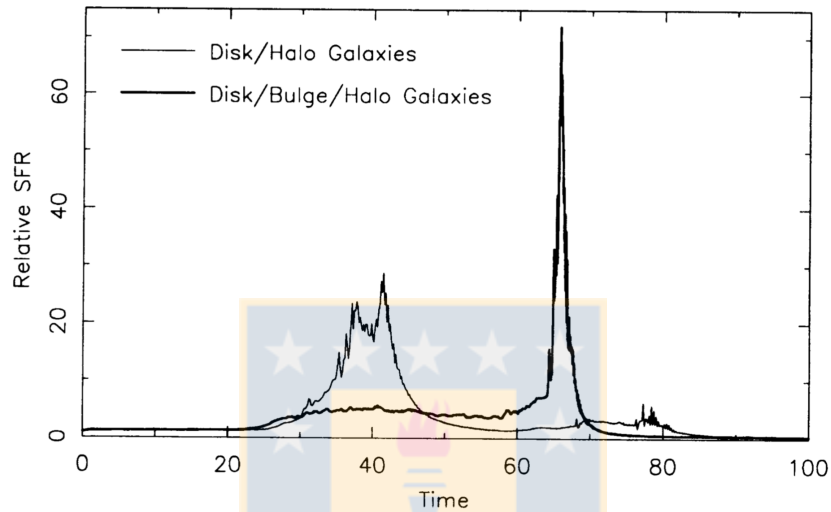


Figure 1.3 Star formation histories of simulated major mergers, with and without a bulge. Time in the  $x$ -axis is in  $10^7$  yr. Credits: Mihos & Hernquist (1994a)

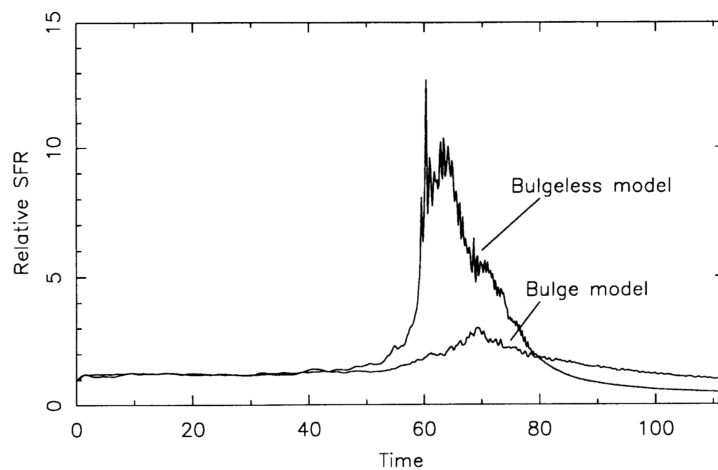


Figure 1.4 Star formation histories of simulated minor mergers, with and without a bulge. Credits: Mihos & Hernquist (1994b)

For the case when galaxies with very different masses merge (so called minor mergers), Mihos & Hernquist (1994b) show that a strong starburst is not observed at the first passage, contrary to major mergers. Figure 1.4 shows the evolution of the global SFR (similar to the previous figure) of merging galaxies with and without a bulge. This figure shows that the global SFR rises only at late merger stages and the highest SFR is reached by the bulgeless merger, which is higher than 10 times the SFR of non-merging galaxies. This starburst lasts for a longer period compared to major mergers ( $2.3 \times 10^8$  yr). On the other hand, galaxies with a bulge also show an increased SFR at late-merger stages but only by 3 times the SFR of non-merging galaxies.

As simulations progress, new recipes for the physics of different components are included to the different coding. Di Matteo et al. (2005) show that numerical simulations including black hole growth show different results compared to simulations without a nuclear super-massive black hole (SMBH). Figure 1.5 shows the gas distribution of two of their simulations, the top images show snapshots of the merging galaxies with a SMBH and the bottom images show snapshots of the simulation of merging galaxies without a SMBH. From left to right, the figure shows four different times in the merging process. First, galaxies are shown just after the first passage (1.1 Gyr). The second snapshot shows the moment before coalescence (1.4 Gyr). The third snapshot is taken at final coalescence (1.6 Gyr). Finally, the fourth snapshot shows the remnant merger at 2.5 Gyr.

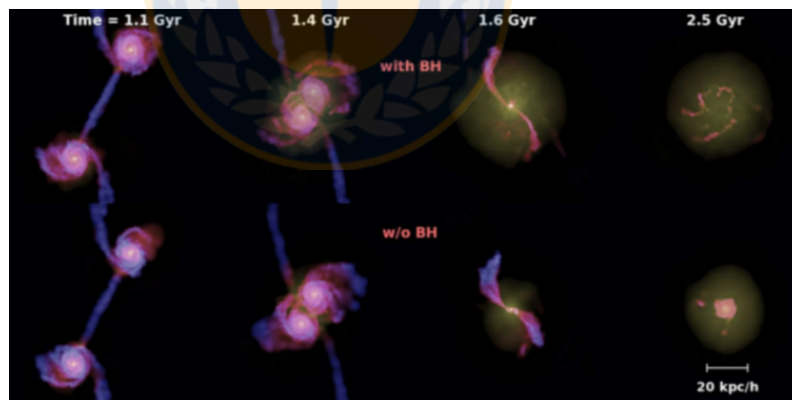


Figure 1.5 Simulations of mergers with and without a black hole. Di Matteo et al. (2005)'s numerical simulations of merging galaxies with (top) and without (bottom) nuclear super-massive black hole.

We can notice how the morphology of the merging galaxies are affected by the inclusion of the black hole in the simulation. The third and fourth snapshots show the most evident differences, where we can observe a concentration of gas in the center of the remnant without the black hole. This is not observed in the simulations with the black hole, indicating that the black hole plays an

important role on the gas distribution of mergers. Furthermore, Figure 1.6 shows the star formation history and the black hole growth of merger simulations of galaxies with different stellar mass.

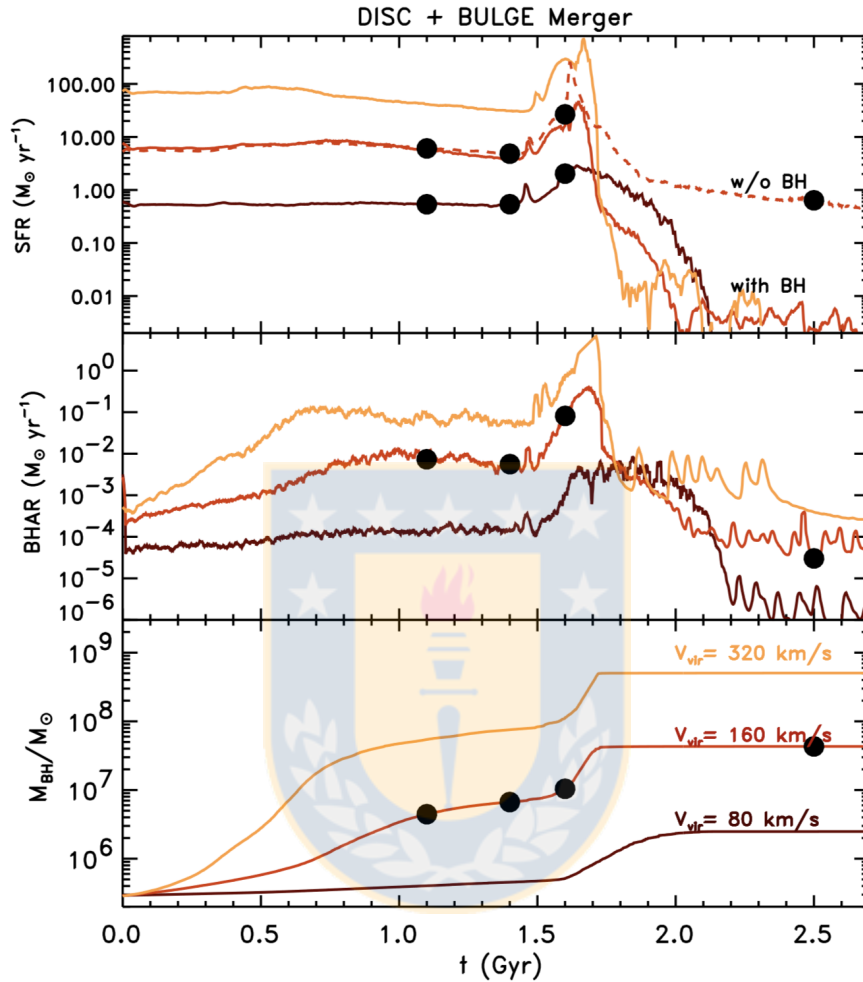


Figure 1.6 Star formation history and black hole growth in Di Matteo et al. (2005)'s simulations. Star formation history (top), black hole accretion rate (middle), and black hole growth (bottom) of merger simulations shown by Di Matteo et al. (2005). The coloured lines show the models of galaxies with virial velocity  $v_{vir} = 80$  (dark red), 160 (red), and 320 km/s (orange). The dashed-line in the top panel shows the model of a galaxy without SMBH. The four black circles show the different stages shown in Figure 1.5, from left to right.

The top panel shows the star formation rate throughout the merging process, where we can observe that different masses (coloured lines) show similar behaviour until the coalescence stage (third black dot). Just after coalescence, more massive galaxies (light-orange line) show a higher peak and a more abrupt decay in SFR compare to the low-mass merger (dark-red line). Also notice the SFR of a merger without a black hole (dashed-orange line), where the peak after coalescence

is significantly higher than the merger with a black hole (solid-orange line). On the other hand, the black hole accretion (middle panel) and black hole growth (bottom panel) shows its dependence on the mass of the merging galaxies. More massive galaxies start the black hole growth sooner within the merger process (peaking at coalescence), in contrast to lower mass galaxies, where the growth is only produced at and after coalescence.

Furthermore, Di Matteo et al. (2008) studied hundreds of simulations of major mergers, using different parameters for these merging galaxies, such as stellar mass, bulge mass, and gas fraction, and different initial parameters for the merging galaxies' orbits. For example, Figure 1.7 presents the star formation history of four different mergers, from which all have as the primary a spiral galaxy with gas-to-stellar mass ratio of 10%. From left to right, the panels show the primary spiral merging with: a similar spiral with a retrograde orbit and an angle of  $45^\circ$ , a similar spiral with a direct orbit and an angle of  $90^\circ$ , a gas-rich (20%) spiral with a retrograde orbit and an angle of  $45^\circ$ , and a more gas-rich (30%) spiral with a direct orbit and an angle of  $45^\circ$ . Retrograde and direct orbits refer to the direction of the spin of the galaxy's rotation, retrograde merging galaxies have opposite rotations, and direct merging galaxies have the same direction of rotation. The angle refers to the angle between the disk of each merging galaxy at the time of collision.

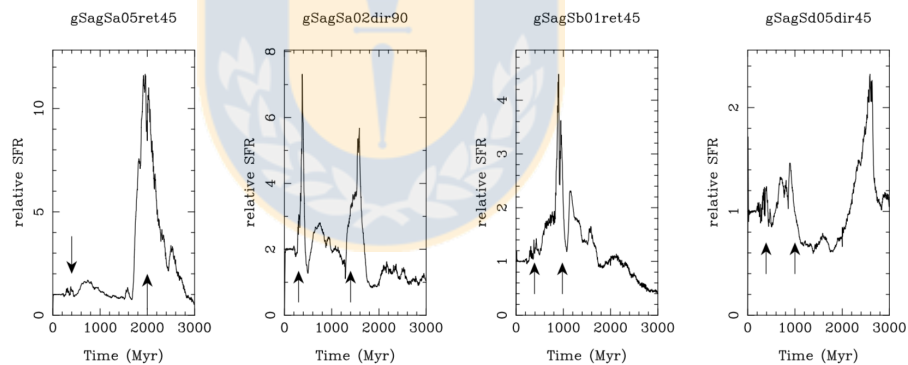


Figure 1.7 Star formation history for different mergers simulated by Di Matteo et al. (2008). The arrows show the first pericenter passage and the time of coalescence.

As we can see in the first two panels, the direction and the angle of collision affect the SFR throughout the merger process. We observe a peak in star formation at the first passage when the two galaxies collide in an angle of  $90^\circ$  (second panel). This is contrary to the merger with the two galaxies forming an angle of  $45^\circ$  and a opposite rotation direction (first panel), where there is no starburst at this period. On the other hand, both show a peak of star formation at the time of coalescence, the highest and longest shown by the merger showing no starburst at early stages, as the prior merger used its gas at early and intermediate stages.



On the other hand, the other two mergers show lower relative SFR compared to the two first cases (notice the y-axis values of the different panels). There is a small peak of star formation at first passage for both cases, and at the time of coalescence both show higher relative SFR, the highest being shown by the retrograde orbit. Overall, strong starbursts (stronger than 5x) are rarely found in these simulations ( $\sim 15\%$ ). Also, the starbursts last for a short period of time (only a few  $10^8$  yr).

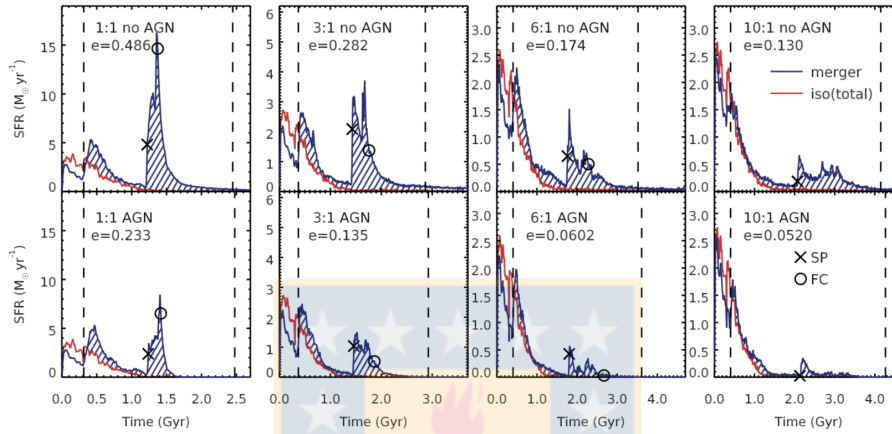


Figure 1.8 Star formation history for different mergers simulated by Park et al. (2017). Star formation history for major (left panels) and minor mergers (right panels). The top panels show mergers of simulations not considering AGN and the bottom panels show mergers with AGN. The X and circle show the second passage and final coalescence, respectively. The "e" parameter (top-left corner) shows the SFR excess, the comparison between the SFR of the merger (blue) to the isolated (red) galaxies between the two vertical dashed-lines.

A recent study investigated hydrodynamical simulations to test AGN feedback affecting the merging process (Park et al., 2017). Several simulations have shown that as the SMBH is triggered, the AGN can heat the surroundings, halting star formation in its surroundings. Park et al. (2017) found that the AGN feedback suppresses the star formation more efficiently compared to non-merging galaxies and this effect is larger for major than for minor mergers. Figure 1.8 shows the star formation history of major and minor mergers, from left to right, with stellar mass ratios of 1:1, 3:1 for the major mergers and 6:1, and 10:1 for the minor mergers. Merging galaxies without AGN feedback are shown on the top panels and simulations that include AGN feedback are shown on the bottom panels. The blue shaded regions show the star formation rate of the merging systems to compare with an isolated galaxy shown in red. The 'X' and 'O' symbols show the second passage and final time of coalescence, respectively. It is clear that galaxies reach higher SFR when AGN feedback is not considered. Also, major mergers show higher SFR compared to minor mergers.

Figure 1.9 shows the star formation history of mergers considering AGN feedback (as the

bottom panels of the previous figure) on the top panel (Park et al., 2017). The middle and bottom panels show the black hole growth and accretion rate, respectively. Notice the dashed lines in these panels which show the growth and accretion rate of an isolated galaxy's black hole. The AGN accretion is higher at second passage and coalescence (second and third vertical dotted lines) for major mergers, while for minor mergers, the black hole growth is not that different than the isolated galaxy, and the accretion rate is much lower. Additionally, Park et al. (2017) studied the effect of the AGN in bulge and bulgeless galaxies, similar to Mihos & Hernquist (1994a,b)'s studies mentioned previously. They found that for minor mergers, the primary's bulge size does not play an important role when AGN feedback is included. However, there is still a tendency for SFR to be higher for bulgeless galaxies compared to galaxies with a bulge.

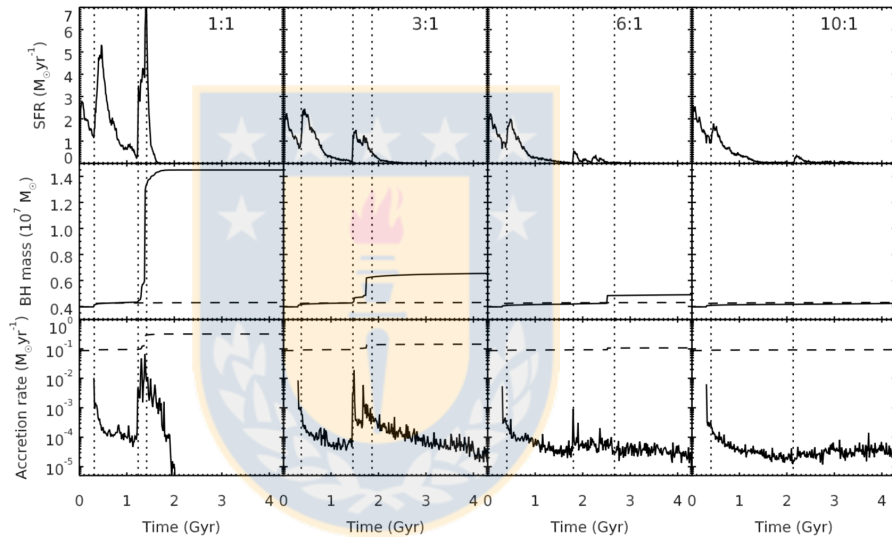


Figure 1.9 SFH and accretion for different mergers simulated by Park et al. (2017). Star formation history (top), BH mass growth (middle), and AGN accretion (bottom) for major and minor mergers (Park et al., 2017).

While simulations show that the SF enhancement can be 2-20 times higher than the SFR of non-interacting galaxies, observations show that some very perturbed galaxies show SFR up to 10-100 times higher compared to unperturbed galaxies with the same  $M_*$ .

## 1.2 The SFR- $M_*$ plane and the Main Sequence of Star Formation

Several observations have shown that unperturbed star-forming galaxies form stars according to their stellar mass. Massive galaxies form stars faster compared to less massive galaxies following a tight relation, the so-called Main Sequence (MS) of star formation. There have been many studies

to determine this relation at low- and higher-redshifts (Elbaz et al., 2007; Noeske et al., 2007; Daddi et al., 2007; Pannella et al., 2009; Karim et al., 2011; Wuyts et al., 2011; Whitaker et al., 2012; Rodighiero et al., 2014; Whitaker et al., 2014; Chang et al., 2015; Pannella et al., 2015; Renzini & Peng, 2015; Schreiber et al., 2015, 2017).

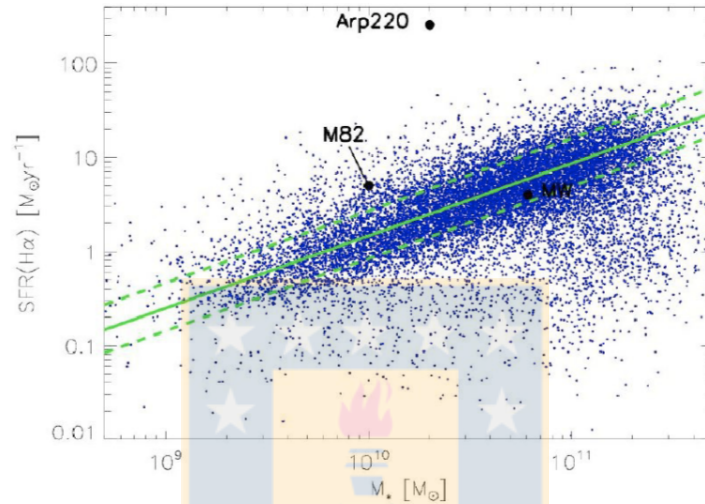


Figure 1.10 Main Sequence. SFR- $M_*$  plane of low-redshift SDSS galaxies from Elbaz et al. (2007). The green-solid line shows the Main Sequence with its scatter (0.3 dex) shown by the dashed-green lines. Three special cases are shown: our Milky Way (MW), M82, and Arp220. The latter two are likely involved in galaxy interactions.

Figure 1.10 shows the SFR- $M_*$  plane and the MS determined by Elbaz et al. (2007), represented by the solid-green line, for a sample of low-redshift ( $0.015 \leq z \leq 0.1$ ) galaxies from SDSS. The dashed-green lines show a scatter of 0.3 dex. Notice the position of our Milky Way (MW) below the MS but within the scatter. For reference in this figure, the  $M_*(\text{MW}) = 6.1 \times 10^{11} M_\odot$  (Flynn et al., 2006) and  $\text{SFR}(\text{MW}) = 4 M_\odot \text{ yr}^{-1}$  (Diehl et al., 2006). It also shows the galaxies M82 and Arp220. M82 is a very luminous galaxy within the group of galaxies M81, located in the constellation of Ursa Major. This galaxy is considered a starburst galaxy which is forming stars 10 times faster than an MS galaxy. Arp220 is a peculiar galaxy catalogued by Halton Arp in 1966, Arp220 is forming stars at a rate  $\sim 200 M_\odot \text{ yr}^{-1}$  (Varenius et al., 2016), which is astonishingly high compared to MS galaxies.



Figure 1.11 Images of galaxies. From left to right: we show a representation of our Milky Way, and images of the interacting galaxies M82 and Arp220. *Credits: Images from <https://www.spacetelescope.org>*

Figure 1.11 shows an image of our Milky Way (representation; left), M82 (middle), and Arp220 (right). Just from the morphology, we can observe that the representation of the MW looks like a normal/unperturbed spiral, in contrast to M82 and Arp220 which have unusual morphologies. M82 is known to have been involved in an interaction with M81, the central galaxy of the group. And Arp220 is a system of two interacting galaxies in the stage of coalescence. These two latter cases show high values of SFR, this phenomenon has been observed in a more extensive sample. Elbaz et al. (2011) studying ultra-luminous infrared galaxies (ULIRGs), observed that compact galaxies show high SFR compared to non-interacting galaxies with the same  $M_*$ , and that these galaxies tend to show features of interactions. Figure 1.12 shows the compact galaxies (red dots) studied by Elbaz et al. (2011). These galaxies are mostly above their MS upper limit, showing very high (10-100x) SFR compared to unperturbed galaxies (black dots).

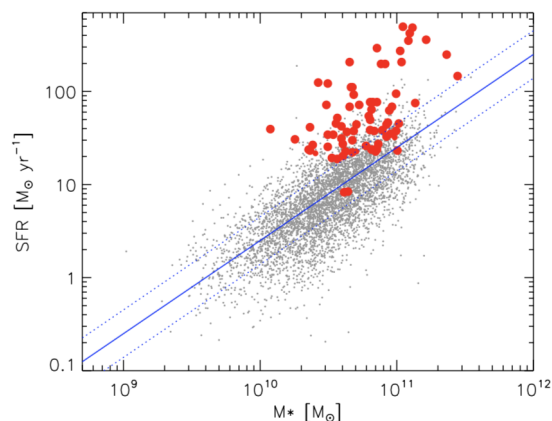
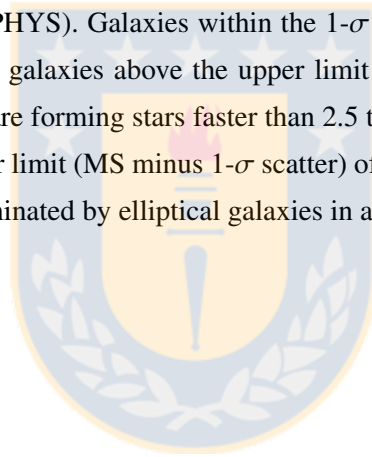


Figure 1.12 Main Sequence and compact ULIRGs. SFR- $M_*$  plane of compact galaxies from Elbaz et al. (2011). The red dots show compact galaxies which tend to show features of interactions.

### 1.2.1 Star Formation Mode

As mentioned previously, simulations compare the SFR to the SFR of simulated non-merging galaxies, and the observational studies mentioned here compare their SFR to the SFR of a control sample. In this thesis, in order to study the rise of SFR of galaxies during the merger process, we compare the SFR of the merging galaxy to the SFR that a galaxy would have at the same  $M_*$  if this galaxy were in the MS. We refer to this comparison ( $sSFR/sSFR_{MS}$ ) as star formation mode (SF mode) also referred to as "starburstiness" in the literature (Elbaz et al., 2011). The SF mode measures the separation from the MS, hence galaxies in the MS have an SF mode equal to zero.

We chose to perform the comparisons to the MS shown by Chang et al. (2015, hereafter CHANG+15) as they determined their MS using  $M_*$  and SFR estimated via SED fitting utilising the same code we used (MAGPHYS). Galaxies within the  $1-\sigma$  scatter determined by CHANG+15 are referred to as MS galaxies, galaxies above the upper limit (MS plus  $1-\sigma$  scatter) are called starburst galaxies (SB), which are forming stars faster than 2.5 times the rate of MS galaxies, and finally, galaxies below the lower limit (MS minus  $1-\sigma$  scatter) of the MS are referred to as passive galaxies, which are usually dominated by elliptical galaxies in a non-merging sample.



## 1.3 Dependence on Companion Distance and the Morphology

In interacting galaxies, the IR luminosity, AGN content, and SFR are highly related to the distance and morphology of the companion galaxy (Hwang et al., 2010, 2011; Ellison et al., 2013; Satyapal et al., 2014). Hwang et al. (2010, 2011) found that the changes in IR luminosity, AGN content and SFR occur when the galaxies are at distances lower than their virial radius ( $v_r$ ), showing the highest values for these three properties at distances lower than  $0.5 v_r$ . Figure 1.13 shows the dependency of the IR luminosity ( $L_{IR}$ , top panel), and (U)LIRG fraction (middle and bottom panels) on the distance to and the morphology of the companion. Blue symbols show (U)LIRGs with a late-type companion and red symbols show (U)LIRGs with early-type companions. The  $L_{IR}$  and (U)LIRG fraction increases when the companion is a late-type galaxy but these properties seem to decrease when the companion is an early-type galaxy.

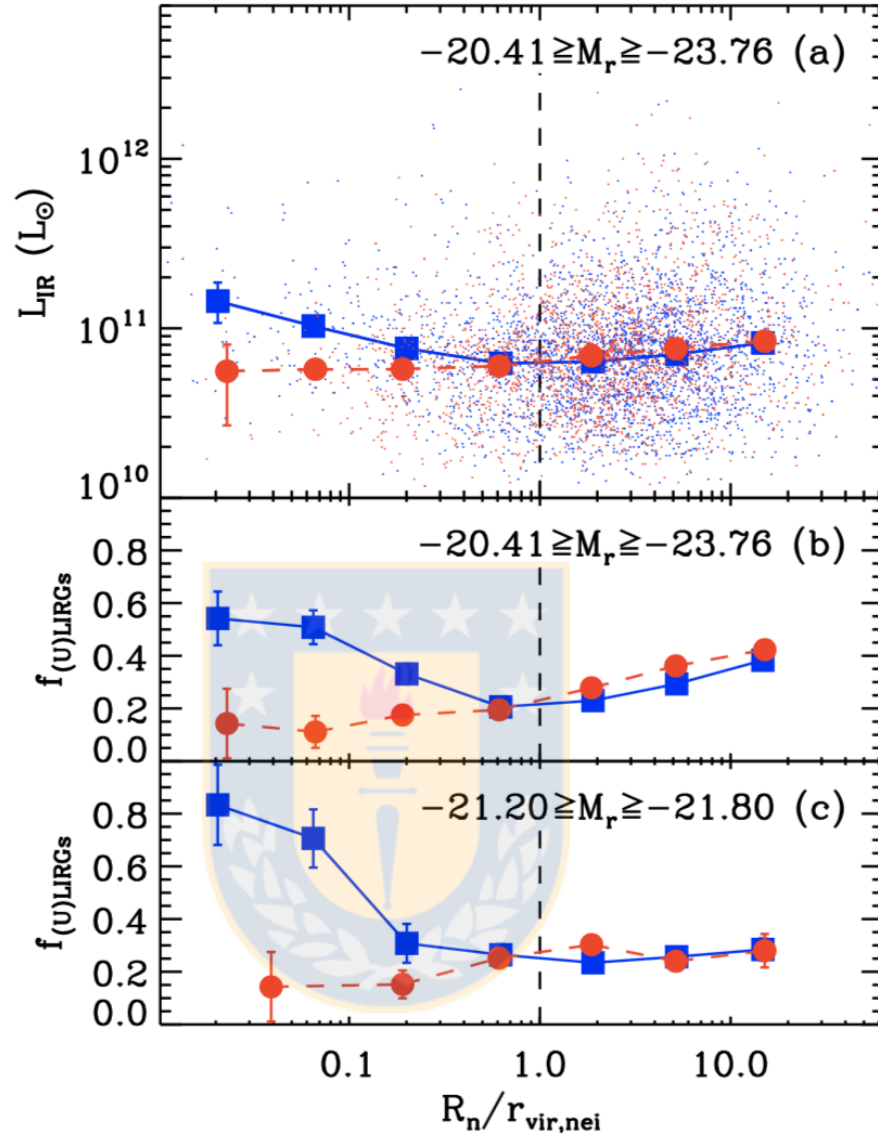


Figure 1.13 ULIRG fraction according to the distance to and the morphology of its companion.  $L_{\text{IR}}$  and (U)LIRG fraction dependency on the distance to and the morphology of the companion as shown by Hwang et al. (2010). Symbols show the morphology of the companion galaxy, blue squares and red circles represent late-type and early-type galaxies, respectively.

Figure 1.14 show a similar behaviour for the SFR (top panel) and specific star formation rate (sSFR; bottom panel) of (U)LIRGs. These two increase as the late-type companion gets closer and decrease when the close companion is an early-type galaxy. The  $M_*$  (middle panel) seems to do the opposite, it decreases when the companion is a late-type and stay almost constant when the companion is an early-type galaxy (Hwang et al., 2011).

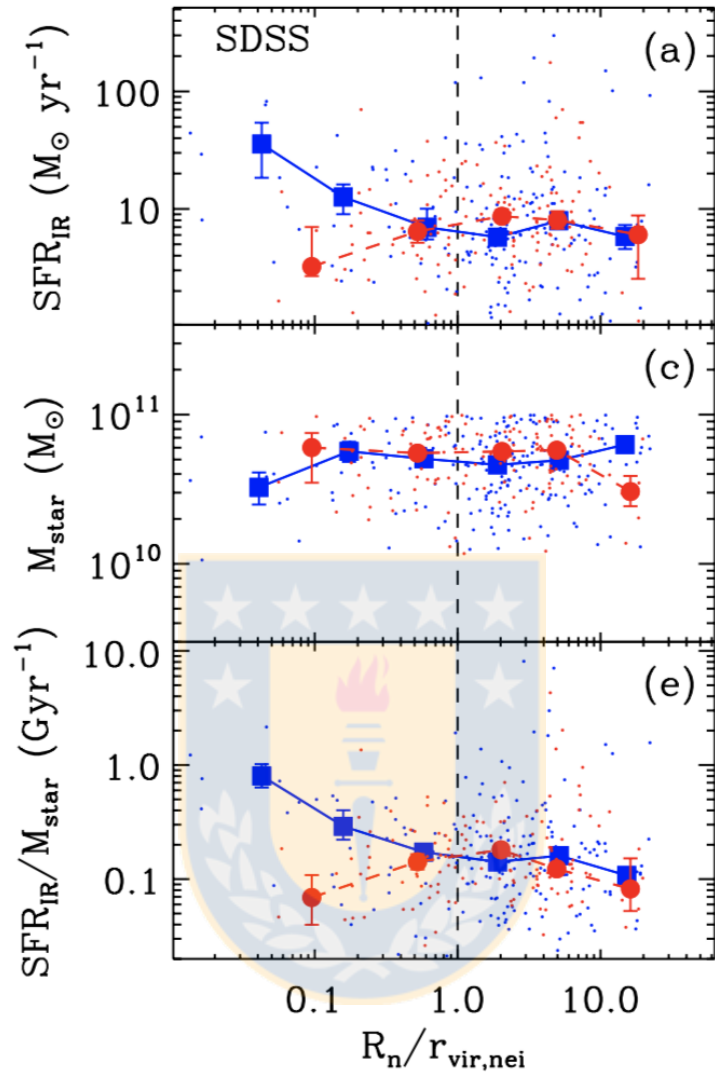


Figure 1.14 SFR,  $M_*$ , and sSFR according to the distance to and the morphology of its companion. SFR (top panel),  $M_*$  (middle panel), and sSFR (bottom panel) dependency on the distance to and the morphology of the companion as shown by Hwang et al. (2011).

Furthermore, Ellison et al. (2013) showed that galaxies increase their SFR when the distance to the companion decreases as compare to the respective control sample. Figure 1.15 shows the dependence of the SFR excess (SFR of the galaxy compared to the control sample) as a function of the distance to its nearest neighbour. The shaded region shows the SFR of post-mergers. The decline of SFR with distance to the companion is clear. However, the SFR excess shows low values (2 - 3), which are similar to the results obtained from simulations but very different to the interacting (compact) galaxies shown by Elbaz et al. (2011).

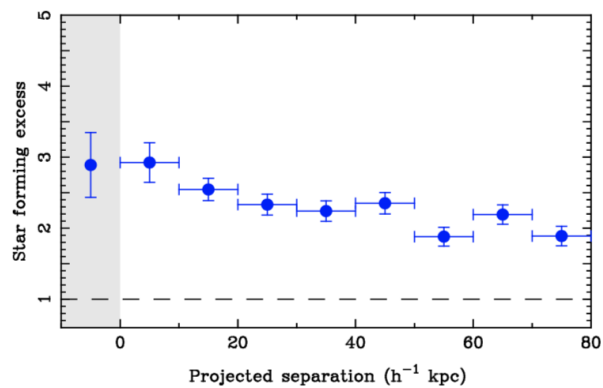


Figure 1.15 SFR excess according to the distance to its companion. Dependence of the SFR excess as a function of the distance to its companion as shown by Ellison et al. (2013).

Using the same sample as Ellison et al. (2013), Satyapal et al. (2014) studied the fraction of galaxies with an AGN according to the distance to the nearest companion. They identified galaxies hosting an AGN using a WISE colour limit (Stern et al., 2012,  $W1 - W2 \geq 0.8$ ). These AGN fractions are shown in Figure 1.16 as blue symbols. They also lower the WISE colour limit to  $(W1 - W2) \geq 0.5$  as galaxies with redshift lower than 0.2 show colours much lower than 0.5 (Assef et al., 2013). These AGN fractions are shown in red. Again, the shaded region shows post-mergers. The AGN fraction shows a clear decline with distance to the companion, post-mergers showing values twice as large as the smallest separation. However, the values of the fractions are very small (0.1 - 0.16) which suggest that AGN are not very common in interacting galaxies.

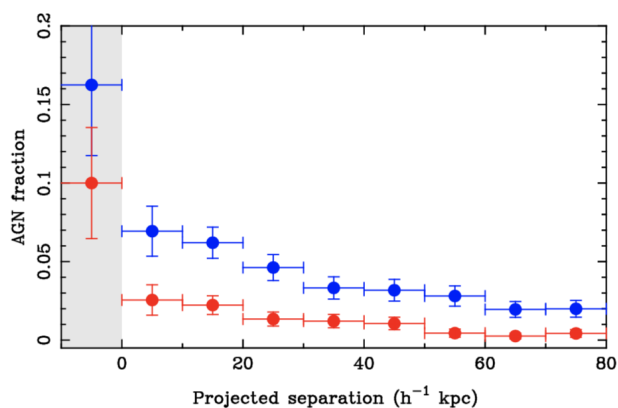


Figure 1.16 AGN excess according to the distance to its companion. AGN fraction dependency on the distance to the companion as shown by Satyapal et al. (2014).



## 1.4 Stellar Mass and Star Formation Rate Estimators

There are many different methods to estimate  $M_*$  and SFR. The most frequently method used to estimate  $M_*$  is the one shown by Bell et al. (2003), which relates the optical colour ( $g - r$ ) from SDSS to the  $r$ -band Mass-to-Light (M/L) ratio, as follows:

$$\log(M_*/L_r) = \begin{cases} -0.15 + 0.93(g - r) \\ -0.306 + 1.097(g - r) \end{cases}, \text{ for } 0.3 < (g - r) < 1$$

This method is based on mass-to-light ratios ( $M/L$ ) determined using SED fitting to some or all of the  $ugrizK$  fluxes obtained for the Milky Way. Similarly, Taylor et al. (2011) studied galaxies from the Galaxy And Mass Assembly (GAMA) sample, using the ( $g - i$ ) and the  $i$ -band luminosity ( $L_i$ ) from SDSS. They obtained the following relation:

$$\log(M_*/L_i) = -0.68 + 0.70(g - i)$$

Another method is the one shown by Cluver et al. (2014), where they show the relation between  $M_*$  and WISE colours. They find three different relations, for low-redshift sources, for star-forming galaxies, and for the entire sample, as follows:

$$\log(M_{stellar}/L_{W1}) = \begin{cases} -2.54(W1 - W2) - 0.17 & , \text{ for low-redshift galaxies} \\ 0.04(W1 - W2) - 1.93 & , \text{ for star-forming galaxies} \\ -1.96(W1 - W2) - 0.03 & , \text{ for the entire sample} \end{cases}$$

with  $L_{W1}(L_\odot) = 10^{-0.4(M_{W1}-3.24)}$ , where  $M_{W1}$  is the absolute magnitude of the galaxy in W1.

For SFR, there are also several methods. These can be based on the UV emission, the  $H_\alpha$  emission line, and/or the IR emission. Cluver et al. (2014) presents two relations, one between the dust-corrected  $H_\alpha$ -derived SFR and the W3 luminosity, and the second related to the W4 luminosity. These are as follows:

$$\log \text{SFR}_{H_\alpha} (M_\odot \text{ yr}^{-1}) = 1.13 \log \nu L_{W3}(L_\odot) - 10.24$$

$$\log \text{SFR}_{H_\alpha} (M_\odot \text{ yr}^{-1}) = 0.82 \log \nu L_{W4}(L_\odot) - 7.3$$

Three other studies also relate the W4 luminosity to the SFR: Lee et al. (2013), Jarrett et al. (2013), and CHANG+15. Lee et al. (2013) shows two relations, one non-linear and a second with a slope equal to unity, as follows:

$$\text{SFR}_{\text{W4}}(M_{\odot} \text{ yr}^{-1}) = (4.25 \pm 0.20) \times 10^{-9} L_{\text{W4}}^{0.96 \pm 0.01} (L_{\odot})$$

$$\text{SFR}_{\text{W4}}(M_{\odot} \text{ yr}^{-1}) = (1.59 \pm 0.11) \times 10^{-9} L_{\text{W4}} (L_{\odot})$$

Jarrett et al. (2013) and CHANG+15, as well as Cluver et al. (2014), claim that the relations to W4 are more accurate than the ones using W3, since W3 is highly affected by PAH emission, which is not the case for W4. Jarrett et al. (2013) and CHANG+15 relations, respectively, are as follows:

$$\text{SFR}_{\text{IR}}(\pm 0.04)(M_{\odot} \text{ yr}^{-1}) = (7.50 \pm 0.07) \times 10^{-10} L_{\text{W4}} (L_{\odot})$$

$$\log \text{SFR}_{\text{W4}}(M_{\odot} \text{ yr}^{-1}) = \log L_{\text{W4}}(L_{\odot}) - 9.08$$

Another way to estimate the SFR is to measure the emission of young stars (UV) and correct it by the dust extinction (IR). Janowiecki et al. (2017) shows this combined approach, using the NUV band from GALEX and the W4 filter from WISE, as follows:

$$\text{SFR}_{\text{NUV}}(M_{\odot} \text{ yr}^{-1}) = 10^{-28.165} * L_{\text{NUV}}(\text{erg/s/Hz}), \text{ from Schiminovich et al. (2007)}$$

$$\text{SFR}_{\text{W4}}(M_{\odot} \text{ yr}^{-1}) = 7.50 \times 10^{-10} (L_{\text{W4}} - 0.04 L_{\text{W1}}) (L_{\odot})$$

where the total SFR will be the sum of both:

$$\text{SFR} = \text{SFR}_{\text{NUV}} + \text{SFR}_{\text{W4}}$$

These methods are based on one or two band photometric data. As merging galaxies are unusual galaxies, showing very perturbed morphologies, it is not unexpected that they do not follow the same relations followed by unperturbed galaxies. Thus, we decided that the best method to estimate  $M_*$  and SFR is via fitting the spectral energy distribution (SED) of the merging galaxy using as many photometric points as possible. For this, we compile all the information from the largest surveys currently available: the GALaxy Evolution eXplorer (GALEX), the Sloan Digital Sky Survey (SDSS), and the Wide-field Infrared Survey Explorer (WISE). After compiling the available data, we noticed that the radius of the merging galaxies, as listed in the catalogues, was smaller than the ones shown in the images, indicating that the radius measured automatically was not recovering the light of the entire galaxy for this type of objects. Thus, we were compelled to perform the photometry on our merging galaxies in a less automated way in order to obtain more accurate values for  $M_*$  and SFR.

### 1.4.1 Photometry using SExtractor

There are several softwares and tools to extract sources from an image (e.g. SkyCat, IRAF, DS9). These are mainly aimed to study one or a few objects at a time, as the photometry is performed in a manual and more precise manner. SExtractor (Source Extractor) is the commonly used software to perform photometry in large samples, as this can extract sources from many images automatically setting a few initial parameters. Here, it's possible to set parameters such as: detection threshold from the sky, deblending parameters, background sizes, and output images like background, objects found, the image with the objects subtracted, among many others. These parameters can be different for each image when is used from a script, e.g. IDL or python. This makes SExtractor the perfect tool for my task.

Since I noticed that the available photometry from the different surveys underestimates the flux of merging galaxies, I measured the photometry of the merging galaxies in our sample in all the 11 filters (FUV, NUV, *u*, *g*, *r*, *i*, *z*, W1, W2, W3, and W4) in a less-automated manner, using SExtractor. The parameters that affect the photometric measurements of merging galaxies the most are the sky-threshold and the n-deblending. The first one sets the minimum flux to detect an object, this mainly affects faint merging galaxies and merging galaxies with faint tidal tails. The second one decides the threshold use to determine whether a separated but nearby source is part of the same object or not. This parameter also affects the detection of faint tidal tails, and galaxies with luminous star-forming regions, as these can be detected as separated objects.

### 1.4.2 SED fitting using MAGPHYS

MAGPHYS is a spectral energy distribution (SED) fitting code created by da Cunha et al. (2008). The SED shows the flux of the light emitted by a galaxy at different wavelengths. Thus, from an SED, we can learn about many of the components (e.g. stars, gas, and dust) of a galaxy depending in which wavelength we observe. MAGPHYS contains 50,000 stellar population template spectra and 50,000 polycyclic aromatic hydrocarbons (PAH)+dust emission template spectra, which are used to fit the ultraviolet (UV)/optical and infrared (IR) photometric data, respectively. The stellar templates include models with random, and superimposed bursts of star formation, generating templates with different star formation histories. Figure 1.17 shows the SED of three different galaxies with available photometric points (red symbols) from UV (GALEX) to IR (SCUBA). The best fit obtained by MAGPHYS to the photometric data is shown in black, with the residuals shown in the small subpanels. The unattenuated stellar population spectrum is shown in blue. After computing the goodness of the fit parameter  $\chi^2$ , MAGPHYS provides several properties of a galaxy. For this study, we focus on the  $M_*$  and the SFR with their respective likelihood distributions.

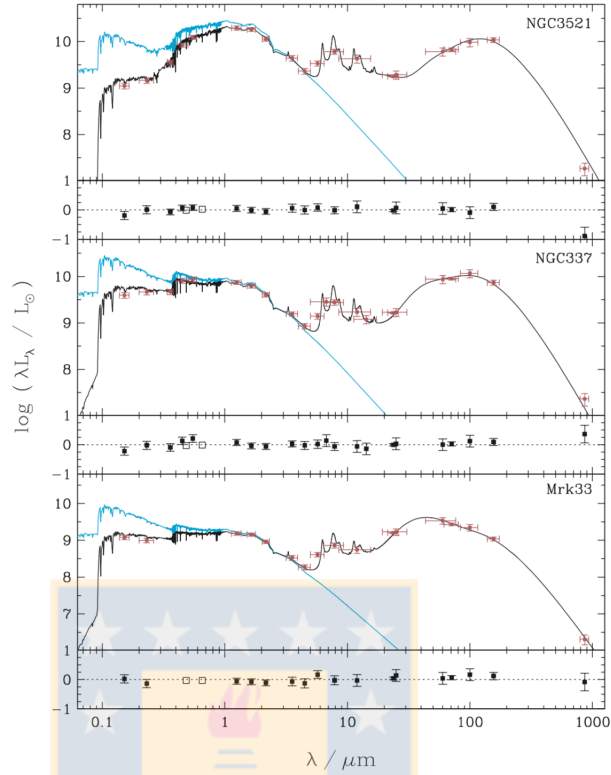


Figure 1.17 SED fitting. The SED of three different galaxies fitted by MAGPHYS (da Cunha et al., 2008).

There are several SED fitting codes, these can have different ranges in wavelength and different methods to estimate the resulting parameters. There also are more recent SED fitting codes that allow to set more free parameters, and set the fit for different components. MAGPHYS is the best publicly available SED fitting code as it provides the estimation of  $M_*$  and SFR that we need, providing also the point spread functions (PDF) for each property, and it shows to perform well in fitting the dust of galaxies CHANG+15, which is very important in this study, since merging galaxies at late stages show to be very dusty.

## 1.5 Identifying AGNs

Active galactic nuclei (AGNs) are a very powerful source hosted in galaxies, their bolometric luminosities ranges from  $L_{bol} = 10^{44}$  to  $10^{48}$  erg/s. AGNs can be observed from X-ray to radio wavelengths, as their presence can affect the entire SED of a galaxy. However, AGNs can be obscured by dust in the hosting galaxy. Thus, to detect an AGN in a very dusty host galaxy, X-rays observations are necessary.

To identify an active galactic nucleus (AGN) in our merging galaxies, we use three different methods. The first one is the well-known BPT diagrams (Baldwin et al., 1981), the diagnostic emission line ratios between the forbidden lines: [OIII], [NII], [SII], and [OI] and the Balmer lines:  $H_\beta$ ,  $H_\alpha$ . Kewley et al. (2006) summarised the different possible classifications of galaxies showing emission lines: star-forming (SF) galaxies, galaxies containing an AGN, LINER galaxies, and Seyfert galaxies. Figure 1.18 shows the three common BPTs. They compare the  $\log([\text{OIII}]/H_\beta)$  to the  $\log([\text{NII}]/H_\alpha)$  (left panel), to the  $\log([\text{SII}]/H_\alpha)$  (middle panel), and to the  $\log([\text{OI}]/H_\alpha)$  (right panel). The red lines separate the star-forming galaxies from the galaxies hosting an AGN (left panel), and from the Seyferts and LINERS (middle and right panels). There is also a composite separation (blue-dashed line in the left panel), that includes galaxies hosting an AGN but also star-forming. The blue lines in the middle and right panels show the separation and scatter of Seyfert and LINER galaxies.

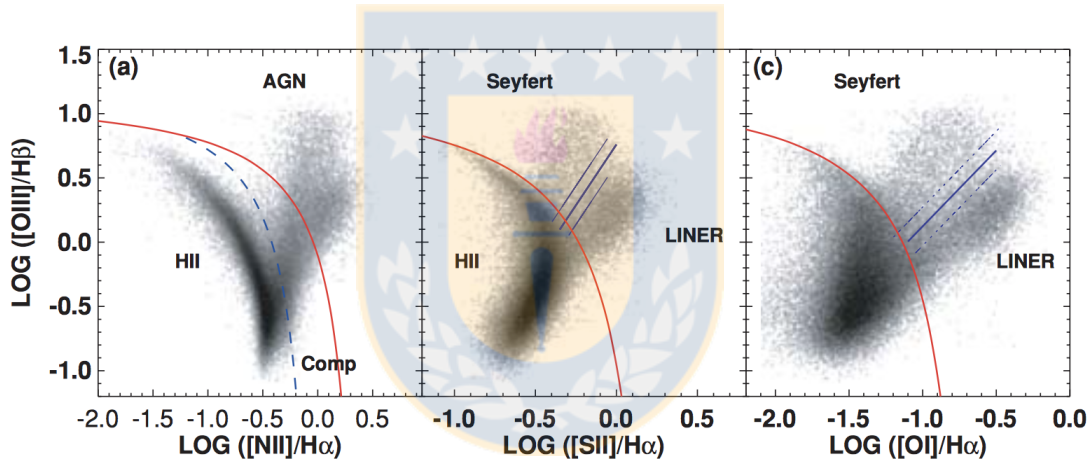


Figure 1.18 BPT diagnostic diagrams. BPT diagnostic diagrams summarised by Kewley et al. (2006). Lines of separation follow the equations shown in the text.

The lines of separation can be summarised as follows:

For the BPT-NII (left panel):

$$\log([\text{OIII}]/H_\beta) = 0.61/(\log([\text{NII}]/H_\alpha) - 0.05) + 1.3 \text{ (Kauffmann+03 line, in red)}$$

$$\log([\text{OIII}]/H_\beta) = 0.61/(\log([\text{NII}]/H_\alpha) - 0.47) + 1.19 \text{ (Kewley+01 line, in blue)}$$

For the BPT-SII (middle panel):

$$\log([\text{OIII}]/H_\beta) = 0.72/(\log([\text{SII}]/H_\alpha) - 0.32) + 1.30 \text{ (main AGN line, in red)}$$

$$\log([\text{OIII}]/\text{H}\beta) = 1.89\log([\text{SII}]/\text{H}\alpha) + 0.76 \text{ (LINER/Sy2 line, in blue)}$$

For the BPT-OI (right panel):

$$\log([\text{OIII}]/\text{H}\beta) = 0.73/(\log([\text{OI}]/\text{H}\alpha) + 0.59) + 1.33 \text{ (main AGN line, in red)}$$

$$\log([\text{OIII}]/\text{H}\beta) = 1.18\log([\text{OI}]/\text{H}\alpha) + 1.30 \text{ (LINER/Sy2 line, in blue)}$$

The second method we use is based in the emission line HeII (Shirazi & Brinchmann, 2012), which can be detected only due to sources with hard ionization radiation. This method is similar to the BPT but is shown that can detect more AGNs than the BPT. However, the BPT still can identify AGNs that the method using the HeII emission line does not. Figure 1.19 shows the HeII diagnostic diagram (Shirazi & Brinchmann, 2012), which compares  $\log([\text{HeII}]/\text{H}\beta)$  and  $\log([\text{NII}]/\text{H}\alpha)$ . The lines of separation are shown by Shirazi & Brinchmann (2012), as follows:

$$\log([\text{HeII}]/\text{H}\beta) = -1.22 + \frac{1}{8.92 \log([\text{OI}]/\text{H}\alpha) + 1.32} \text{ (composite line, dotted line)}$$

$$\log([\text{HeII}]/\text{H}\beta) = -1.12 + \frac{1}{8.92 \log([\text{OI}]/\text{H}\alpha) - 0.88} \text{ (main AGN line, solid line)}$$

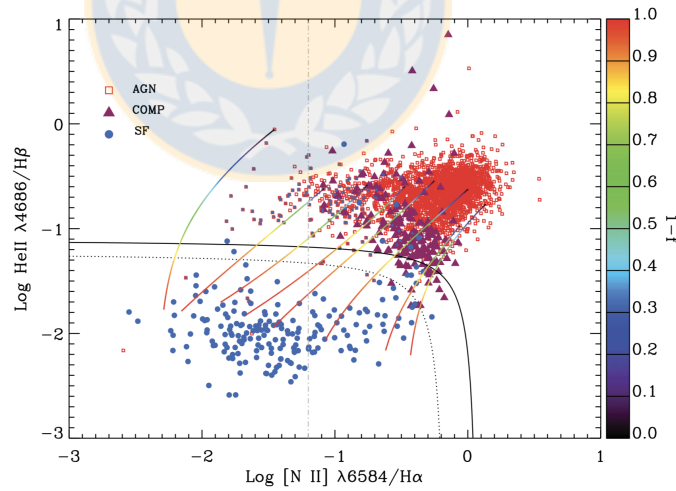


Figure 1.19 HeII diagnostic diagrams. HeII diagnostic diagrams summarised by Shirazi & Brinchmann (2012).

The symbols are coloured by the classification using the BPT, blue symbols represent star-forming galaxies, red symbols show galaxies with an AGN, and the magenta symbols are composite galaxies (star-forming and AGN). The lines coloured with a gradient (1-f) show the fraction of

the spectrum contributed by the star-forming galaxy, 0.0 (black) meaning that there is no fraction of SF present in the spectrum and 1.0 (red) means that the galaxy is highly star-forming.

The third method we use is the one based on WISE colours. Stern et al. (2012) and Jarrett et al. (2011) studied the  $W1-W2 - W2-W3$  diagram, finding that galaxies separate fairly clearly according to their SF, AGN content, and IR luminosity. The left panel of Figure 1.20 shows the diagram as presented by Cluver et al. (2014), where we can observe that ellipticals, spirals, starburst galaxies, (U)LIRGs, and galaxies with an AGN are reasonably separated. The right panel shows the separations to detect an AGN as shown by Stern et al. (2012) (dotted line) and Jarrett et al. (2011) (dashed polygon).

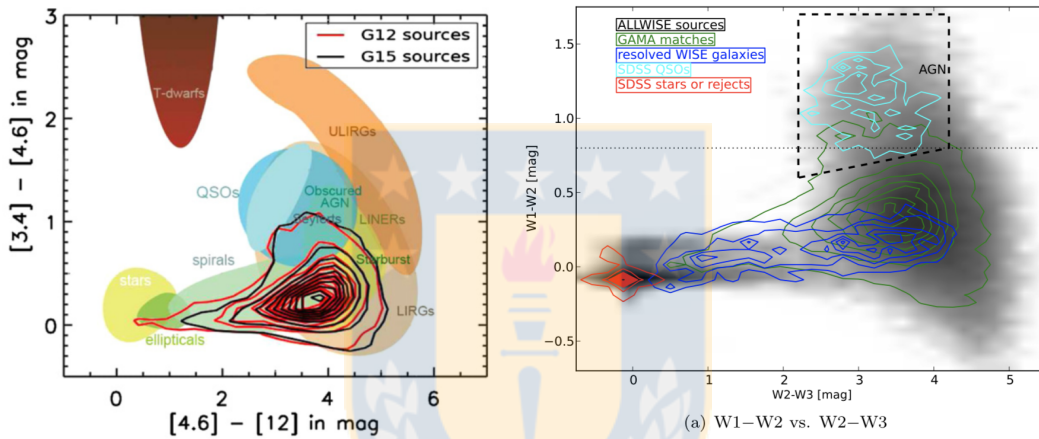


Figure 1.20 WISE colour-colour diagram. WISE colour-colour diagrams as shown by Cluver et al. (2014) (left panel) and Jarrett et al. (2011) (right panel).

The lines of separations follow the next equations:

dotted line:

$$0.8 \leq W1 - W2$$

dashed polygon:

$$2.2 < W2 - W3 < 4.2$$

$$0.1(W2 - W3) + 0.38 < W1 - W2 < 1.7$$

These three methods have their own pros and cons. For example, the emission lines come from the central region (3'') is more likely to be observing only the region where the AGN would be. However, this is tightly related to the distance to the galaxy, as the farthest the galaxy is located the more light from the galaxy is observed, and not only the center, where the AGN should be located. Thus, we increase the possibilities of observing regions with star formation plus the AGN.

Additionally, the emission lines are highly affected by dust and mergers at their final stages are usually very dusty. On the other hand, the WISE colour-colour diagram seem to separate unperturbed galaxies with an AGN well enough, but the relatively low resolution of WISE means that we are forced to use the colours of the entire galaxy, instead of only the nucleus, thus allowing us to only identify AGNs that outshine their host galaxy.





# 2

## Multi-band Photometry, Classification, Stellar Masses, and Star Formation Rates

### 2.1 Introduction

In this chapter, I present the assembly procedure and characteristics of the merging systems included in the final data sample. I classified these merging galaxies according to their morphology and merger stage in the merger process. After compiling the available information from the public surveys (GALEX, SDSS, and WISE), I noticed that the sizes show different values between the ones catalogued and the available images. Thus, I decided to perform the photometry on these merging galaxies to improve the estimates of stellar mass ( $M_*$ ) and star formation rate (SFR). The semi-automated photometric procedure is summarised in Section 2.3.2. In order to show the different results obtained using either a different photometry or estimator, I present comparisons to different public catalogues and relations available in the literature. As a matter of notation, we use ‘merger’ to denote a merging system of galaxies that includes one or more individual merging galaxies. This study has been included in Calderón-Castillo et al. (submitted, hereafter Paper I).

### 2.2 Sample and Data

#### 2.2.1 Sample Selection

Our sample has been drawn primarily from five large samples: the Arp’s Catalog of Peculiar Galaxies<sup>1</sup> (Arp, 1966) (Arp 1966; ARP Galaxies) containing 338 peculiar galaxies; The VV<sup>2</sup> Catalogue of Interacting Galaxies (Vorontsov-Velyaminov et al., 2001) with 852 interacting systems; the mergers classified by Nagar et al. (submitted) containing 81 mergers with sub-millimetric

---

<sup>1</sup><http://arpgalaxy.com>

<sup>2</sup>[www.sai.msu.su/sn/vv](http://www.sai.msu.su/sn/vv)

and gas information; the mergers classified by citizen scientists in the Galaxy Zoo (GZ) Project<sup>3</sup> (Holmbeck et al., 2016, GZ mergers) listing 3373 mergers; and the mergers selected from the Great Observatories All-sky LIRG Survey<sup>4</sup> (Sanders et al., 2003, GOALS), which includes 629 (U)LIRGs.

From these  $\sim 4000$  galaxies, we have selected  $\sim 600$  mergers, counting a merger only once even when it appears in multiple catalogues, obeying the following criteria:

- if the system contains two galaxies, both components must show a difference in redshift  $\Delta z < 0.002$  ( $\Delta v_{\text{rel}} < 500$  km/s), which will exclude most fly-bys or unrelated galaxies, and selecting systems that are more likely to eventually coalesce.

- the merger is not part of either a group or a cluster, so it can be considered as an isolated binary system.

- in order to have well sampled SEDs, we only select mergers having full photometric coverage from imaging: FUV and NUV from GALEX;  $u$ ,  $g$ ,  $r$ ,  $i$ , and  $z$  from SDSS; and W1, W2, W3, and W4 from WISE. Table B.1 lists the effective wavelength and detailed information of each filter.

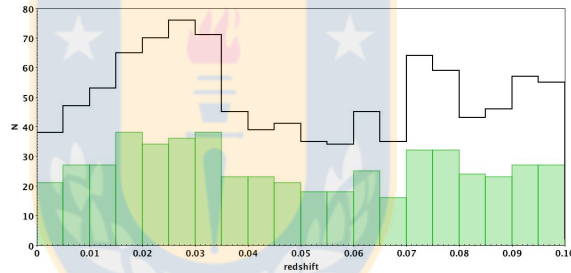


Figure 2.1 Redshift Distribution. The green filled histogram shows the redshift distribution of the 540 merging systems and the black histogram shows the distribution for all 919 individual galaxies in the merging systems. *Credits: Calderón Castillo P.*

The final sample contains 919 galaxies in 540 mergers. Since our galaxies are found in the SDSS, the majority of the sample is at  $z < 0.1$ , with a median value of  $z = 0.044 \pm 0.029$ . In Fig. 2.1 the redshift distribution of mergers is shown in green and for individual galaxies in black. The absolute-magnitude distribution of individual galaxies, shown in Fig. 2.2, has a median of  $-21.25 \pm 1.35$  mag in the  $r$ -band (SDSS).

Since the mergers have been classified based primarily on the SDSS imaging, where the sensitivity is  $24 \text{ mag/arcsec}^2$  in the  $r$ -band, we may miss merging features fainter than this value. Therefore inevitably, we may miss mergers at early- and late- merging stages, over-accounting for merging systems at intermediate stages.

<sup>3</sup><http://data.galaxyzoo.org>

<sup>4</sup><http://goals.ipac.caltech.edu>

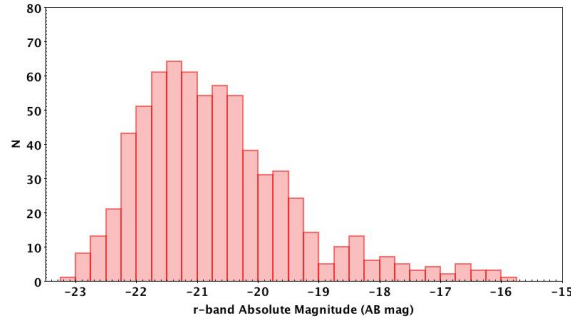


Figure 2.2 *r*-band Absolute Magnitude Distribution. SDSS *r*-band absolute magnitude distribution of all individual galaxies in the final sample. Credits: Calderón Castillo P.

A considerable bias of the GZ project is that the images they provide to the citizens for a visual inspection are relatively small, hence merging pairs with large separations are missed. Another bias that can be introduced in the GZ and/or our merging stage classification is that some of the late merging stages containing only one galaxy could have been an old interaction which did not result in a merger, where the secondary galaxy which passed-by is too far away to be considered as a companion.

### 2.2.2 Imaging Data

We compiled data from several surveys, spanning the UV, optical, and IR wavelengths. We gathered fully reduced imaging for FUV and NUV from GALEX<sup>5</sup> (GR6/GR7), obtaining images of 1.2° (1450 pixels) in radius. For SDSS<sup>6</sup> (DR13), we obtained images for the following optical bands: *u*, *g*, *r*, *i*, and *z* (10 x 13 arcmin<sup>2</sup>, which corresponds to 2048 x 1489 pixel<sup>2</sup>). Finally, we used 18.3x18.3arcmin<sup>2</sup> (800 x 800 pixel<sup>2</sup>) images for W1, W2, W3, and W4 from WISE<sup>7</sup>.

## 2.3 Results

In this section, we will present the classification distributions of the sample. Also, we will summarise our semi-automated photometry approach, the complications of an automated photometry and possible solutions. We will show the results of our photometry and compare them to available catalogs. Finally, we will compare our measurements of  $M_*$  and SFR to those in the catalogs and discuss the possible biases.

<sup>5</sup><http://galex.stsci.edu/data/>

<sup>6</sup><https://dr13.sdss.org/sas/dr13/>

<sup>7</sup><http://irsa.ipac.caltech.edu/applications/wise/>

### 2.3.1 Galaxy and Merger Sequence Classification

The 540 mergers of the final sample were classified by morphology and merging stage based on a visual inspection of the SDSS images (PCC). The morphological classes of the individual galaxies in the systems are: spiral, elliptical, lenticular (S0), and highly-disturbed. The latter classification includes all galaxies that are too disturbed to be clearly included in any of the other three classifications. An example of each classification is shown in Fig. A.1. Figure 2.3 shows the distribution of the morphology of the merging galaxies. A larger fraction of the sample (34%) is highly-disturbed. Most of these galaxies are likely to have been identified as spirals in the past as they presently show very disturbed tidal tails and nuclear regions. Other galaxies show shells, features often associated with mergers involving elliptical galaxies.

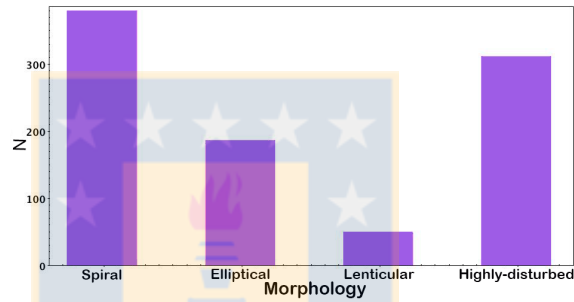


Figure 2.3 Morphology Distribution. The distribution of galaxy morphology for all individual galaxies in the sample: classifications are spiral, elliptical, lenticular (S0), and highly-disturbed. The latter classification describes galaxies that are too disturbed to be classified in any of the other classifications. *Credits: Calderón Castillo P.*

Some studies classify mergers based on their separation (Ellison et al., 2008, 2011, 2013; Darg et al., 2010). However, applying this criteria based on component separation does not necessarily imply that mergers are ordered in the correct merging time considering that the distance between the merger components depends on the mass ratio of the components and the particular orbital parameters of each merging system (e.g. relative speeds).

Thus, we based our classification on a more timeline-like merging sequence. Firstly, we applied the classification prescription in Veilleux et al. (2002, hereafter V02), and then further sub-classified using a new criteria defined in this work. V02 separates the merging sequence into five merging stages: I (*First Approach*), where the two galaxies are clearly separated but on course to collide, here we added the additional constraint that the velocity separation is  $\Delta z < 0.002$  ( $\Delta v < 500 \text{ km/s}$ ). II (*First Contact*), where the galaxies are overlapping but show no clear signs of disturbances in their morphology. III (*Pre-Merger*), where galaxies show strong tidal tails, bridges and/or shells but there are still two nuclei clearly observed. IV (*Merger*), where there is only one

nucleus visible (diffuse or compact) and the resulting galaxy shows a very disturbed morphology. V (*Old Merger*), where there is only one galaxy with no visible tidal tails but it shows a disturbed central morphology. Figure 2.4 shows the V02 classification scheme for a complete merging sequence as indicated below each image.

Our new merging sequence is based on V02’s sequence with additional separations tracing a more detailed timeline of the merging process allowing us to explore possible dependencies in more detail. We separate the merging stage III into 3 sub-stages: IIIa (*overlap*), the two galaxies overlap and show disturbances. IIIb (*disturbed*), the two galaxies show strong tidal tails, bridges and/or shells but they are clearly separated (not overlapping). IIIc (*double-nucleus*), an intermediate stage between stages IIIb and IV, where only one galaxy is observed as highly perturbed and shows two clear nuclei. We also separated the merging stage IV into two different stages following the V02 description but in a more visual way, since our galaxies are all in the nearby Universe. Merging stage IVa (*diffuse-nucleus*) shows a diffuse centre, and IVb (*compact-nucleus*) shows a compact nucleus. Figure 2.4 shows a representative example where our classification is indicated above each image.

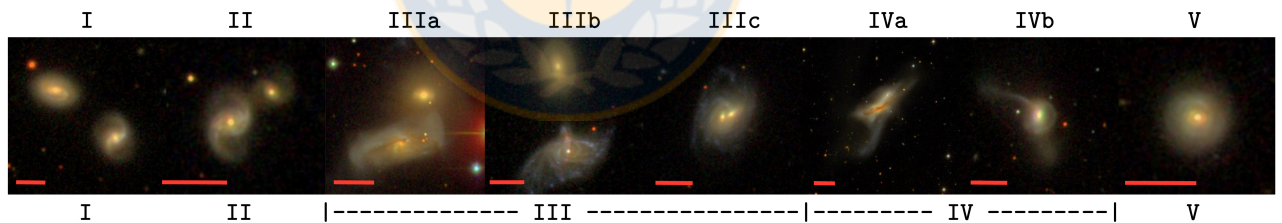


Figure 2.4 The Merger Sequence. SDSS images of an example merger from each merging stage defined in this study (top), and defined in V02 (bottom). Red lines represent 20” in each image.

Figure 2.5 shows the distribution of merging stages defined by V02 (blue) with our additional definitions (green inserts). Most of the mergers are classified in merging stage III, since this is the easiest stage in which to detect a merger because the merger features are most notorious at this stage.

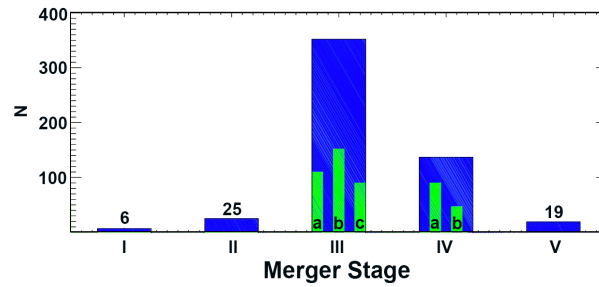


Figure 2.5 Merger Stage Distribution. Distribution of merger stages following the classification in V02 (blue), and our own classification (blue plus green). *Credits: Calderón Castillo P.*

### 2.3.2 Galaxy Photometry: Problems and Solutions

When visualizing the images using the WISE interactive website, it was immediately clear that the galaxies were often much larger than the radii listed in the WISE website tables. Figure 2.6 compares the radius measured on the WISE website using the interactive measuring tools to the semi-major axis ( $r_{semi}$ ) tabulated in the AllWISE extended sources catalogue, their semi-major axis ( $r_{semi}$ ) are always heavily underestimated in the AllWISE extended sources catalogues.

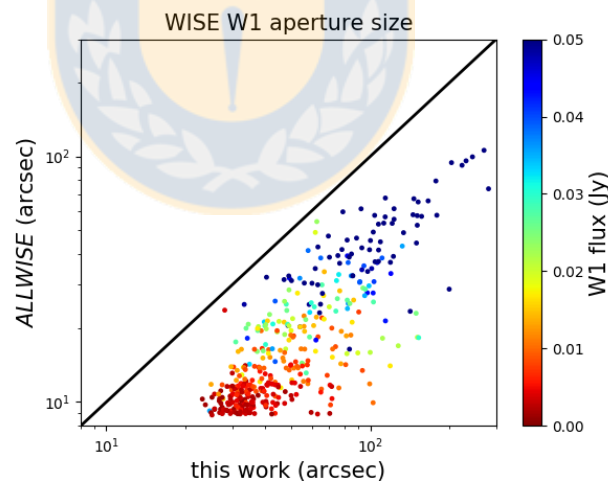


Figure 2.6 W1 radius Comparison. A comparison of the aperture radius we find is required to measure all of a galaxy's light in the WISE W1 images ( $x$ -axis, see text for details) to the  $r_{semi}$  of the AllWISE catalog. The line of equality is shown with a solid black line and galaxy symbols are coloured by their total W1 flux (in Jy) following the colour bar to the right. *Credits: Calderón Castillo P.*

These smaller radius measurements are likely linked to the low-sensitivity of 2MASS, which was used to estimate the apertures for the AllWISE catalog. This immediately shows that the

AllWISE catalog listed photometry of mergers is not accurate, and that the total luminosity is underestimated. For this reason, we decided to perform our own photometry, not just on the WISE imaging but across all the filters we use.

Another additional difficulty arising in mergers is that they can be so disturbed that the usual parameters used when making automated photometric measurements do not extract all the light from the galaxy. Disturbed morphologies, faint tidal tails, and luminous star-forming regions all have to be taken into account when measuring a merging galaxy's luminosity. Also, since the mergers don't show the same features along the merging sequence or often with each other, there is no unique set of parameters which can be used to perform the photometry automatically from system to system. Therefore, we are forced to perform the photometry for all the systems, and in all bands, almost completely manually. However, to aid efficiency, we have developed a semi-automatic procedure that we will now describe.

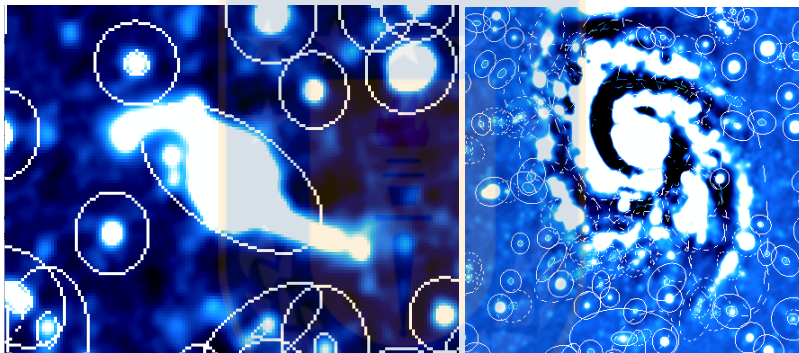
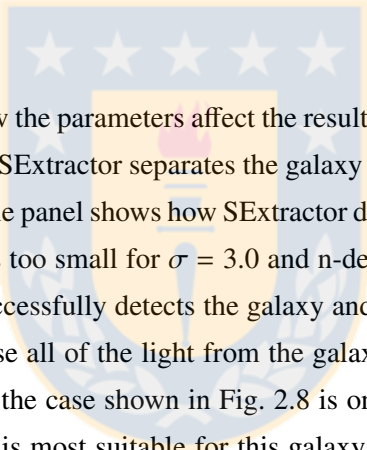


Figure 2.7 Different mergers need different photometry. An example of the danger of using the same automated SExtractor photometry on WISE images of the full sample. SExtractor was run with the same parameters on both examples shown. On the left, SExtractor finds an aperture which is smaller than the galaxy. On the right, SExtractor detects the different star-forming regions as separated galaxies and not a galaxy as a whole.

We started by performing the photometry in the WISE images, using SExtractor (Bertin & Arnouts, 1996). For example, as we apply commonly used values for the sky-threshold ( $3\sigma$ ) and deblending-threshold ( $n\text{-deblending} = 4$ ), we noticed that not all the mergers were included completely within the aperture, hence not all the light was extracted from the source by SExtractor (see Fig. 2.7, left panel). Also, for some galaxies, the same SExtractor setup extract only the light of a very bright star-forming region within the merging galaxy (see Fig. 2.7, right panel). Thus, we experimented with various values for the main SExtractor parameters, until we obtained a matrix of possible reasonable parameters (sky-threshold ( $\sigma$ ): 1.5, 3, and 5 and  $n\text{-deblending}$ : 2, 4, 8, 16, and 32). We then repeatedly ran SExtractor on each of our sources, applying each pair of values

from the matrix of SExtractor parameters and, in the process, obtaining 15 images per galaxy per filter.

Then each image and its resultant SExtractor apertures was checked visually (PCC) in order to choose the best SExtractor parameters for each individual galaxy. The best parameters are the ones that show an aperture that encompasses all of the light from the galaxy, avoiding contamination from other sources, and that does not exclude any star-forming region that belongs to the galaxy. In the case that the two individual galaxies were overlapping, we chose the parameters for which SExtractor shows an aperture that includes both galaxies in one aperture. This could happen in merger stages II and IIIa. We also confirm that the measured flux does not increase when we increase the size of the aperture in blank regions of the sky.



Some examples of how the parameters affect the result for one system can be found in Fig. 2.8. The top panel shows how SExtractor separates the galaxy into different regions for  $\sigma = 1.5$  and n-deblending = 4. The middle panel shows how SExtractor detects the central part of the galaxy only, making an aperture that is too small for  $\sigma = 3.0$  and n-deblending = 4. Finally, the bottom panel shows how SExtractor successfully detects the galaxy and correctly chooses an aperture which is sufficiently large to enclose all of the light from the galaxy for  $\sigma = 5.0$  and n-deblending = 4. It is important to stress that the case shown in Fig. 2.8 is only one example, and that the particular choice of parameters that is most suitable for this galaxy does not provide acceptable results for other mergers in our sample. More examples are shown in App. C. This highlights how redoing the photometry was a necessity for our mergers, and demonstrates that automated photometry on these type of complex sources is highly challenging.

Our photometric technique can be summarised as follows. We first check which parameters extract all the light from each galaxy in the WISE bands W1 and W4. After this we choose whichever is the larger aperture between W1 and W4 and use that aperture size for all filters. The location of the aperture in the rest of the filters is automatically found by SExtractor. In practice, we find that once the best set of parameters are found for a particular galaxy from the W1 image, running SExtractor with these parameters on the other filters results in similar detections. We visually check each filter to ensure that the sources were detected entirely and check for possible contamination, and rerun with alternative parameters from the set if necessary.



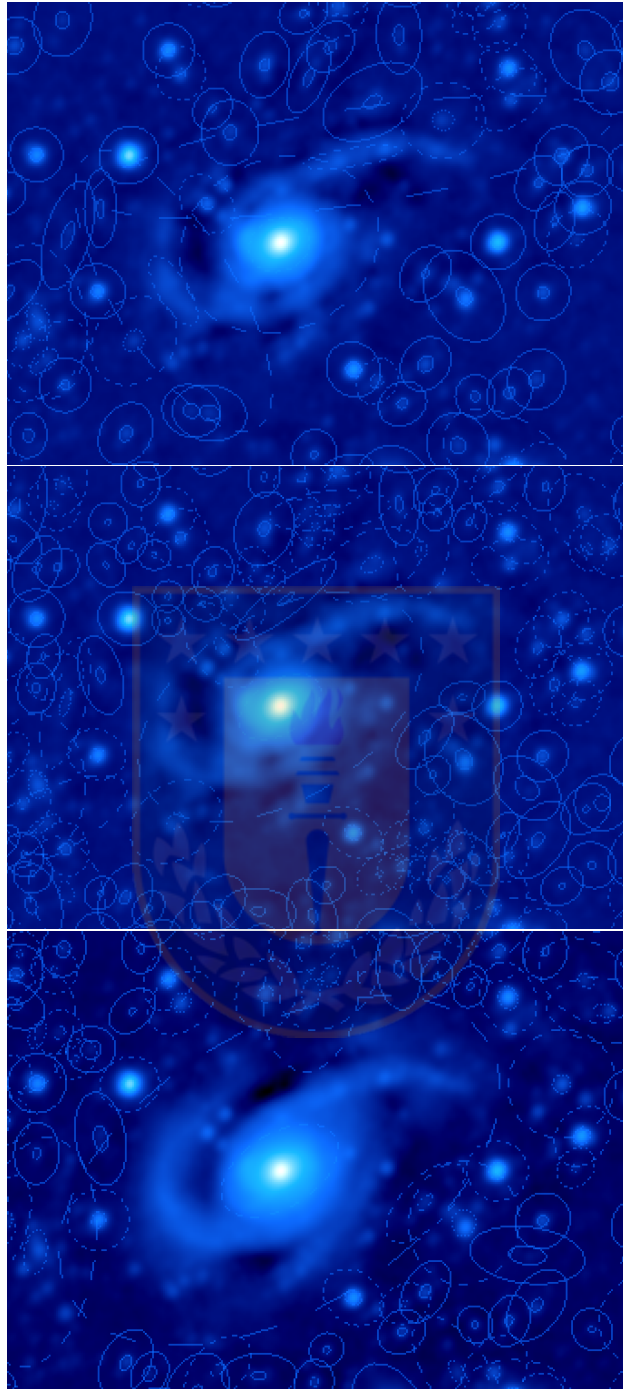


Figure 2.8 Changing the sky-threshold and n-deblending I. Examples of running SExtractor, with different parameters (changing sky- and deblending-thresholds), on the same galaxy. See text for details.

To show an example of how unreliable some catalogued measurements can be, we have se-

lected a merging galaxy and show the apertures from the different surveys and our aperture measured by SExtractor using the optimal parameters for this galaxy. Figure 2.9 shows 12 images, the first image is the SDSS *ugriz* image, following by the eleven filters we use: FUV, NUV, *u*, *g*, *r*, *i*, *z*, W1, W2, W3 and W4 (as described in the right-bottom corner of each image). For FUV and NUV, we show the aperture listed in the GALEX catalog in cyan. For the *ugriz* images, SDSS shows only one aperture size which is from the *r*-band aperture (in magenta), this value is also used by CHANG15 to correct their W1-3 fluxes. The aperture shown for this galaxy by SDSS is so small that it is barely seen on the figure. For the WISE filters, we show the *rsemi* values listed in the AllWISE catalog (in red). Finally, we show our measured aperture (green circle) on all the images. In this case, we have selected the aperture size measured for W4, since it is larger than that found for W1. We can see that for all the images the aperture used by the different catalogues are much smaller than the galaxy, while our aperture covers the entire galaxy in all the eleven filters.

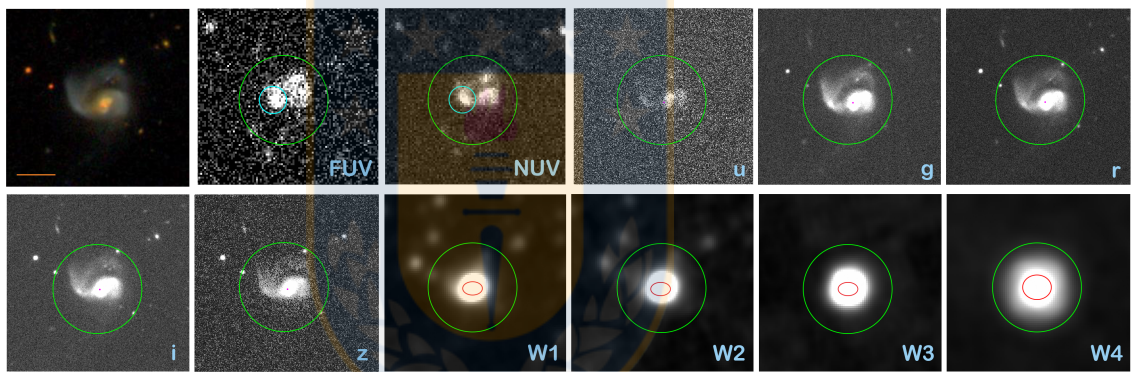


Figure 2.9 Example of aperture sizes from different surveys compared to our measurements. An example of the different apertures used by different surveys and our measurement in all the filters. The first image shows the galaxy in the SDSS *ugriz*-bands. The orange line represents  $20''$ . This SDSS image is followed by FUV, NUV from GALEX; *u*, *g*, *r*, *i* and *z* from SDSS; and W1, W2, W3 and W4 from WISE. Cyan apertures show the apertures shown on the GALEX catalog. Magenta apertures show the small aperture listed in SDSS tables, which is barely seen on the figure. Red apertures are the listed ellipses in AllWISE tables. The aperture we use for all filters, in this case measured from the W4 image, is shown in green.

The final fluxes have been corrected for Galactic extinction (Schlafly & Finkbeiner, 2011; Yuan et al., 2013) for all filters, except W3 and W4, for which Galactic extinction is negligible. They have also been corrected following each survey's specification. SDSS *u*- and *z*-bands need a correction of 0.04 and 0.02 mag, respectively, and an extra calibration of 8% for spiral and disk galaxies is needed for W4. In order to take possible systematic uncertainties into account, we have added 0.05, 0.02 and 0.1 mag in GALEX, SDSS, and WISE, respectively, to the statistical

uncertainties calculated by SExtractor. We have compiled useful information from the different surveys in Table B.1, in order to facilitate the use of the different parameters that are required in the photometry process.

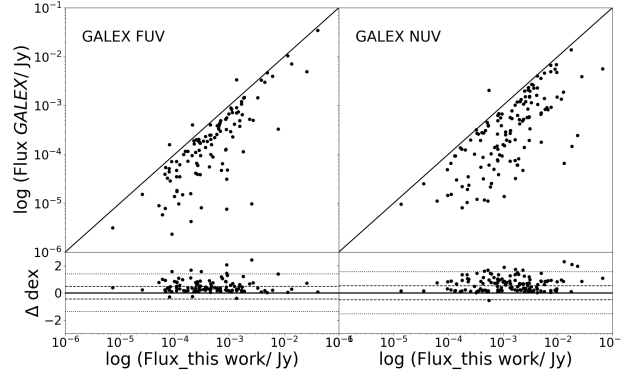


Figure 2.10 Flux comparison with GALEX. Flux comparison between our measured photometry and GALEX table's values. The black line shows equality. The y-axes show the GALEX FUV-NUV flux. The dashed- and dotted-lines show the 1- and 3- $\sigma$  from the one-to-one relation, respectively. Credits: Calderón Castillo, P.

The aperture fluxes measured by us are significantly different from those measured by previous authors. Figure 2.10 shows a comparison between our aperture fluxes ( $x$ -axes) for FUV (left panel) and NUV (right panel) and the respective values listed in the GALEX catalog. Most of the galaxies show higher fluxes for our measurements.

Figure 2.11 shows nine panels comparing our measured fluxes on the  $x$ -axis to CHANG15's fluxes. The five first panels (from left to right) show the comparison to SDSS MODELFLUX, the three following panels show the comparison to WISE W1-3 mpro fluxes corrected by the radius calibration shown by CHANG15, and the last panel shows the WISE W4 mpro flux which is not corrected by CHANG15. WISE W1-4 panels show that for some fraction of our sample, there are no measurements listed (see CHANG15's fluxes equal to 10 Jy). Thus, we have increased the number of useful data for this sample. For the first five panels, most of our fluxes are brighter than those listed as MODELFLUX as well as for W4 mpro. This is due to the larger apertures we use to measure the flux. For WISE W1-3 filters, we observed that CHANG15's values are systematically larger than our fluxes. This could be related to their correction that increases the flux depending on the radius in the r-band of the galaxy. This correction can be adding more flux than that needed for this type of galaxies, over-correcting the flux for these three filters. The fluxes are affected differently depending on the filter, which will not just create an offset but it will change the shape of the final SED.

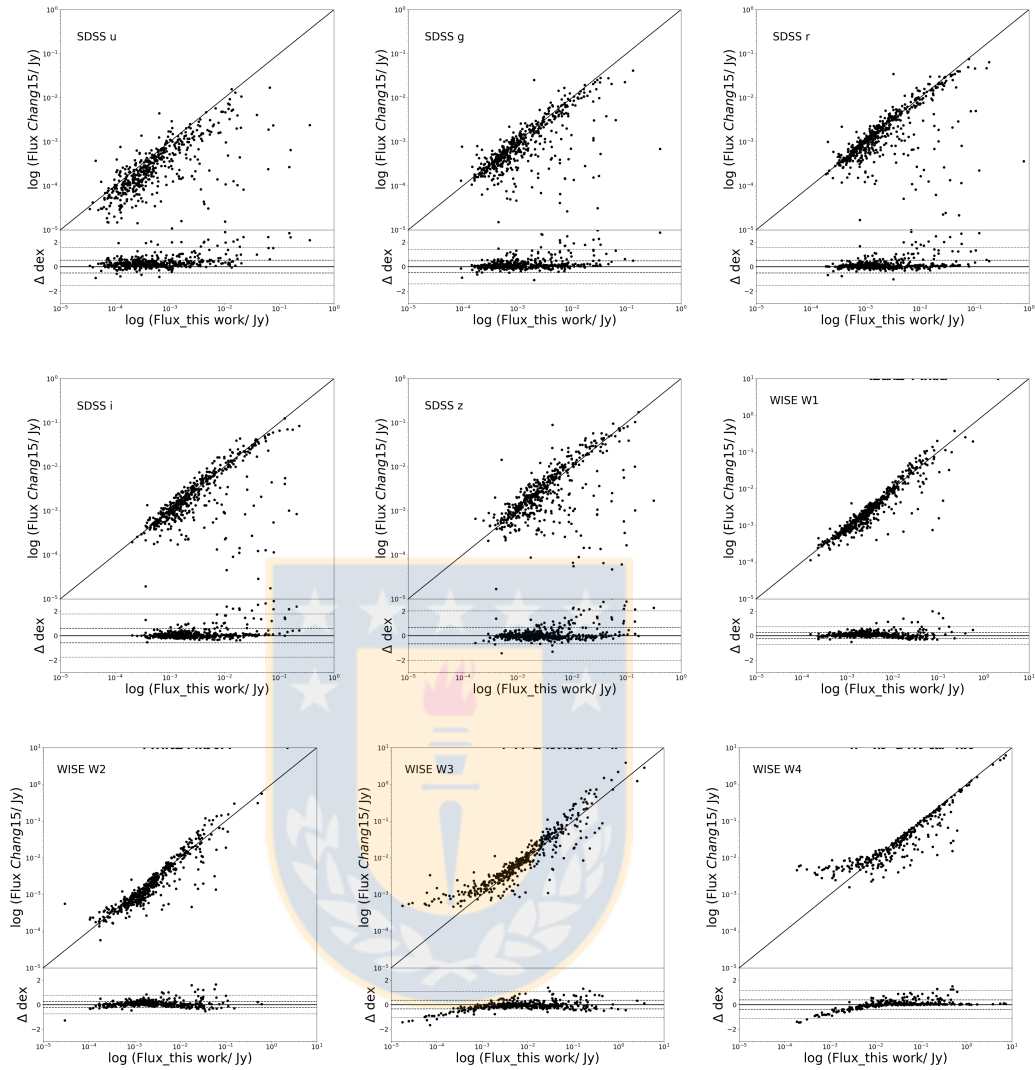


Figure 2.11 Flux comparison with SDSS and WISE *mpro*. A comparison of the aperture fluxes measured by us to those listed by CHANG15 for all galaxies common to our samples. Specifically we use the SDSS MODELFLUX values and the WISE *mpro* fluxes from CHANG15. The solid line in each main panel shows the line of equality and each small panel shows the difference between the two axes, respectively. Datapoints at the highest  $y$ -axis values in each main panel represent galaxies with fluxes measured by us but not by CHANG15. The dashed- and dotted-lines show the 1- and 3- $\sigma$  from the one-to-one relation, respectively. *Credits: Calderón Castillo, P.*

Figure 2.12 shows the comparison between the fluxes measured by SExtractor ( $x$ -axes) and AllWISE table `gmag`, which is recommended for extended sources by the WISE team. Our fluxes are higher than those listed in the AllWISE tables due to our larger apertures. For a small fraction of the galaxies at the faint end of W3 and W4 (6 and 10%, respectively), we see that our

measurements are lower than the listed in the AllWISE tables.

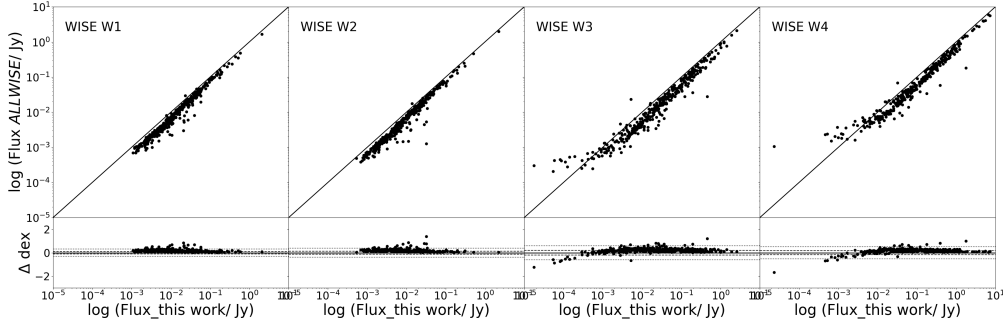


Figure 2.12 Flux comparison with SDSS and WISE  $g_{mag}$ . Flux comparison between our measured photometry and WISE table's values. The black line shows equality. The y-axes show the WISE  $g_{mag}$  flux conversion. The dashed- and dotted-lines show the 1- and 3- $\sigma$  from the one-to-one relation, respectively. Credits: Calderón Castillo, P.

Figure 2.13 shows the comparison between our W1 photometry measurements on the  $x$ -axis and the WISE table W1  $g_{mag}$  values (recommended for extended sources), coloured by the ratio between our aperture radius and the WISE table semi-major axis ( $r_{semi}$ ). This clearly shows the dependency of the measured flux on the aperture used during the photometry. For almost all galaxies our measurements give higher fluxes than those listed in the WISE table magnitudes, which is primarily due to our (more correct) larger apertures.

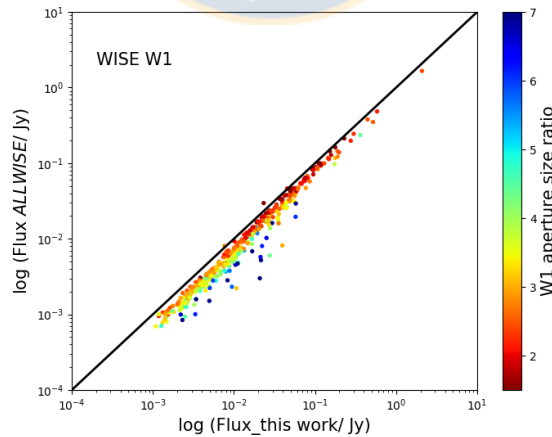


Figure 2.13 Flux comparison coloured by the radii ratio. Comparison of the total aperture flux (Jy) measured by us and that listed in the WISE tables for all galaxies in our sample. Symbols are coloured by the ratio of our measured aperture size to that applied by the WISE team, following the colour bar on the right, and the black line shows equality. Credits: Calderón Castillo, P.

The comparisons between our measured fluxes and the ones listed in GALEX, SDSS and WISE do not depend either on the morphology of the galaxies or the merger stage of the merger. Some of these comparisons can be seen in Fig. D.1.

### 2.3.3 MAGPHYS: SED fitting to obtain $M_*$ and SFR of mergers

We obtain our  $M_*$  and SFR using the publicly available SED fitting code, MAGPHYS<sup>8</sup> (da Cunha et al., 2008). This program fits photometric data from UV to submillimetric wavelengths. We have used the 2003 libraries recommended by their website, which assembles 50000 stellar population template spectra (Bruzual & Charlot, 2003) for the optical photometric library and other 50000 PAH+dust emission template spectra for the infrared photometric library. MAGPHYS models galaxy SEDs according to the redshift of the given sample and uses a Bayesian approach to interpret the SEDs so as to statistically derive different galaxy properties, such as  $M_*$ , SFR, dust mass, among other quantities.

In order to obtain more accurate estimations of the  $M_*$  and the SFR of our galaxies, our sample was chosen such that all mergers have available imaging covering the FUV, NUV,  $u$ ,  $g$ ,  $r$ ,  $i$ ,  $z$ , W1, W2, W3, and W4. When a merging galaxy did not show flux in some filter (occasionally FUV, NUV, or W4), we set the flux to  $-99.0$  and an uncertainty of  $3\text{-}\sigma$ . In this manner, MAGPHYS will consider this flux as an upper limit.

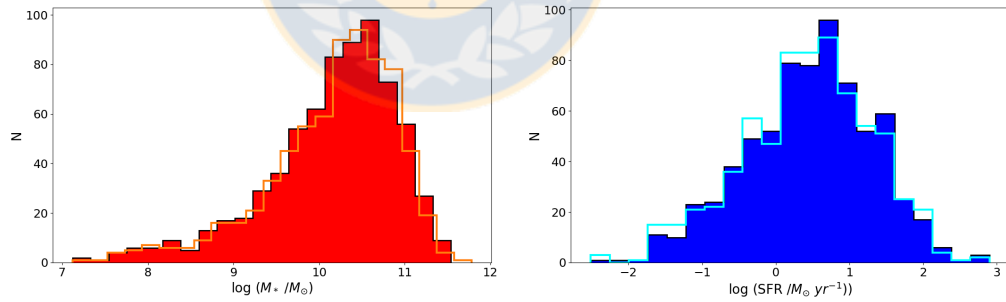


Figure 2.14 Stellar Mass and Star Formation Rate distribution. Distribution of  $M_*$  (left) and SFR (right) obtained by MAGPHYS, for all individual galaxies in our sample. The red and blue histograms show the  $M_*$  and SFR distribution using all the eleven filters and the orange and cyan histograms show the results using SDSS+WISE only. Credits: Calderón Castillo, P.

The SED fits show a median  $\chi_r^2 = 0.4$  and a mean of 1.9. Some SED fitting examples are shown in Fig. E.1. The left panel of Fig. 2.14 shows the distribution of the estimated  $M_*$  (in red), for our merger sample the median value is  $\log(M_*/M_\odot) = 10.28 \pm 0.76$ . The resulting SFR have a median

<sup>8</sup><http://www.iap.fr/magphys/>

of  $\log(\text{SFR}/M_{\odot}\text{yr}^{-1}) = 0.51 \pm 0.86$  with the distribution shown in the right panel of Figure 2.14 in blue.

We have also estimated  $M_{*}$  and SFR using only the optical and NIR data, in order to compare these results to CHANG15's catalog where they use the same more limited numbers of filters. For this sample, we obtain a mean and a median of  $\chi_r^2 = 1.7$  and 0.25 for the SED fits. A lower  $\chi_r^2$  could result because MAGPHYS finds it easier to fit to fewer data points but also the fits may be less accurate since it is missing information from the young population of the merging galaxy. When we include GALEX data, both  $M_{*}$  and SFR estimates are very similar to the ones derived using SDSS+WISE only (orange and cyan histograms in Fig. 2.14, respectively).

In Figs. E.1 and E.2, we show some examples of the SED fits for the sample using all eleven filters and SDSS+WISE only, respectively.

### 2.3.4 $M_{*}$ and SFR comparison to other catalogs

We compare the results obtained by MAGPHYS using all the filters with those obtained using only SDSS+WISE (see Fig. 2.15). We can see that they correlate and have a scatter of 0.1 dex for  $M_{*}$  (left panel) and 0.2 dex for SFR (right panel), with no apparent systematic offsets. The scatter may be larger for SFR compared to  $M_{*}$  because UV is a sensitive tracer of recent star formation. This means that including GALEX may not cause large differences in measurements for the majority of the sources but it can lead to differences as large as 10 and 15 times for  $M_{*}$  and SFR, respectively, in individual galaxies.

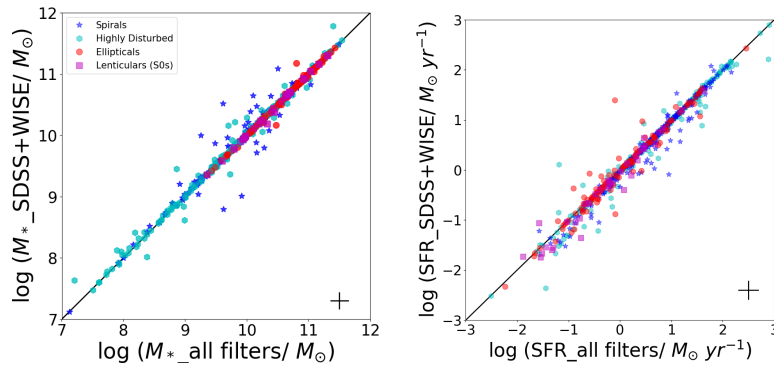


Figure 2.15  $M_{*}$  and SFR comparison to limited filters. Comparison of the  $M_{*}$  (left) and SFR (right) estimated by MAGPHYS when using all filters (see text) in the  $x$ -axis and only SDSS+WISE filters in the  $y$ -axis. The typical error is shown in the bottom-right corner of each panel. The sample is coloured by morphology as indicated in the legend. Credits: Calderón Castillo, P.

We coloured the merging galaxies by morphology in order to look for dependencies. Spirals are shown as blue stars, highly-disturbed galaxies are shown as cyan hexagons, ellipticals are shown as red circles, and lenticular galaxies are shown as magenta squares. The scatter in  $M_*$  is dominated by spirals and highly-disturbed galaxies. In comparison to the SFR, where the scatter is similar for all morphologies.

Figure 2.16 shows the comparison between our  $M_*$  (top) and SFR (bottom) results and the values listed in the CHANG15 (left), MPA-JHU (middle), and NSA (right) catalogues. We cross-matched our mergers to this catalogue using a distance limit of  $5''$ , where all coordinates come from SDSS. In the case of overlapping galaxies, we considered the one with the minimum distance.

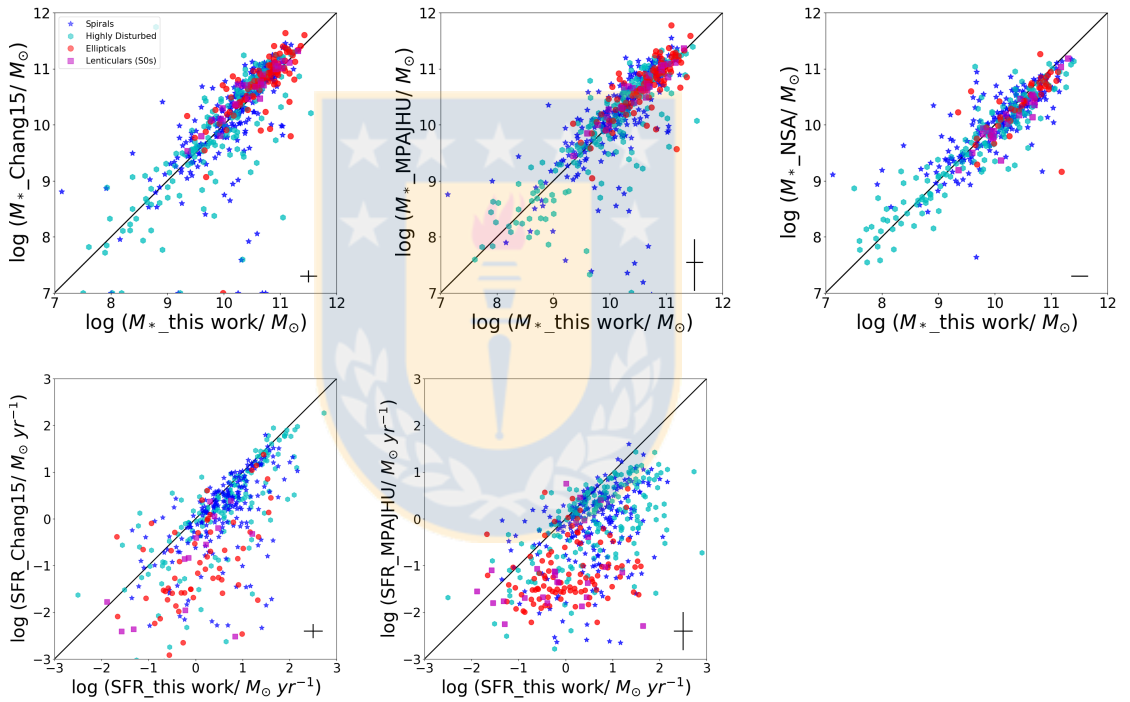


Figure 2.16  $M_*$  and SFR comparison to catalogues. Comparison between our  $M_*$  (top panels) and SFR (bottom panels) estimates to the estimates listed by CHANG15 (left panels), MPA-JHU (middle panels), and NSA (right panel). NSA does not list SFR in their catalog. The typical error is shown in the bottom-right corner of each main panel. Datapoints at the lowest y-axis values in the top-left panel represent galaxies with the minimum value set by CHANG15. These datapoints are not considered for the fits. The merging galaxies are coloured by morphology as shown in the legend. Credits: Calderón Castillo, P.

Since we have the SDSS+WISE results, we can directly compare our results to CHANG15's values (see Fig. 2.16 left panels). In both cases MAGPHYS is used to estimate  $M_*$  (top panel) and SFR (bottom panel). The only difference is that CHANG15 used the measurements shown in



SDSS and AllWISE tables with an additional correction for W1-3 fluxes based on the aperture size in the SDSS r-band, whereas we use our own semi-automated photometric approach. Thus, any differences that arise are primarily a result of the photometric methodology. Stellar masses show good agreement for most of the sample with a scatter of 0.5 dex, considering only CHANG15's sources with  $M_* > 10^7 M_\odot$ , and a scatter of 0.76 dex for SFR, considering only CHANG15's sources with  $\text{SFR} > 10^{-3} M_\odot \text{yr}^{-1}$ . The comparisons of  $M_*$  and SFR show no dependency on merger stage or separation (see Fig. F.1). The comparison of SFR show a large scatter, which indicates that SFR are more affected by small differences in photometry compared to  $M_*$ . There are many galaxies with very low SFR estimated by CHANG15, which can be underestimations of this property due to either or both i) the UV emission is not considered and ii) over-corrections of the W1, W2, and W3 fluxes. This leads to changing the SED shape affecting the  $M_*$  and SFR estimates, resulting in differences up to 500 times in  $M_*$  and 5000 times in SFR.

We also compare our results to catalogs using a different approach to estimate  $M_*$  and SFR. From here on we only use our results obtained by MAGPHYS using all of our filters (GALEX, SDSS, and WISE) on the  $x$ -axis in our figures and analysis.

The MPA-JHU estimated  $M_*$  and SFR, among other properties. The  $M_*$  were estimated within the 3'' fibre spectra and extending it for the entire galaxy based on the SDSS *ugriz* galaxy photometry, using a Bayesian approach, and the model grids shown by Kauffmann et al. (2003), applying an additional correction for the nebular emission contribution to the photometry based on the spectra. The SFR were estimated from the spectra and photometry, depending on the presence of an AGN content and the strength of the emission lines. For galaxies with strong emission lines, the SFR within the 3'' fibre was obtained using the nebular emission lines as described by Brinchmann et al. (2004) and, beyond the fibre, the SFR was calculated using the photometry based in Salim et al. (2007). For galaxies containing an AGN and galaxies showing weak emission lines, the SFR was calculated based on the optical photometry only.

Comparing our results to the MPA-JHU tables, we observe that the  $M_*$  show a scatter of 0.5 dex (the top-middle panel of Fig. 2.16). We also observe galaxies with 100 - 1000 times smaller  $M_*$  compared to our results. Lower  $M_*$  values are probably the result of lower luminosities measured in optical filters. Since MPA-JHU uses the SDSS tables to derived  $M_*$  and SFR, their SDSS fluxes are lower than our photometric measurements, as shown in Sec. 2.3.2. On the other hand, MPA-JHU SFR estimates show no clear correlation with our SFR results (the bottom-middle panel of Fig. 2.16). The scatter of a linear fit to the datapoints is 0.9 dex and some SFR estimates can be as much as 10000 times smaller than our estimates. MPA-JHU estimates their SFR based in the 3'' spectra corrected by their optical photometry. This correction was based mostly on unperturbed galaxies, thus we might consider that this could lead to large problems when considering highly

perturbed galaxies like mergers.

The NASA SLOAN Atlas (NSA) provides images, measurements and derived properties of  $\sim 140000$  nearby galaxies with available GALEX and SDSS photometry, and emission lines measurements. Stellar masses were calculated using the k-correction fit, similar to Kauffmann et al. (2003).

Figure 2.16 (right panel) shows the comparison between our  $M_*$  and NSA catalogued  $M_*$ . The  $M_*$  correlate but show a large scatter (0.4 dex), with differences up to 100 times our own estimates. These differences are likely related to the lower fluxes for GALEX and SDSS photometry that NSA uses to obtain their  $M_*$ .

The comparison between our  $M_*$  and SFR results and these 3 catalogues show similar dependency on morphology. The correlation does not clearly depend on morphology but the scatter of  $M_*$  is dominated by spirals and highly-disturbed galaxies. For the SFR, a large fraction of spirals and highly-disturbed galaxies are close to the one-to-one relation. However, there is still a large scatter, similar to ellipticals and lenticular galaxies.

We made a linear fit to the distribution of datapoints in Fig. 2.16. The parameters of the best fit and the scatter about that fit are provided in Tab. 6.1.

Table 2.1 List of the best fit parameters obtained from the comparison between our  $M_*$  and SFR results and the ones listed in each catalogue. *Credits: Calderón Castillo, P.*

	Catalogue	slope	intercept	scatter
$M_*$	CHANG15	0.89	1.07	0.49
	MPA-JHU	0.92	0.82	0.53
	NSA	0.79	2.05	0.44
SFR	CHANG15	0.81	-0.42	0.76
	MPA-JHU	0.56	-0.62	0.88

Comparisons to MPA-JHU and NSA catalogues are complex, since these use different approaches to estimate  $M_*$  and SFR. However, we can investigate some of the reasons for the differences observed between our results and CHANG+15's. In order to better understand the largest differences between our results and CHANG+15, we have plotted the SEDs of some galaxies showing some of the largest differences.

Figure 2.17 shows the SEDs of the galaxies shown in Figure 2.16 marked with the same symbol as the one at the top-right corner of each SED. Next to each SED, we show the *ugriz* image of each galaxy with the aperture we use in green, and the SDSS aperture used by CHANG+15 in magenta.

From top to bottom:

◇ Most of the fluxes shown by CHANG+15 are very similar to our measurements, even when

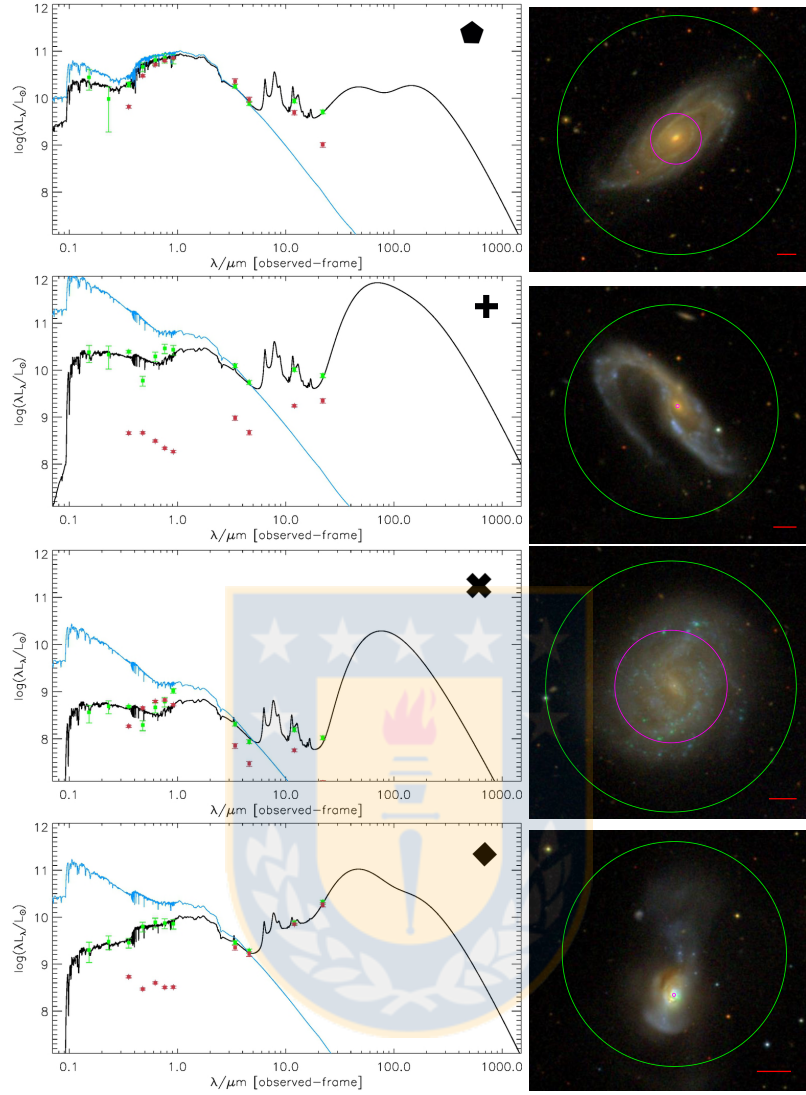


Figure 2.17 SEDs of galaxies with the largest differences to CHANG+15. SEDs and *ugriz* image for some examples of galaxies with large differences between our  $M_*$  and SFR results to CHANG+15's. The symbol shown in the top-right corner of each SED represents the galaxy's symbol in Figure 2.16. The black and blue lines show the attenuated and unattenuated SED fitted to our measurements in green. The red dots show the fluxes used by CHANG+15. The *ugriz* image show the apertures measured in our study in green and the one measured by SDSS in magenta. The red line represents  $20''$  in each image. *Credits: Calderón Castillo, P.*

their aperture is much smaller than ours. However, the *u* and W4 shows lower values for CHANG+15. This can be the reason why their SFR value is much lower than ours, since these wavelengths show the emission and re-emission of young star formation, respectively.

✚ shows a galaxy that had not been measured accurately either by SDSS or WISE. The SDSS

aperture is very small, barely seen in the *ugriz* image. Thus, the  $M_*$  and SFR values are very different between ours and CHANG+15's.

✖ The SDSS photometry shows a very different shape for the SED. However, the fluxes are not very different at these wavelengths. On the other hand, CHANG+15 shows lower fluxes for WISE compared to ours. Furthermore, there is no W4 flux shown by CHANG+15. The similarity in the SDSS fluxes might originate the similarity in  $M_*$  and the higher WISE fluxes of our measurements can explain our higher SFR estimate.

Finally, ◇ shows a very small aperture for SDSS, showing very low fluxes compared to our measurements. For WISE, however, the measurements are very similar. This results in very different  $M_*$  and SFR estimates.

This shows that there are several factors affecting the difference in the results; such as, differences in the photometric data of one survey compared to the other, low measurements in all of the filters, different measurements made in one or two filters which changes the shape of the SED. Hence, mergers must be studied with extreme caution if the catalogued values may be used.

### 2.3.5 Testing common estimators of $M_*$ and SFR

In this section, we consider how various  $M_*$  and SFR indicators perform on samples of mergers. The indicators we show in this section were derived using different methods than this study, but using some of the filters that we use. Thus, we can compare commonly used  $M_*$  and SFR indicators from the literature with our results measured using MAGPHYS. The  $M_*$  and SFR computed for this section were calculated using our new photometric values. We start by comparing  $M_*$  indicators.

We also contrast our MAGPHYS-derived  $M_*$  values with those estimated from one or two band photometry by Cluver et al. (2014, hereafter CL14), Bell et al. (2003, hereafter B03) and Taylor et al. (2011, hereafter T11). CL14 have studied two of their equatorial fields in the Galaxy and Mass Assembly (GAMA) Survey. They note that 'the typical W1  $1-\sigma$  isophotal radius is more than a factor of  $\sim 2$  in scale compared to the equivalent 2MASS  $K_s$ -band isophotal radius', and that WISE *gmags* should be used with caution since no deblending nor star subtraction has been made in WISE tables, which is further reason to apply our semi-automatic approach. They also show empirical relations between the  $M_*$  derived from synthetic stellar population models and W1 and W2 colours and W1 luminosity, which they separate into three equations following the form:  $\log M_{\text{stellar}}/L_{W1} = a(W1 - W2) - b$ , with  $L_{W1}(L_{\odot}) = 10^{-0.4(M_{W1}-3.24)}$ , where  $M_{W1}$  is the absolute magnitude in W1. For low-redshift sources,  $a$  and  $b$  are  $-2.54$  and  $0.17$ , respectively. For star-forming galaxies,  $a$  and  $b = 0.04$  and  $-1.93$ , respectively.  $a = -1.96$  and  $b = 0.03$  in the best-fit for the entire sample.

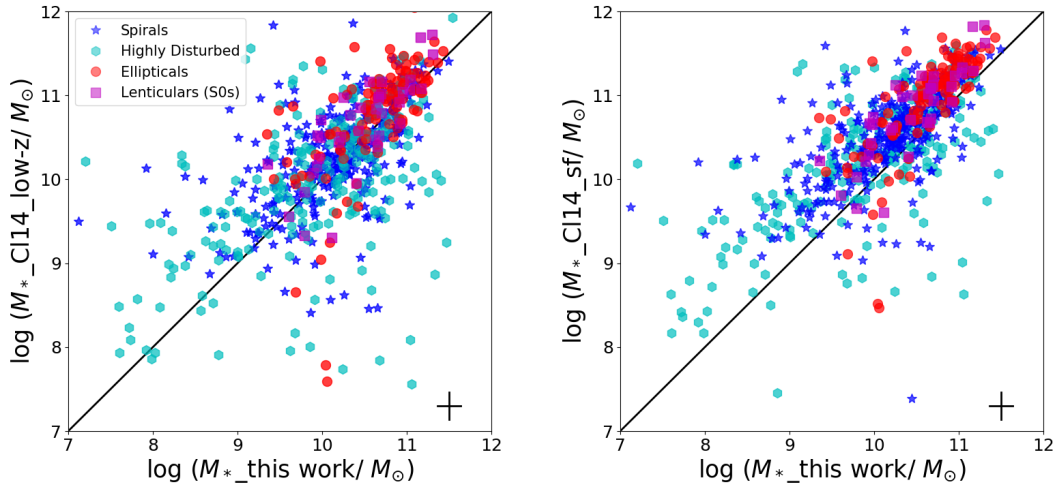


Figure 2.18  $M_*$  comparison to CLUVER14. Comparison of our  $M_*$  values (derived from our MAGPHYS fits to data in GALEX, SDSS and WISE filters) to those estimated using only WISE W1 and W2 photometry combined with the relations provided in CL14. The left panel shows the comparison to the relation for low-redshift sources, and the right panel shows the comparison to the relation for star-forming galaxies (see text). The typical error is shown in the bottom-right corner of each panel. *Credits: Calderón Castillo, P.*

Figure 2.18 shows the comparison between our  $M_*$  and the estimates using the CL14 relations. The left panel shows the  $M_*$  estimated using CL14's relation for low-redshift galaxies, and the right panel shows the  $M_*$  estimations using the CL14 relation for their entire sample, and using the star-forming relation for star-forming galaxies. Both methods tend to provide higher values of  $M_*$  compared to our results, and there is a large scatter in both methods (1.1 dex and 1.0 dex, respectively), leading to differences of up to a factor of 1000.

The correlations of these comparisons do not show a clear dependency on the morphology of the merging galaxies but the scatter is dominated by spirals and highly-disturbed galaxies.

The relation shown by B03 is frequently used, this relates the  $M_*$  to optical colours, following:  $\log(M_*/L_r) = -0.15 + 0.93(g-r)$ (1) and  $\log(M_*/L_r) = -0.306 + 1.097(g-r)$ (2) for galaxies in the range  $0.3 < (g-r) < 1$ , with  $L_r$  being the luminosity ( $L_\odot$ ) in the r-band. Figure 2.19 (left panel) shows the relation between  $\log(M_*/L_r)$  and the  $(g-r)$  colour. Equations (1) and (2) from B03 are shown in blue and green, respectively. Our best fit (in cyan) shows a steeper slope than for B03 sample:  $\log(M_*/L_r) = 0.9 + 1.69(g-r)$  and redder colours for a large fraction of our sample. This could be related to the higher dust mass of merging galaxies compared to unperturbed galaxies.

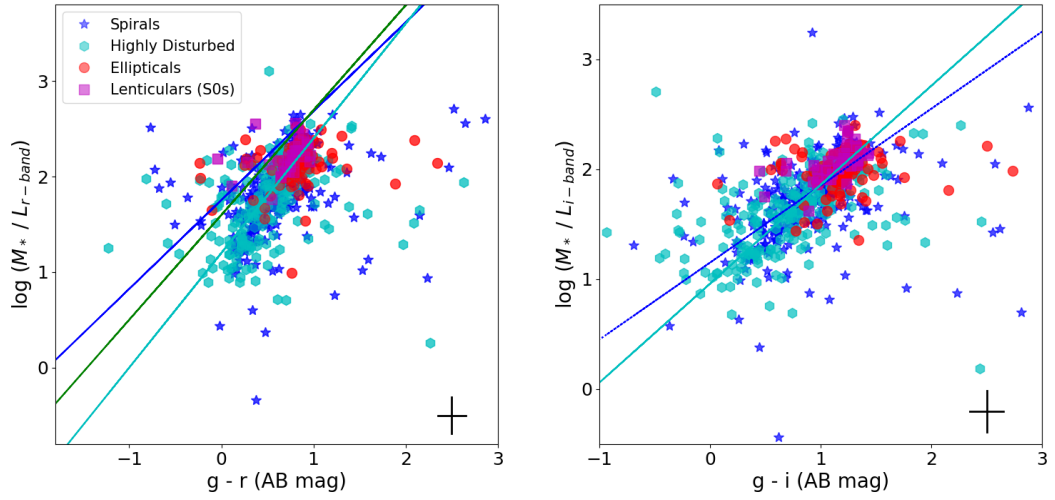


Figure 2.19  $M_*$  comparison to B03 and T11. The left panel shows the  $M_*$ -to-light ratio versus colour relation from B03. Blue line shows equation (1) and green line shows equation (2) from B03. Our best fit is shown in cyan. The right panel shows the  $M_*$ -to-light ratio versus colour relation from T11. Blue line shows  $M_*$ -colour relation from T11. Our best fit is shown in cyan. The typical error is shown in the bottom-right corner of each panel. *Credits: Calderón Castillo, P.*

Figure 2.19 (right panel) shows the relation between the  $M_*/L_i$  and the  $(g-i)$  colour. The blue line shows the relation determined by T11 for the GAMA sample:  $\log(M_*/L_i) = -0.68 + 0.70(g-i)$ , with  $L_i$  being the luminosity in the  $i$ -band in  $L_\odot$ . Our best fit shows a steeper slope:  $\log(M_*/L_i) = 0.96 + 0.90(g-i)$  but no offset with colour, suggesting a good correction for dust, as they also use near-infrared filters. This could be related to the span of their wavelength range for their SED fitting and hence, estimations. The large scatter could be due to different photometry used for their and our calculations.

These two relations do not show a clear dependency on morphology and the scatter is large for all morphologies. However, spirals and highly-disturbed galaxies show larger scatter compared to elliptical and lenticular galaxies.

We now compare our MAGPHYS-derived SFR results to those estimated by CL14, Lee et al. (2013), Jarrett et al. (2013), CHANG15, and Janowiecki et al. (2017, hereafter J17). CL14 also present a relation between a dust-corrected  $H_\alpha$ -derived SFR and W3 and W4 luminosities separately:

$$\log \text{SFR}_{H_\alpha} (M_\odot \text{ yr}^{-1}) = 1.13 \log \nu L_{W3} (L_\odot) - 10.24,$$

$$\log \text{SFR}_{H_\alpha} (M_\odot \text{ yr}^{-1}) = 0.82 \log \nu L_{W4} (L_\odot) - 7.3,$$

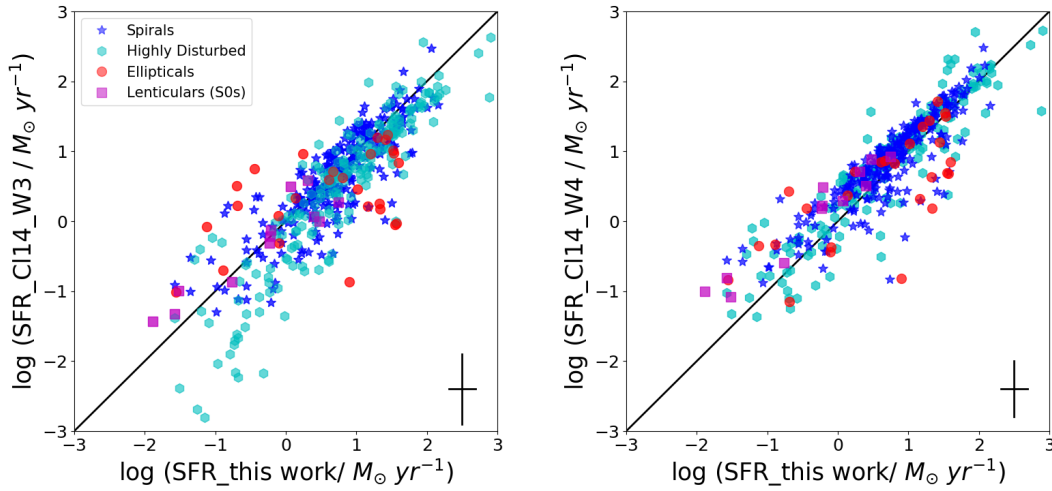


Figure 2.20 SFR comparison to CLUVER14. Comparison of our SFR values (derived from our MAGPHYS fits to data in GALEX, SDSS and WISE filters) to those estimated using only WISE W3 and W4 photometry combined with the relations provided in CL14. The left panel shows the comparison to the relation using W3, and the right panel shows the comparison to the relation using W4. The typical error is shown in the bottom-right corner of each panel. *Credits: Calderón Castillo, P.*

Figure 2.20 shows the comparison between our SFR and the estimates from CL14’s relations for W3 (left panel) and for W4 (right panel). CL14 SFR correlate closely to our results, showing larger scatters for SFR estimated from W3 compared to estimations from W4 (0.5 compared to 0.4, respectively). This could be related to the fact that W3 is more affected by PAH emission, as shown in previous studies (Jarrett et al., 2013, CL14, CHANG15). It is important to note that even if they seem to relate closely, the estimations can lead to differences of up to a factor of 50 for the W4 relation and a factor of 500 for the W3 relation.

The scatter in the results using the W3 relation is large for all morphologies. Nevertheless, a large fraction of spirals and highly-disturbed galaxies seem to be closer to the one-to-one relation. The comparison to the SFR using the W4 filter show no dependency on morphology.

The left panel of Fig. 2.21 shows the relation between the SFR and the luminosity in W4. We show different relations found in the literature. Lee et al. (2013) show two relations, a non-linear (red-dotted line) and a linear relation (red-solid line). The magenta line shows the relation found by Jarrett et al. (2013) and the green line shows the relation found by CHANG15. Our relation seems to be in between Lee et al. (2013) relations and CHANG15’s relation. There is a large scatter, showing higher SFR for the same  $L_{W4}$ , which might indicate that  $L_{W4}$  does not fully trace all the SFR of the galaxy. This result does not depend on the morphology of the merging galaxy.

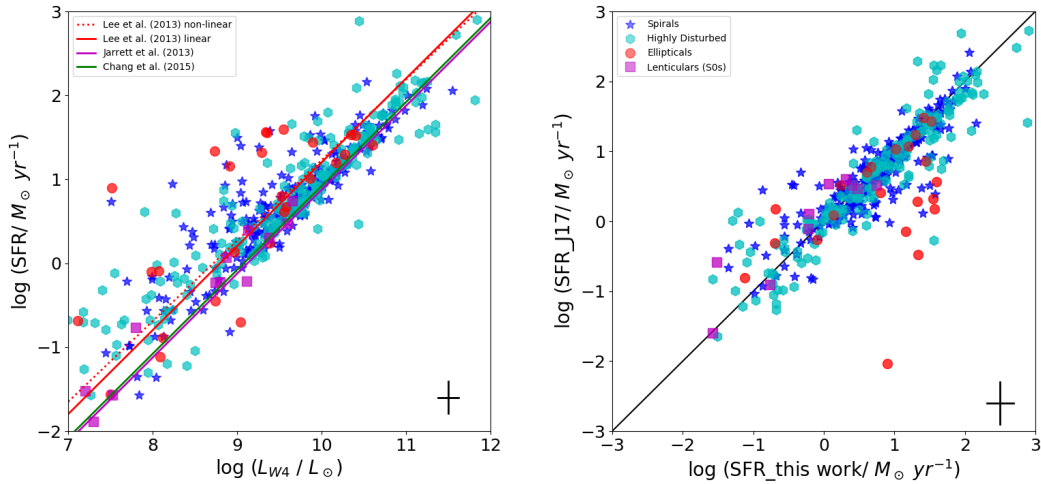


Figure 2.21 SFR comparison to the literature. Left panel shows the relation between the SFR and the W4 luminosity ( $L_{W4}/L_{\odot}$ ). The lines show different relations from the literature. The red-dotted line shows the non-linear relation found by Lee et al. (2013), while the red-solid line shows the linear relation from the same study. The magenta line shows the relation by Jarrett et al. (2013) and the green line shows the relation found by CHANG15. The right panel shows the comparison between our MAGPHYS SFR results and calculation using the SFR relation defined by J17. The black line shows the equality line. The typical error is shown in the bottom-right corner of each panel. *Credits: Calderón Castillo, P.*

Figure 2.21 right panel shows a comparison of the SFR we derive from MAGPHYS and that derived using the SFR estimator of J17. J17's approach combined the SFR from the NUV light and the attenuated light in W4, following:  $\text{SFR} = \text{SFR}_{\text{NUV}} + \text{SFR}_{\text{W4}}$ , with  $\text{SFR}_{\text{NUV}} (\text{M}_{\odot} \text{yr}^{-1}) = 10^{-28.165} * L_{\text{NUV}}(\text{erg/s/Hz})$  from Schiminovich et al. (2007) and  $\text{SFR}_{\text{W4}} (\text{M}_{\odot} \text{yr}^{-1}) = 7.50 \times 10^{-10} (L_{\text{W4}} - 0.04L_{\text{W1}}) (L_{\odot})$  from Jarrett et al. (2013) with an extra correction for stellar contamination. Both ours and J17's results show a tight correlation for a large fraction of the sample, except for galaxies with low SFR. The correlation and scatter are very similar for all morphological classifications.

### 2.3.6 The Colour-Morphology Relation

The mid-infrared colour-colour relation separates galaxies by morphology, luminosity and AGN content. Figure 2.22 shows the colour-colour relation (Jarrett et al., 2011; Cluver et al., 2014; Jarrett et al., 2017), which allows to identify galaxies with an AGN, ULIRGs and also separates galaxies by morphology, such as spheroids (ellipticals and lenticulars) and disks (intermediate and



star-forming). The lines shown in the figure follow the separations shown by CL14.

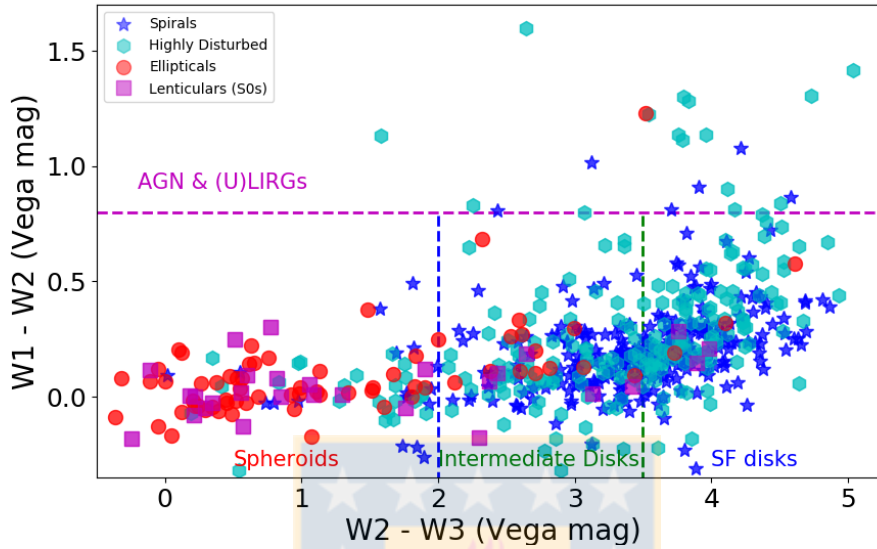


Figure 2.22 WISE colour-colour diagram. Showing the morphology separation as in Fig. 5 of CL14, where galaxies can be separated by Spheroids, Intermediate disks, star-forming disks and AGN and (U)LIRGs. We coloured our merging galaxies by morphology as indicated in the legend. Credits: Calderón Castillo, P.

We can see that, overall, merging galaxy morphologies differentiate similarly to unperturbed galaxies on the WISE colour-colour diagram. Elliptical (red) and lenticular (magenta) galaxies are mostly in the spheroids region, and spiral (blue) and highly-disturbed (cyan) galaxies are in the disk region. We can see a high number density of datapoints in the star-forming disk region where we expect to find spirals and starburst galaxies. It's also important to notice that as expected, merging galaxies can be found spread on this plot, we can see blue ellipticals and red spirals, as they change colour due to the merging process.

### 2.3.7 The Main Sequence and the specific star formation rate

The majority of galaxies follow a relation in the SFR- $M_*$  plane called the main sequence (MS; Elbaz et al. 2007, 2011, CHANG15). The scatter of this MS is  $\sim 0.4$  dex (CHANG15). Galaxies above this limit are forming stars 10 to 100 times faster than galaxies in the MS, these galaxies are called starburst galaxies. Galaxies below the MS region are not forming many stars, these galaxies are called passive galaxies.

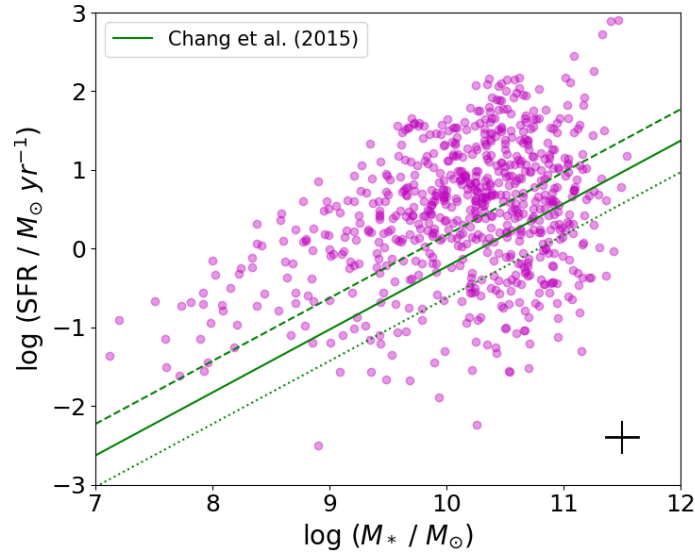


Figure 2.23 The SFR- $M_*$  plane. The green line shows the MS estimated by CHANG15, dotted- and dashed-green lines show a 0.4 dex from CHANG15's MS. The typical error is shown in the bottom-right corner. *Credits: Calderón Castillo, P.*

Figure 2.23 shows the SFR- $M_*$  plane of our sample and the MS found by CHANG15 (green line). The scatter of their MS is shown by the dashed- and dotted-green lines. CHANG15 also use MAGPHYS to estimate their  $M_*$  and SFR results, and they determined the MS for their sample. For this reason, this is the best MS available for studying our sample. Figure 2.23 shows that almost 60% of our merging galaxies are in the starburst region (above the green-dashed line).

How mergers move in this plane through their merging process will be shown in Chapter 3.

In order to look for a specific star formation rate (sSFR) indicator using one or two photometric bands, we look for a relation between this parameter and a combination between the stellar component and the dust/obscured star-forming component, which can be traced by the mid-infrared colour W1-W4 from WISE filters. Figure 2.24 shows the relation found for our merger sample, which follows the equation below:

$$\log(\text{sSFR}/\text{yr}^{-1}) = 0.34(\text{W1} - \text{W4}) - 11.42$$

with (W1-W4) in Vega magnitudes.

The scatter of this relation is similar for all morphologies except for lenticular galaxies, which show a smaller (0.2 dex) scatter compared to that shown by the other morphologies (0.5 dex).

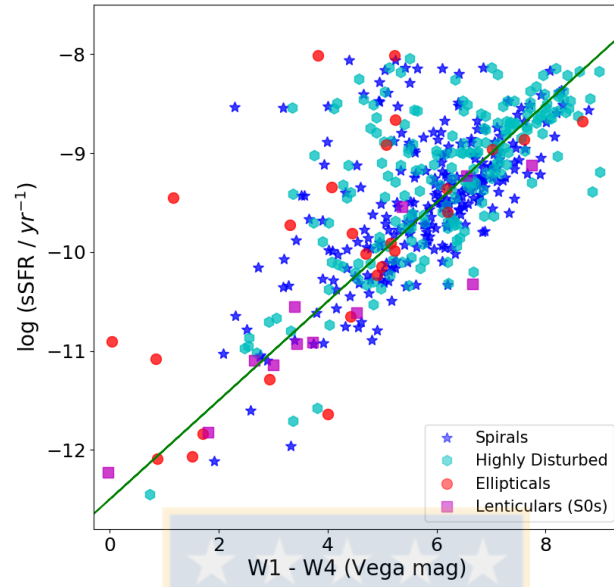


Figure 2.24 The sSFR - WISE colour relation for mergers. The green line shows the best fit to our sample (see text). The coloured symbols show the morphology of our merging galaxies as described in the legend. *Credits: Calderón Castillo, P.*

# 3

## Evolution of Star Formation and Accretion Activity during the Merging Process

### 3.1 Introduction

In this chapter, we study the star formation mode (SF mode) of merging galaxies during the merger process. Taking advantage of our new catalogue of isolated merging systems presented in the previous Chapter, we calculate the SF mode using stellar mass ( $M_*$ ) and star formation rate (SFR) estimates. We compare these values to the MS presented by Chang et al. (2015), and look for dependencies on any merger stage as classified in our timeline-like merger sequence. We also study the possible dependency between the SF enhancement and the morphology of the merging galaxy or of its companion. Finally, we present the AGN fraction at each merger stage. The AGN are identify using three different methods, two based in emission line ratios and the third based on the WISE colour of the merging galaxy. AGNs identified by any of these methods are consider AGN candidates. Thus, in this chapter when we refer to a galaxy hosting an AGN, we refer to an AGN candidate. Also in this chapter, we refer to merging galaxies as ‘galaxies’, and for unperturbed galaxies, we specify that we are referring to ‘unperturbed galaxies’. This study has been included in Calderón-Castillo et al. (submitted,b; hereafter Paper II).

### 3.2 Data

#### 3.2.1 The Sample

The merger sample has been assembled using five parent samples that include mainly mergers: the Arp’s Catalog of Peculiar Galaxies<sup>1</sup> (Arp, 1966, ARP Galaxies); the VV<sup>2</sup> Catalogue of Interacting

---

<sup>1</sup><http://arpgalaxy.com>

<sup>2</sup>[www.sai.msu.su/sn/vv](http://www.sai.msu.su/sn/vv)

Galaxies (Vorontsov-Velyaminov et al., 2001); the mergers classified by Nagar et al. (submitted); the mergers classified by citizen scientists in the Galaxy Zoo (GZ) Project<sup>3</sup> (Holmbeck et al., 2016, GZ mergers); and the mergers selected from the Great Observatories All-sky LIRG Survey<sup>4</sup> (Sanders et al., 2003, GOALS). From this set of catalogues, we have only selected mergers that are isolated, showing only one or two components, and that do not belong to either a group or cluster. In the presence of two components, we have restricted our selection to systems where their respective velocities are  $\Delta v_{\text{rel}} < 500$  km/s ( $\Delta z < 0.002$ ), to try to exclude fly-bys or galaxies that only appear close by projection effects. In this way, we try to select galaxy interactions that are more likely to eventually coalesce. We also restricted our sample by only including mergers with available imaging in all of the following filters: FUV and NUV from GALEX;  $u$ ,  $g$ ,  $r$ ,  $i$ , and  $z$  from SDSS; and W1, W2, W3, and W4 from WISE. Applying all these constraints result in 540 isolated mergers (919 merging galaxies in total) as our final sample. The redshift has a range up to  $z = 0.1$ . For more details please refer to Chapter 2.2.

The analysis presented here aims to understand the relation between the merger stage and the morphology of the components. We classified galaxies in four different types: spiral, elliptical, lenticular, and, in cases where none of those classes were applied, the galaxies were labeled as highly-disturbed (HD). This latter classification (HD) was also sub-classified either as late- or early-type. HD galaxies with gas (visible in their SDSS images as streams, tidal tails, and/or bridges and blue colour) are considered late-type galaxies. These dominate the HD sample by number. On the other hand, HD galaxies without gas (red mergers showing shells visible in the SDSS images) are considered as early-type galaxies.

The merger stages are based on the merger sequence shown by Veilleux et al. (2002), plus additional sub-classes that we introduced in Chapter 2. We have adopted eight different merger stages: *I (First Approach)*: the two galaxies are clearly separated but approaching to each other, following our  $\Delta v_{\text{rel}}$  condition. *II (First Contact)*: the two galaxies are overlapping with no strong perturbations. *IIIa (Pre-Merger overlap)*: the two galaxies are overlapping and showing strong perturbations. *IIIb (Pre-Merger disturbed)*: the two galaxies are clearly separated but showing strong perturbations. *IIIc (Pre-Merger double-nucleus)*: there is only one very perturbed object clearly showing two nuclei. *IVa (Merger diffuse-nucleus)*: one very perturbed object with a very diffuse nucleus. *IVb (Merger compact-nucleus)*: one very perturbed object with a very luminous and compact nucleus. *V (Old Merger)*: one galaxy with no strong perturbations but disturbed central morphology. Representative images of the morphology and merger stage classification can be seen in Figs. A1 and 9 described in Chapter 2, respectively.

---

<sup>3</sup><http://data.galaxyzoo.org>

<sup>4</sup>[Http://goals.ipac.caltech.edu](http://goals.ipac.caltech.edu)

### 3.2.2 Merging galaxies properties

In order to study the star-forming properties of mergers, we have estimated the  $M_*$  and SFR of these objects using the publicly available code MAGPHYS<sup>5</sup> (da Cunha et al., 2008). This code fits the spectral energy distribution (SED) of a galaxy based on photometric data, which can range from UV to submm. We have chosen the following surveys as they span a large range in wavelength, tracing young stars (GALEX), old stars (SDSS), and obscuration of young stars by dust (WISE). This allows us to determine  $M_*$  and SFR more accurately, taking advantage of the large, wide-field surveys that are publicly available. We have fitted SEDs to our entire sample, utilizing our own photometric measurements, that were measured using a semi-automated method. The semi-automated method allowed us to extract the entire merging galaxy's light, including faint tidal tails, and bright star-forming regions, which might otherwise be considered as distinct objects by a fully-automated method. This procedure was necessary since the automated measurements catalogued by the aforementioned surveys are found to be not reliable enough for merging galaxies, often showing systematically lower fluxes compared to our measured values (see Chapter 2 for more details).

## 3.3 Results

### 3.3.1 Stellar Masses

In order to look for biases in our study, we first considered the distribution of stellar masses separated by merger stages to search for any dependence. The top panel of Fig. 3.1 shows the  $M_*$  distributions of each merger stage, normalised by the number of objects at each merger stage, coloured as indicated in the legend. The stars and solid lines above the distributions show the median of each merger stage distribution. The range in  $M_*$  spans four orders of magnitude ( $7.5 < \log(M_*/M_\odot) < 11.8$ ) for the entire sample.

The bottom panel of Fig. 3.1 shows the median (blue dot), mean (green square), and the standard deviation (blue error lines) of the stellar mass according to merger stage. Medians for all eight merger stages fluctuate within  $10^{10.1}$  and  $10^{10.8} M_\odot$ . It seems there is a small decline in stellar mass related to the merger stage. However, the difference between the median  $M_*$  of the first merger stage (Merger Stage I) and the last merger stage (Merger Stage V) is only 0.5 dex, which can be considered negligible for our present study, and is smaller than the error bars on each data point. Thus, we can assume that there is no significant bias of stellar mass as a function of merger stage in our study.

<sup>5</sup><http://www.iap.fr/magphys/>

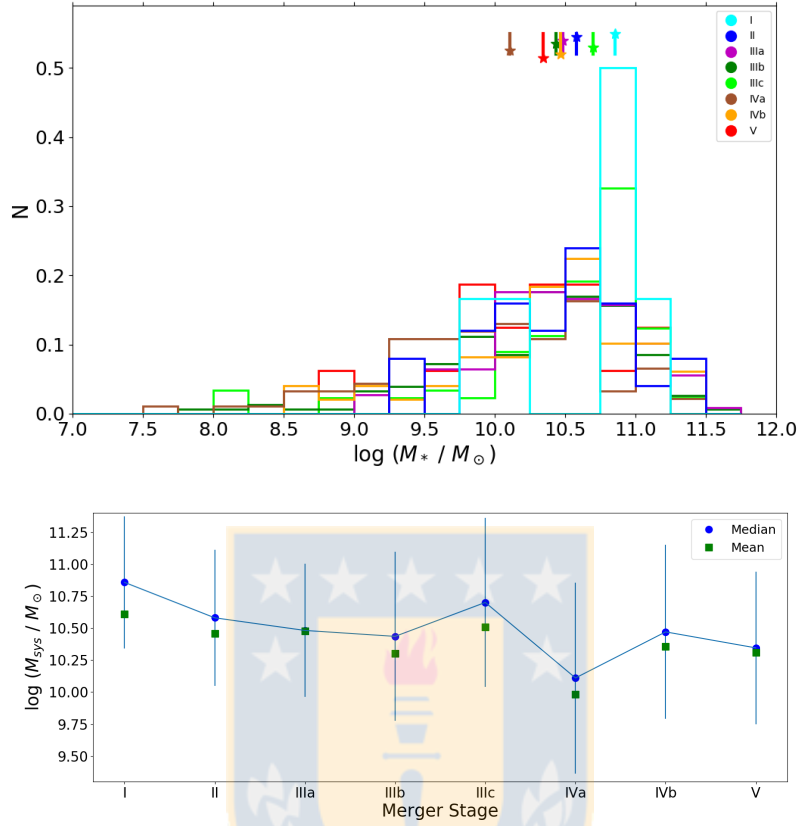


Figure 3.1  $M_*$  distribution at each merger stage. *Top*: Normalised stellar mass distribution for each merger stage. Each merger stage is coloured as shown in the legend. The stars and solid lines above the distributions show the median stellar mass of each merger stage. *Bottom*: The median (blue circles), mean (green squares), and standard deviation (blue error lines) of the stellar mass at each merger stage. *Credits: Calderón Castillo, P.*

For the SF mode analysis, we have separated our sample according to the stellar mass ratio between the interacting pairs, since the difference in stellar mass of the components can affect the resulting SF enhancement (Di Matteo et al., 2008; Hopkins et al., 2008; Park et al., 2017). We have adopted the definition of major merger when a system shows a stellar mass ratio up to 1:4 (Rodríguez-Gomez et al., 2015; Weinzirl, 2015; van de Voort et al., 2018). Figure 3.2 shows the stellar mass ratio distribution between the primary (most massive) and the secondary component. The mergers shown in this figure are the systems where both components are separated enough to be detected as different objects by SExtractor (not overlapping), thus have separated photometric measurements and individual  $M_*$  and SFR. The dashed line shows the separation between major and minor mergers. The effect on the SF mode caused by the stellar mass ratio of the components

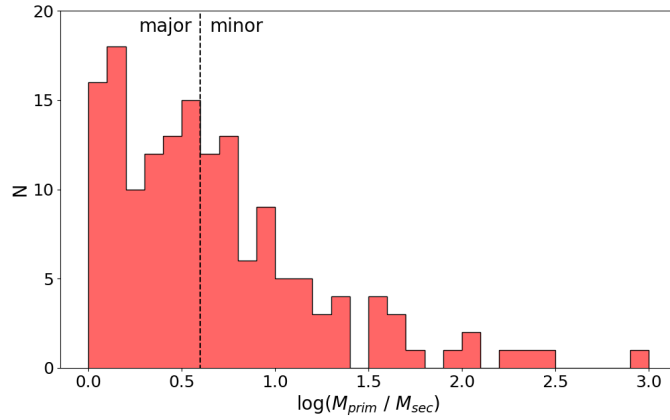


Figure 3.2  $M_*$  ratio distribution. Stellar mass ratio between the primary and the secondary component of the mergers showing two separated components. *Credits: Calderón Castillo, P.*

is presented in Sec. 3.3.3.

We have also separated the sample into different stellar mass bins in order to study how the stellar mass of a merger affects our results. For this, we have defined three stellar mass bins. The low- $M_*$  bin for stellar masses lower than  $\log(M_*/M_\odot) < 9.5$ . The medium- $M_*$  bin for stellar masses between  $9.5 < \log(M_*/M_\odot) < 10.5$ . The high- $M_*$  bin for stellar masses higher than  $\log(M_*/M_\odot) > 10.5$ . Since there are no clear dependencies on our results caused by the difference in stellar mass of the merger, we present these results in the App. G.1.

### 3.3.2 Evolution during the Merger Process: movement in the Main Sequence

Figure 3.3 shows the SFR- $M_*$  plane of mergers. The solid-magenta line shows the MS determined by Chang et al. (2015, hereafter CHANG+15):

$$\log(\text{SFR}/(M_\odot \text{yr}^{-1})) = 0.80 \log(M_*/10^{10} M_\odot) - 0.23$$

and the scatter of this MS (0.39 dex) is shown by dashed-magenta lines. All mergers within this scatter will be referred to as mergers within the MS. We have adopted this choice of MS because CHANG+15 uses the same SED fitting method (MAGPHYS) as our study to determine it. Other MS are presented in the literature such as Elbaz et al. (2007, 2011), but their  $M_*$  and SFR values are estimated using a very different approach (based on the SDSS fiber and optical filters) and so are less easily comparable with our own results. We note that, all of these MS are determined for the nearby Universe, over a similar redshift range as our sample. Thus, we are not concerned about evolution of the MS in the redshift range of our sample.

The top panel shows the merging galaxies coloured by morphology as shown in the legend.



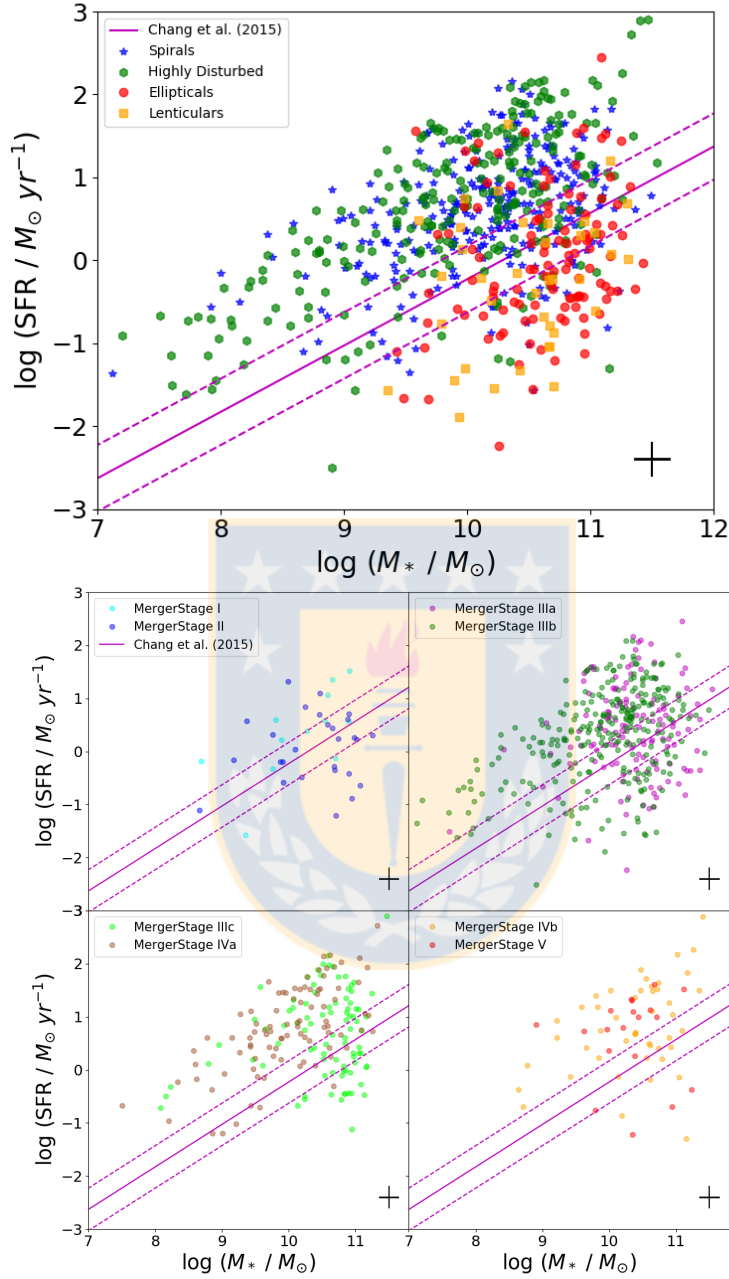


Figure 3.3 SFR- $M_*$  plane separated by morphology (top panel) and merger stage (bottom panel). The solid- and dashed-magenta lines represent the MS and the scatter determined by CHANG+15. The typical error is shown on the bottom-right corner of each panel. Credits: Calderón Castillo, P.

Spiral and HD galaxies (blue stars and green hexagons) are mainly located within the MS or above it. On the other hand, elliptical and lenticular (red circles and orange squares) galaxies cover all

three regions: above, within and below the MS but only at stellar masses higher than  $10^9 M_{\odot}$ . The bottom panel shows the SFR- $M_{*}$  plane separated by merger stage according to the legend in each sub-panel. Again, CHANG+15's MS is shown by the solid- and dashed-magenta lines. As shown in these sub-panels, there is no clear dependence on merger stage. Thus, to study the SF enhancement through the merger sequence, we calculated their SFR/ $M_{*}$  value, and determine their distance from the MS as given in CHANG+15. We refer to this distance as their SF mode, which can be positive (for objects above the MS) or negative for objects below the MS. We consider each galaxy's SF mode separated by their merger stage.

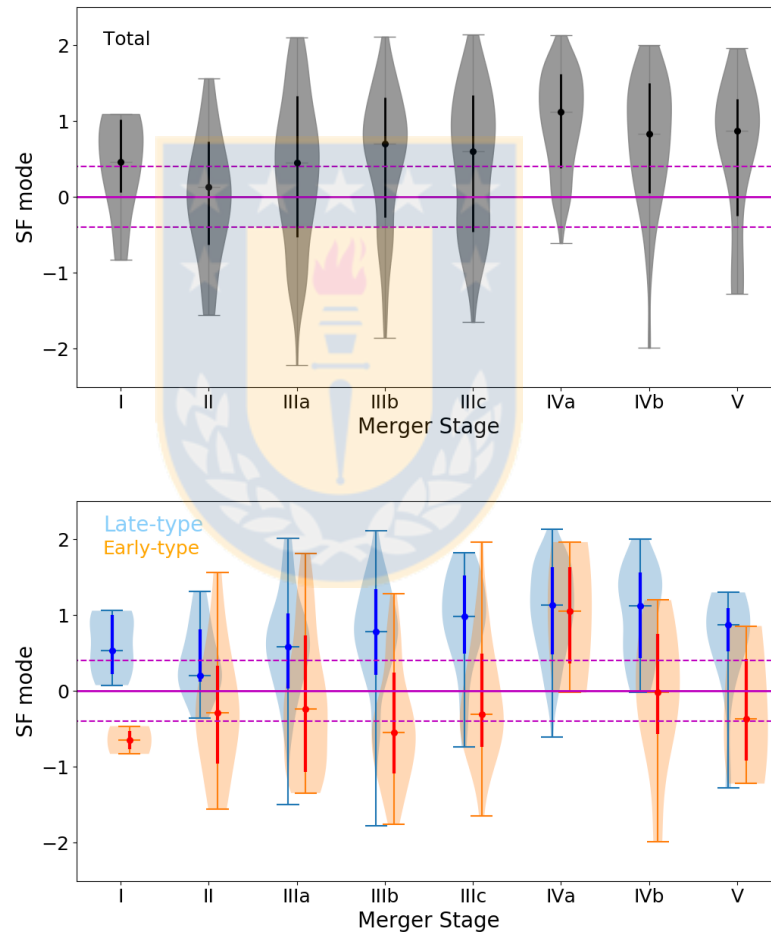


Figure 3.4 SF mode distribution in each merger stage. The filled circle indicates the median and the bold lines show the percentile including 34% of objects from each side of the median (equivalent to one-sigma). The horizontal solid- and dashed-magenta lines represent the MS. The top panel shows the SF mode distribution of the entire sample. The bottom panel shows the SF mode distribution of the merging galaxies separated by late-(blue) and early-(orange) type. HDs are separated into the late- and early-type categories (see text for details). *Credits: Calderón Castillo, P.*

Figure 3.4 shows the distribution of the SF mode in each merger stage, using so-called ‘violin-plots’. Violin-plots are essentially histograms of the normalised number distribution, only the bars are smoothed out to form the shaded region, and bars extend symmetrically to the left and right to give the characteristic violin-like shape. The median of the distribution is shown by the filled circle and overlaid horizontal line, found within each distribution. The dark-coloured lines show the percentiles including 34% of the objects from each side of the median (equivalent to one-sigma of a Gaussian distribution, but additionally allowing for asymmetry in the distribution about the median). The MS, as described previously, is shown by the solid- and dashed-magenta lines. The top panel shows the SF mode distribution of the entire sample. The first thing to notice is that almost all the mergers show enhanced SF mode. Almost every merger stage has a median that is above the positive  $1\text{-}\sigma$  line of the MS. Furthermore, the merging galaxies show an increase in SF as the merger evolves, peaking at about merger stage IVa. More generally, mergers show higher SF mode at intermediate and late stages (from IIIb to V) compared to early stages (I to IIIa).

Galaxies that are actually at early stages of the merging process might fall from large separation to small separation, and they increase their separation again after passing pericentre. Thus, our early and intermediate merger stages (I to IIIc) likely contain a mix of different projected distances between the merging galaxies. Meanwhile post-merger galaxies (e.g. as defined in Ellison et al. 2013) could be found in any of our late merger stages (IVa to V). Ellison et al. (2013) find that the SFR peaks at post-merger stages, and we indeed see a steady SF enhancement.

The bottom panel shows the SF mode distribution for late-(blue) and early-(orange) type galaxies separately. Following our morphological classification, spirals are considered late-type galaxies, and lenticulars and ellipticals are considered early-types. As explained in Sec. 3.2.1, HD galaxies have been sub-classified as late- and early-type galaxies. These galaxies have been included in the blue and orange distributions, respectively. It is clear that late-type galaxies show higher (+1.0 dex on average) SF mode compared to early-type galaxies. In fact, we find this result is independent of stellar mass (see Fig. G.1). This suggests that the SF mode principally depends on the gas content of the merging galaxy.

Figure 3.5 shows the SF mode distribution separated by morphology, as shown in the title of each sub-panel. Spiral and HD (i.e. late-type) merging galaxies show high SF. The median of each merger stage is above the MS. In fact it is the HD galaxies which show the highest SF mode values, with median SF modes of +1 (ten times higher SFR than the MS at that mass) and many being enhanced by as much as a factor of 100 in SFR. As shown in the HD panel, both late-(light green) and early-(dark green) type mergers show SF enhancement, suggesting that mergers which have suffered such strong disturbances enhance their SF either by consuming their own gas reservoir or possibly using gas acquired from their companion. On the other hand, elliptical and lenticular

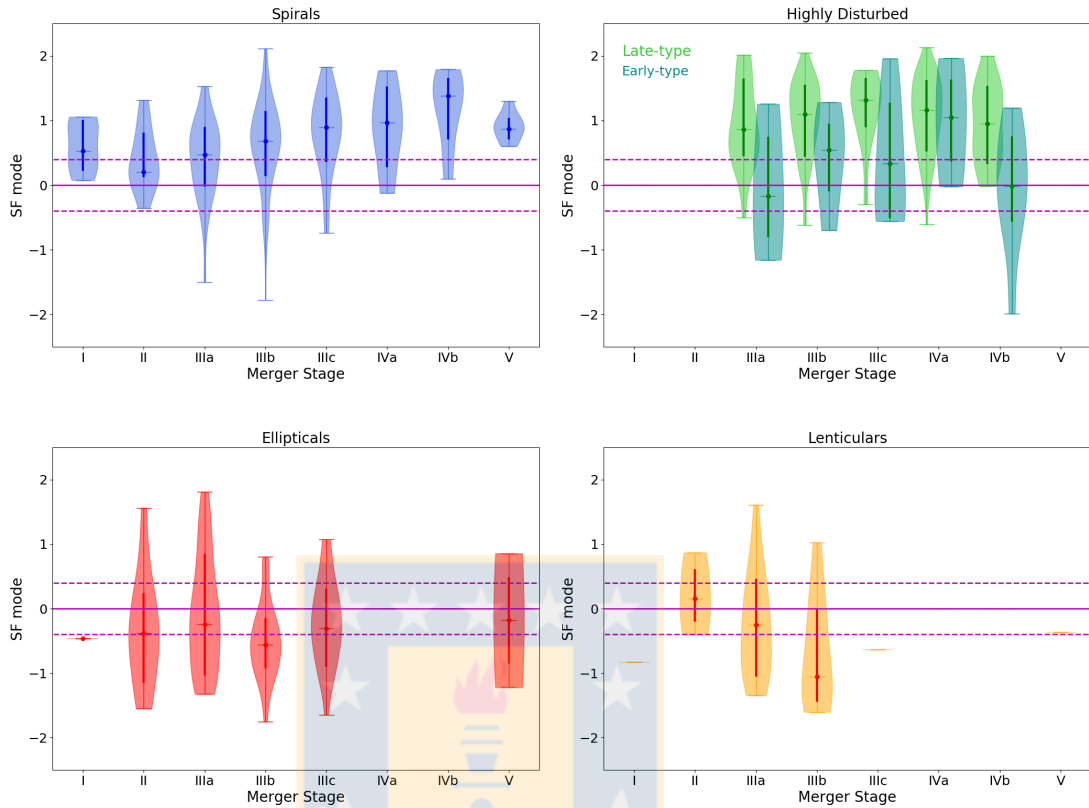


Figure 3.5 SF mode distribution in each merger stage separated by morphology. From top to bottom: Spiral, HD (late- and early-type), elliptical, and lenticular galaxies. The solid- and dashed-magenta lines represent the MS. *Credits: Calderón Castillo, P.*

galaxies show lower SF mode compared to spiral and HD galaxies, but still show higher values compared to unperturbed galaxies with the same morphology (most of which are found below the MS). This suggests that this type of galaxy could form new stars from their own small (<5%; Catinella et al. 2018) gas reservoirs or possibly collect enough cold gas from their companion to form new stars.

A key feature of Figure 3.4 and 3.5 is that enhanced SFR are seen over multiple merger stages, from stage IIIa through to stage V. This might be considered somewhat at odds with the evolving SFR seen in merger simulations, which often show short peaks of enhanced SF at critical moments such as first passage, second passage or final coalescence (Mihos & Hernquist, 1994b; Di Matteo et al., 2005; Park et al., 2017). As a result of the long duration of the SF enhancement that we observe, it raises the possibility that the enhanced SF could contribute significantly to the overall stellar mass growth of the galaxies involved. To get some feeling for the significance of this effect, we employ a back-of-the-envelope calculation. First, we consider two typical MS galaxies; a low-

mass ( $M_* = 10^9 M_\odot$ ) and a high-mass ( $M_* = 10^{11} M_\odot$ ) galaxy. We then consider how much they would increase their own stellar mass over the time period from first passage until final coalescence (roughly corresponding to the merger stage IIIa through to merger stage V). We consider two cases; if they (a) remain on the MS and continue star-forming at the same rate, and (b) suffers a SF enhancement of 1 dex above the MS (starburst) over the whole time period. Actually, the time period between first passage and final coalescence is, in part, a function of mass ratio with more major mergers tending to merge more quickly. We took the duration of the time period from the simulations of Park et al. (2017) for a 1:6 (minor) merger and a 1:1 (major) merger with a parabolic orbit, and found values of 2.3 and 1.1 Gyr, respectively.

The results of the back-of-the-envelope can be summarised as follows: The low-mass MS galaxy increases its stellar mass by 23% (11%) for the 1:6 (1:1) merger. In comparison, the low-mass starburst galaxy increases its stellar mass by 230% (110%) for the 1:6 (1:1) merger. Meanwhile, the high-mass MS galaxy increases its stellar mass by 1.3% (0.6%) for the 1:6 (1:1) merger, while the high-mass starburst galaxy increases its stellar mass by 13% (6%) for the 1:6 (1:1) merger.

In summary, and noting that we have neglected the limitations driven by the available gas reservoir, for low-mass galaxies, the starburst can be very significant to the overall stellar mass growth, and can more than double their mass. We note that our choice of a 1 dex enhancement in SFR is not even very extreme, with some galaxies showing as much as 2 dex enhancement. However, for higher mass galaxies, the enhancement in stellar mass is much less significant for the overall growth. This is a natural consequence of the fact that high-mass MS galaxies tend to have low sSFR, meaning their current SF is not as significant for their stellar mass growth than in low-mass MS galaxies.

### 3.3.3 SF mode dependence on the companion's morphology

In order to study how the different morphologies affect the SF mode of the merger before coalescence, we first selected a subsample of systems that show both merger components separately. Thus, the following analysis is based on systems at merger stages I to IIIb. Because of the low number of mergers at early stages, we study these four merger stages combined. Figure 3.6 shows the comparison between the SF mode of the primary ( $x$ -axis) and secondary ( $y$ -axis) component of the merger in the main panel. The solid- and dashed-magenta lines show the MS location for each axis and the black line shows the one-to-one relation, i.e. where the SF mode of the primary is equal to the SF mode of the secondary component. Coloured symbols show the morphology (see legend) of each component, where unfilled-large symbols show the morphology of the primary and filled-small symbols show the morphology of the secondary component. For example, a

merger that has an elliptical as a primary component and a HD galaxy as a secondary component will be shown as a big red circle with a green hexagon inside (see some examples of this case in the top-left corner of the main panel). Distributions of the SF mode coloured by morphology are shown at the top for the primary component and at the right for the secondary component.

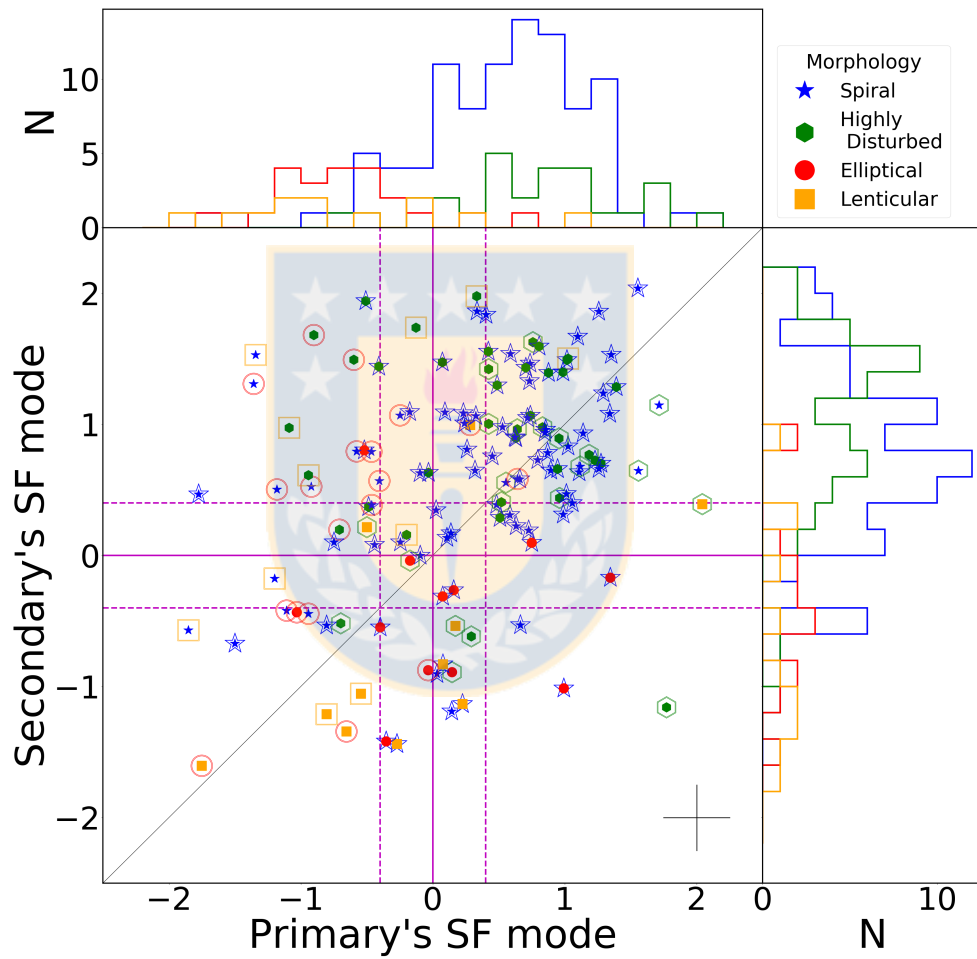


Figure 3.6 Primary's SF mode compared to Secondary's SF mode. Comparison between the SF mode of the primary and the secondary component. The coloured symbols show the morphology of the primary (unfilled symbols) and secondary (filled symbols) components as shown in the legend. The solid- and dashed-magenta lines show the MS and the black line shows the one-to-one relation. The SF mode distributions of the primary and secondary component are shown in the top and right panel, respectively. The SF mode distributions are coloured by morphology as shown in the legend. *Credits: Calderón Castillo, P.*

As noted previously, the spirals and HD galaxies show higher SF modes compared to elliptical and lenticular galaxies. Thus, as a rule of thumb, the SF mode of a merging galaxy seems to be primarily dictated by the galaxy's morphology. For example, primary spirals (large blue stars) typically appear on the right-hand side of the diagram, similarly for HD galaxies. Similarly, primary elliptical and lenticular galaxies (large red and orange symbols) are mostly found towards the left of the panel. The same is true for secondaries, e.g. secondary spirals (small filled-blue stars) are found towards the top, while secondary lenticulars (small filled-orange squares) generally are found towards the bottom of the diagram.

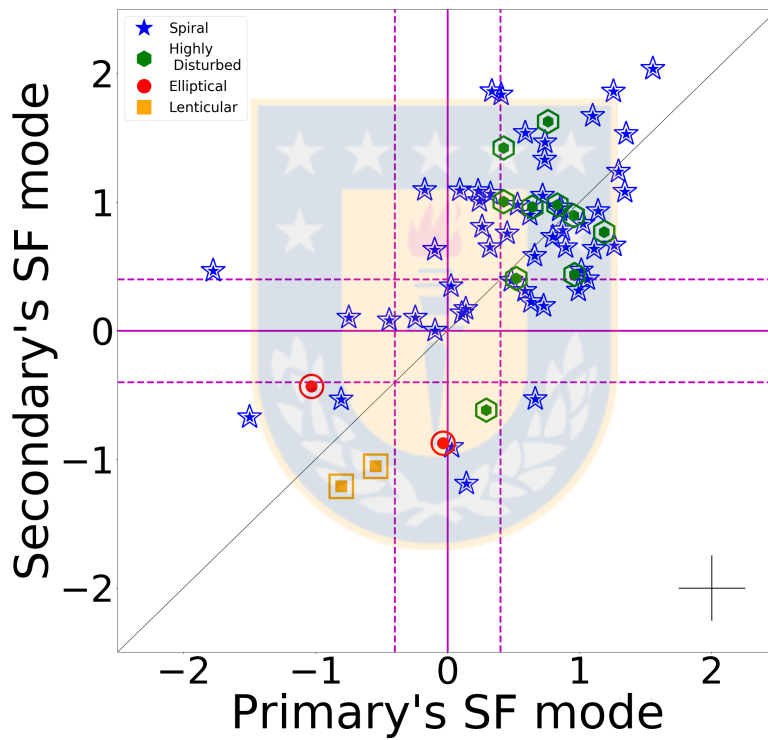


Figure 3.7 Primary's SF mode compared to Secondary's SF mode when Primary and Secondary have the same morphology. Comparison between the SF mode of the primary and the secondary component, for mergers with components of the same morphology. The coloured symbols show the morphology of the primary (unfilled symbols) and the secondary (filled symbols) components as shown in the legend. The solid- and dashed-magenta lines represent the MS and the black line shows the one-to-one relation. The typical error is shown in the bottom-right corner. *Credits: Calderón Castillo, P.*

Simplifying the previous plot, we now consider only systems where both components share the same morphology, so both the small filled symbol (the secondary) and large surrounding symbol

(the primary) will match, as shown in Fig. 3.7. It can now be seen that the distribution of points is not symmetrical about the one-to-one line as would be expected if both primary and secondary responded equally to the tidal interactions. Instead, an overpopulation of points can be seen above the one-to-one line compared to the population below (56% compared to 44%, respectively). This shows that the SF mode of the secondary component tends to be more enhanced than the primary component. We also tested this in both major and minor mergers separately, and found the same trend in both cases (see figures in App. H.1). We have so far only considered SF mode calculated with respect to the MS derived in CHANG+15. In fact, this is a sensible choice as the CHANG+15 study also uses the same SED fitting tool, and so is a fairer comparison. However, we were curious to see how sensitive these results are to our choice of MS. Therefore, we also reproduced Figures 3-7 using the MS derived in Elbaz et al. (2007). Overall, we find the results show the same main features, and the same general distribution. One minor difference is that the spiral galaxies show a hint of being slightly closer to the MS with the Elbaz MS, although they are still clearly enhanced, but for other galaxy morphologies the results are very similar. Therefore, in general, we find our main conclusions are not strongly dependent on our choice of CHANG+15 MS over the Elbaz MS.

Spiral-spiral and HD-HD mergers typically show enhancement of their SF mode. We will consider if having matched morphologies impacts the amount of SF enhancement later in this section.

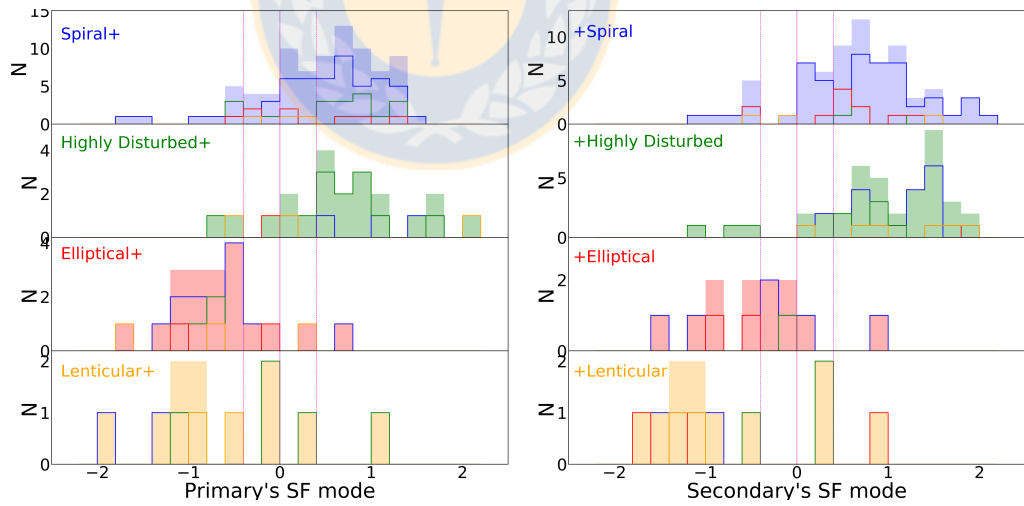


Figure 3.8 SF mode by Component and morphology. SF mode of the primary (left panel) and secondary (right panel) component separated by their morphology. The filled distributions show the total distribution of the morphology shown by the text in each panel. The unfilled distributions show the distribution of the companion's morphology. *Credits: Calderón Castillo, P.*

We now attempt to understand if the morphology of the companion has any impact on the SF



properties of a merging galaxy. To do this we start with the histogram shown at the top of Fig. 3.6, but now separate each of the histograms (separated by primary morphology) shown into a different sub-panel, as shown in the left column of Figure 3.8. The total sample in each sub-panel is given by a shaded histogram. We then colour the histogram lines based on the morphology of the companion. For example, to see how a primary spiral (top panel) responds to having a secondary elliptical (red lines), we can see where the red bars fall on the x-axis (the primary's SF mode). We now repeat this process in the right column of Figure 3.8 but adjusted so that we can instead see the effect of the primary's morphology (histogram bar colour) on the secondary galaxy's SF mode (x-axis). The labeling of the sub-panels uses the following system: 'Primary morphology' + 'Secondary morphology'. e.g. the sub-panel labeled as 'Spiral+' shows the mergers that have a spiral galaxy as primary, and '+Elliptical' shows galaxy's with a secondary elliptical. The colour of the labels in each subpanel matches the colour of the histograms.

As mentioned before, spiral and HD galaxies continue to show clear SF enhancements, with HD galaxies showing slightly higher SF modes. One exception is when the HD galaxy is a primary and has an elliptical as secondary. In this case, both galaxies seem to approach the MS from both sides, with HD galaxies showing decreasing SF mode and ellipticals showing increased SF mode. For example, the 'HD+' panel shows red bars on the left (i.e. HD suppression), while the same system can be seen in the '+Elliptical' panel as green bars on the right (i.e. elliptical enhancement), although clearly this result has the caveat of small number statistics.

In order to analyse any dependence on the stellar mass ratio between the components, we separated the panels in Fig. 3.8 into major and minor mergers. These are shown in the top (major mergers) and bottom (minor mergers) panels of Fig. 3.9.

Comparing major and minor mergers, spiral and HD galaxies (filled-blue and -green distributions) as primary or secondary galaxies show similar trends independent of stellar mass ratio. On the other hand, even considering the low number statistics, it appears that most of the early-type galaxies (filled-red and -orange distributions) show higher SF enhancement if they are in a minor merger compared to major mergers, with the single exception of primary ellipticals, which show the same trend for both major and minor mergers.

Now considering primary spirals, we observe that the median SF mode of the primary is higher when the secondary is a HD (+0.9 dex) than if the secondary is any other type of galaxy (median SF mode of 0.5 dex). A similar scenario is observed for primary lenticulars, where higher SF modes are shown when this type of galaxy interacts with HD galaxies in minor mergers, compared to when interacting with spirals in major mergers. This could suggest that in minor mergers, the primary lenticular galaxy more strongly disturbs the secondary component, transforming it into a HD, and perhaps causing the transfer of some of the cold gas from the secondary to the primary

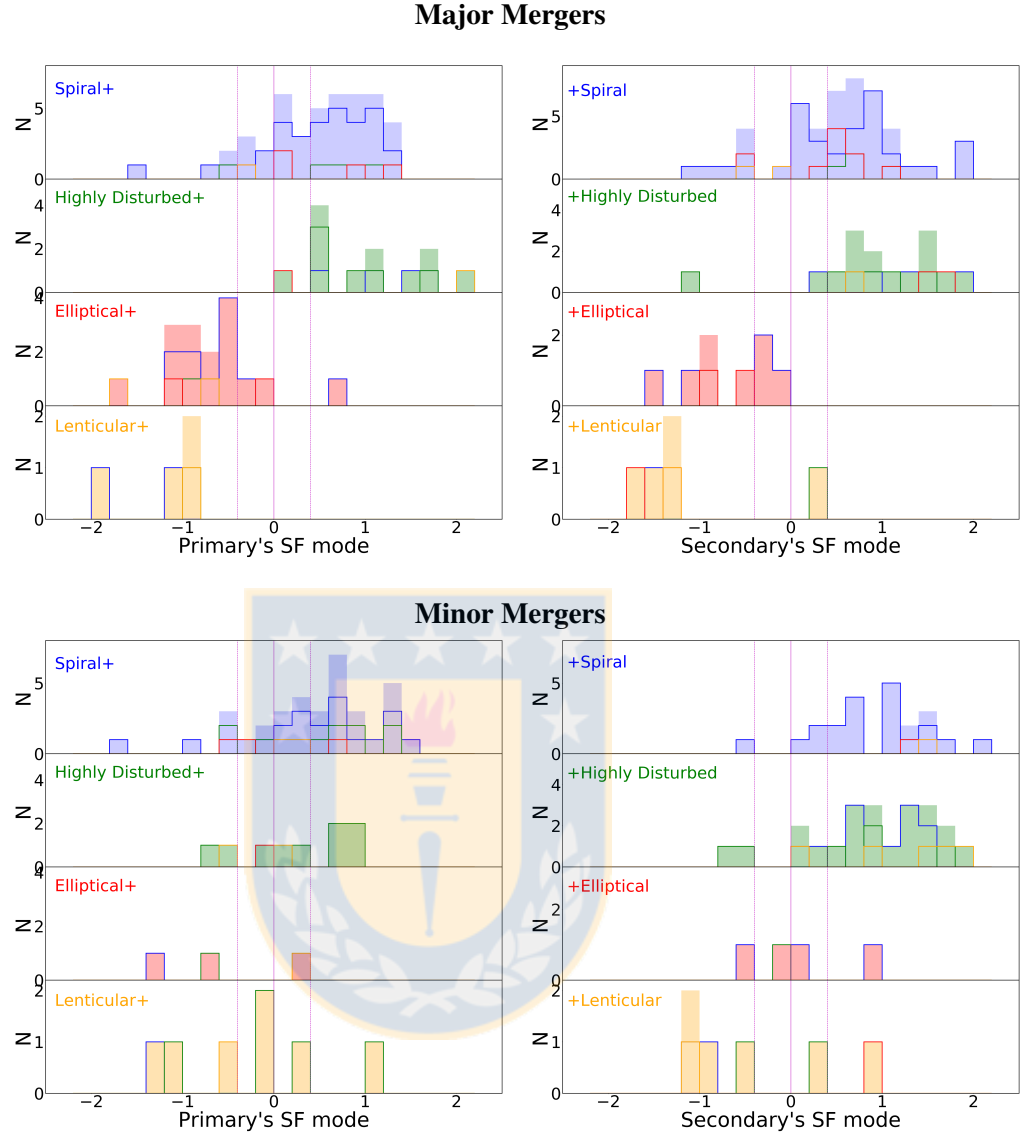


Figure 3.9 SF mode by Component and morphology for Major and Minor mergers. As in Fig. 3.8. The left panels show the SF mode of the primary and the right panels show the SF mode of the secondary component, separated by major (top panels) and minor (bottom panels) mergers. *Credits: Calderón Castillo, P.*

lenticular, resulting in bursts of SF. However, this is not seen in major mergers, where the spiral galaxy is less strongly affected by the lenticular because of their more similar stellar mass. Without highly disturbing the spiral, there may be less opportunity for a significant transfer of cold gas to the lenticular galaxy, hence no rise in SFR. These dependencies on the morphology of the companion agree with Hwang et al. (2011)'s work, where they show that LIRGs have a dependency on the morphology (late- and early-type) of their companions.

For secondary components, these galaxies do not show a clear dependency on stellar mass ratio, as both of the right panels of Fig. 3.9 show similar distributions. Also, these galaxies do not seem to be affected by the morphology of the primary, in contrast to the results mentioned above.

We have also separated the sample in different stellar mass bins to study any dependence on stellar mass. This separation did not show any clear SF mode dependency on the stellar mass of the merger. The SF mode comparisons separated by stellar mass bin are shown in Fig. G.2.

### 3.3.4 Evolution during the Merger Process: SMBH activation

To identify the AGNs in our merger sample, we have used three different methods. The first one is based on the emission line diagnostic diagrams (hereafter BPTs, Baldwin et al. 1981), which uses the ratio between forbidden emission lines to identify galaxies with either star formation activity, active nuclei features, or galaxies with both type signatures (composite galaxies). The BPT that compares  $[\text{OIII}]/\text{H}\beta$  and  $[\text{NII}]/\text{H}\alpha$  will be referred to as BPT-NII. The second and third BPT diagram compare  $[\text{OIII}]/\text{H}\beta$  and  $[\text{SII}]/\text{H}\alpha$  and  $[\text{OIII}]/\text{H}\beta$  and  $[\text{OI}]/\text{H}\alpha$ , respectively, separating Seyfert galaxies from star-forming and LINER galaxies. These BPT will be referred to as BPT-SII and BPT-OI, respectively.

The second method we use is based on a different emission line, HeII, which is observed only if there is a source with hard ionization radiation. This allows us to detect fainter AGNs and/or AGNs embedded in a galaxy with strong SF. This method compares  $\text{HeII}/\text{H}\beta$  and  $[\text{NII}]/\text{H}\alpha$  as shown by Shirazi & Brinchmann (2012, hereafter SB12). We will refer to this method as HeII diagram.

For these first two methods, we have matched our sample to the OSSY (Oh et al., 2011) catalogue. This catalogue has improved the emission line measurements from SDSS DR7, see details in Oh et al. (2011). Sixty percent of the sample show emission lines. This sub-sample show a merger stage and a  $M_*$  distribution similar to the parent sample.

The third method we use is based on the NIR WISE colours, which compares W1-W2 and W2-W3. This colour-colour diagram (hereafter WISE diagram) can identify an AGN in a galaxy as shown by Jarrett et al. (2011, hereafter J11) and Stern et al. (2012, hereafter S12).

Figure 3.10 shows the different methods coloured by morphology. The three top panels show the different BPTs, BPT-NII at the left and BPT-SII in the middle. Each panel shows the separations found in the literature, summarised by Kewley et al. (2006). The bottom-left panel shows the HeII diagram. The separation lines are as shown by SB12. The bottom-right panel shows the WISE diagram, and the lines separating AGN, (U)LIRGs, spheroids and intermediate and star-forming disks, as shown by J11 and S12.

When analysing the diagrams coloured by morphology (Fig. 3.10), we observe that early-type

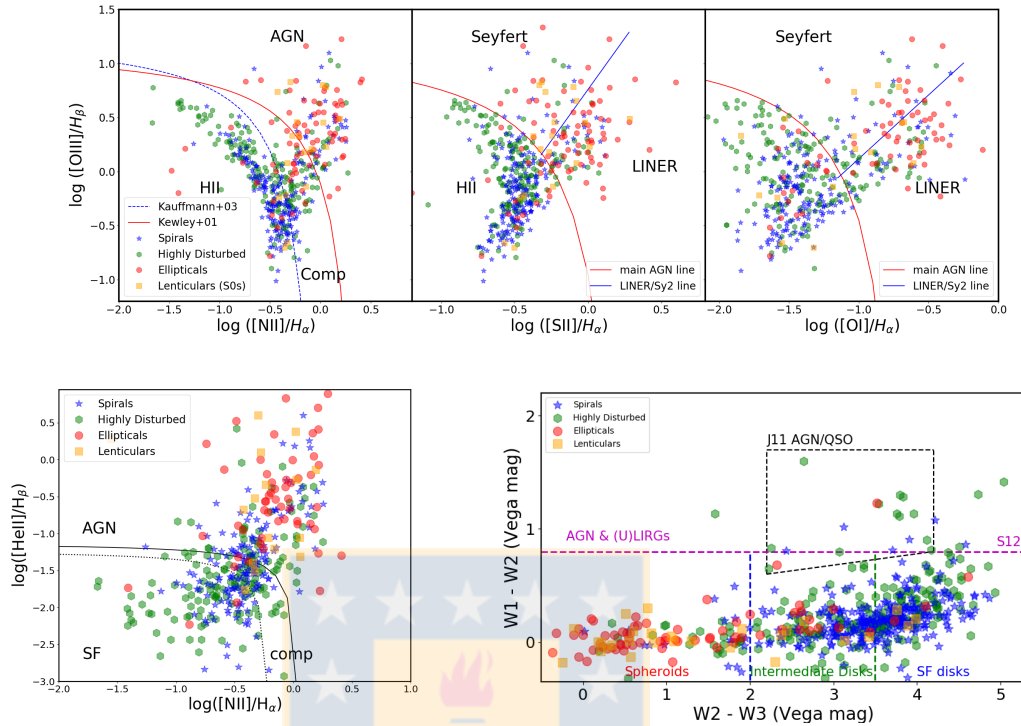


Figure 3.10 Methods to identify AGN. *Top*: BPT diagnostic diagrams of the sub-sample that shows emission lines. Separations are shown in the legends. *Bottom – left*: Diagnostic diagram based on the HeII emission line. Separations defined by SB12. *Bottom–right*: WISE colour-colour diagram. Separations defined by J11 and S12. Mergers in the different panels are coloured by their morphology as shown in the legend. *Credits: Calderón Castillo, P.*

mergers are likely to be in the AGN region and the SF region is mainly populated by spirals, as expected. The WISE diagram shows mostly HD galaxies in the AGN & (U)LIRG region, this is expected as (U)LIRGs are generally very perturbed objects.

Figure 3.11 shows the percentage of galaxies with an AGN in each merger stage, identified by any of the methods shown previously. Galaxies considered AGNs only are coloured in red. Galaxies within the regions: AGN, composite, Seyfert, and LINER are shown by magenta symbols. Errors of the percentages were calculated following Sartori et al. (2015)’s work, using binomial statistics for number of objects ( $N_{tot}$ ) in each stage higher than 20, and for  $N_{tot} \leq 20$  following the confidence limits shown by Gehrels (1986).

AGN seem to start being triggered at intermediate merger stages (since IIIa), where galaxies are close together and clearly after their first passage. AGN peak at stage IVa at the coalescence period and start to slowly decrease at late stages (since IVb).

The peak on the AGN fraction towards coalescence stages agrees with (Park et al., 2017) work.

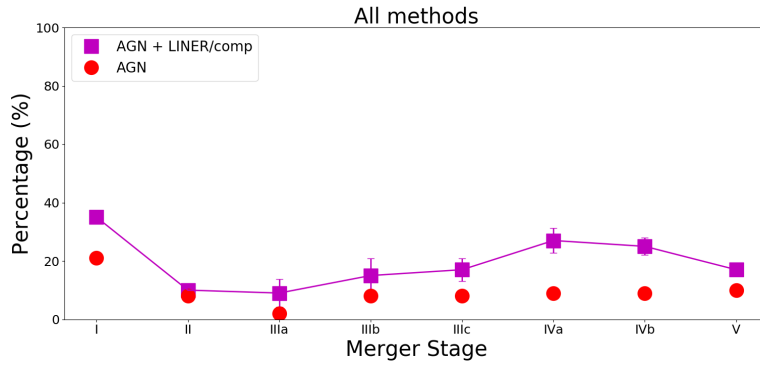


Figure 3.11 AGN fraction at each merger stage. Percentage of galaxies contain an AGN identified by either BPTI, BPTII, HeII emission line or WISE diagram in each merger stage. *Credits: Calderón Castillo, P.*

They show that the accretion rate of gas into the central black hole peaks just before coalescence for pairs with stellar mass ratios of 1:1. However, this declines for merging systems with stellar mass ratios higher than 1:3. This is similar to (Di Matteo et al., 2005)'s simulations, showing that the AGN accretion rates tend to peak at coalescence and rise from early stages depending on the virial velocity of the merging galaxies. On the other hand, observations show that the AGN fractions are higher when the distance between the galaxies is smaller, and peak for post-mergers (Ellison et al., 2013; Satyapal et al., 2014; Hwang et al., 2010). This contradicts our findings, but we need to consider the difference in signal between the studies. Our dependency on merger stage is much higher than their dependency on projected separation, but our sample is also smaller compared to theirs. Furthermore, via our selection criteria, we only consider isolated merging systems.

It is also important to consider some of the caveats of using emission line diagnostics to identify AGN. In particular, dust obscuration can effectively reduce the spectral lines used to indicate AGN. Hence, in principle, it might become more difficult to identify AGN at late merger stages, when the gas and dust may become more centrally concentrated. Also, a common source of data for AGN identification is the spectra of the SDSS, in which the spectral fiber is 3'' in diameter. Therefore, the spectra will tend to include more light from the galaxy as a galaxy's distance increases. This latter issue was addressed in Hwang et al. (2010) by restricting their IRGs sample to galaxies with redshifts  $z < 0.04$ . We attempt to address these issues by checking for any dependency on redshift and dust fraction of our sample. We do not observe any clear dependency on these properties, and therefore do not consider these sources to strongly bias our data. Also, by following our approach, we are able to more fairly compare our results with other measurements of

AGN fraction in the literature who follow the same approach (Ellison et al., 2011, 2013; Satyapal et al., 2014). Although to better address this issue, we believe that identifying AGN using X-ray emission (which is not affected by dust emission) could be of great benefit, and we will consider this topic in a future publication.

We also analyse the number of AGNs identified by the different methods separately (Fig. 3.12) and show where the AGNs identified by one method are located in another method's diagram (App. I.1). Figure 3.12 shows the percentages, of AGNs identified using, from top to bottom, the BPT-NII, BPT-SII, BPT-OI, HeII diagram, and the WISE diagram. First, we notice that the peak at late merger stages is observed in all BPT diagrams as well as WISE-classified AGN. This is not the same for AGN classified using the HeII diagram. We also observed that composite and LINER fraction are very similar to the AGN percentage. Thus, the increase on this type of galaxies do not increase importantly when studying them using this methods. Except when using the BPT-NII, where the fraction of composite and LINER galaxies increase the final fraction by almost twice its value. This increase occurs at intermediate-late and late stages (since merger stage IIIb).

As we observe the low fractions of AGN identified by WISE colours, we can assume that the AGN in this type of galaxy might not outshine the total galaxy light. Hence, most of these AGN are not very powerful.

We have also cross-matched our sample to the VCV (Véron-Cetty & Véron, 2010) catalogue. This catalogue compiles information of AGN confirmed using different methods. When matching the merger sample to the VCV catalogue, we obtain 85 galaxies hosting an AGN. Fifty two of these merging galaxies show emission lines available in OSSY tables. Figure 3.13 shows the VCV-classified AGNs in the three original BPTs. We observe that about a third of these galaxies are classified as star-forming using the BPT method. Figure 3.14 shows that less than a third of the objects are classified as star-forming using the HeII line.

From the objects missing emission lines and not classified as AGN by using either the BPT or HeII, these are mainly at late stages (IVb and V) of the merger sequence, from which 4 are already classified using WISE colours. Percentages at each stage of these objects are as follows: 7% at Merger Stage I, 3.6% at Merger Stage II, 2.5% at Merger Stage IIIa, 3% at Merger Stage IIIb, 1.4% at Merger Stage IIIc, 6% at Merger Stage IVa, 22% at Merger Stage IVb, 21% at Merger Stage V.

Figure 3.15 shows the percentages of merging galaxies hosting an AGN at each merger stage, these AGN have been classified using all four methods: BPTs, HeII, WISE colours, as shown in Figure 3.11, and the VCV catalogue in cyan. This emphasizes the rise in the fraction of merging galaxies hosting an AGN at late stages (Iva to V), suggesting that AGN are mainly triggered at final coalescence. Also, the high fractions at these stages is the result of also adding composite

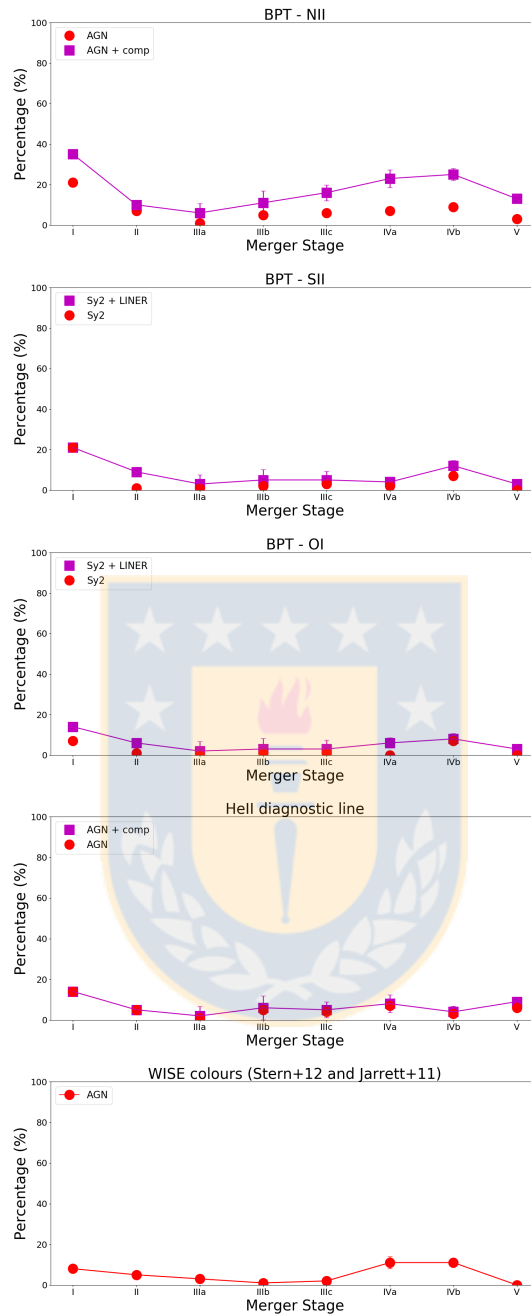


Figure 3.12 AGN fraction at each merger stage from each method. Fraction of galaxies containing an AGN in each merger stage. The panels show, from top to bottom, the AGNs identified using the BPT-NII, BPT-SII, BPT-OI, HeII emission line, and WISE diagram. Credits: Calderón Castillo, P.

galaxies and VCV-classified galaxies, suggesting that these objects beside hosting an AGN are still forming stars as well.

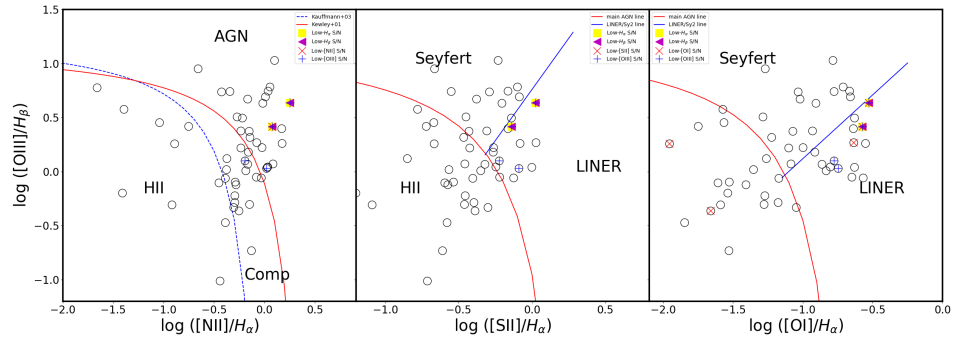


Figure 3.13 BPTs of the merging galaxies hosting an AGN included in the VCV catalogue. Yellow squares show low ( $S/N < 3$ ) S/N for  $H_{\alpha}$ , magenta triangles show low S/N for  $H_{\beta}$ , Red "x"s show low S/N for [NII], [SII], or [OI], in the respective BPT, and blue "+"s show low S/N for [OIII]. Credits: Calderón Castillo, P.

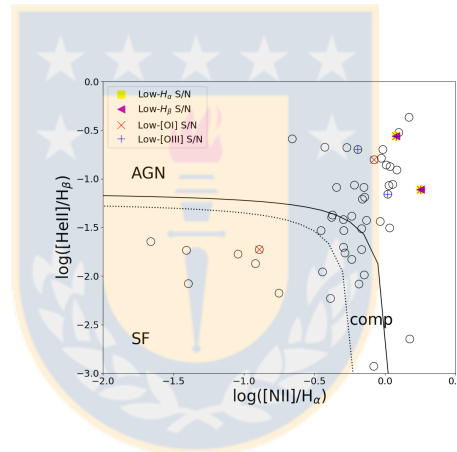


Figure 3.14 HeII line diagnostics of the merging galaxies hosting an AGN included in the VCV catalogue. Yellow squares show low ( $S/N < 3$ ) S/N for  $H_{\alpha}$ , magenta triangles show low S/N for  $H_{\beta}$ , Red "x"s show low S/N for [NII], [SII], or [OI], in the respective BPT, and blue "+"s show low S/N for [OIII]. Credits: Calderón Castillo, P.

Figure 3.16 shows the merging galaxies hosting an AGN in the SFR- $M_*$  plane. They are mainly located at high SFR and high  $M_*$ , but not exclusively. We observe a dependency on  $L_{[OIII]}$  to both SFR and  $M_*$ . This is expected for  $M_*$ , as more massive galaxies host more massive AGN. Galaxies hosting an AGN showing high SFR might suggest positive feedback from the AGN. This means that the AGN allows the galaxy to form stars more rapidly. However, as shown previously, these AGN are not very powerful, suggesting that the AGN is not importantly affecting the star formation within the galaxy.



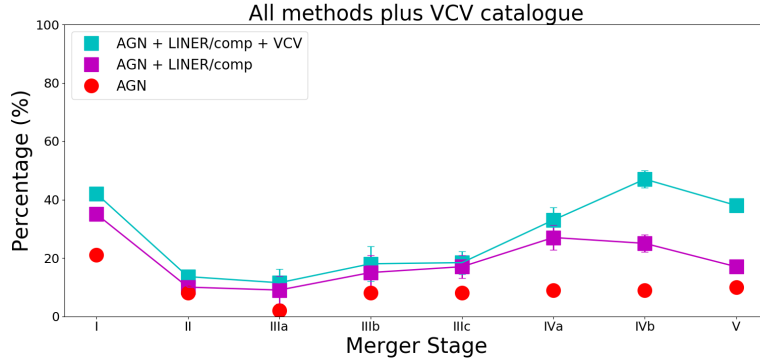


Figure 3.15 Percentages of merging galaxies hosting an AGN at different merger stages. Red circles are AGNs classified using either the BPT, HeII or WISE colours. Magenta squares are objects classified as either AGN, composite, or LINER using any of the methods mentioned previously. Cyan squares are AGNs classified by the VCV catalogue. *Credits: Calderón Castillo, P.*

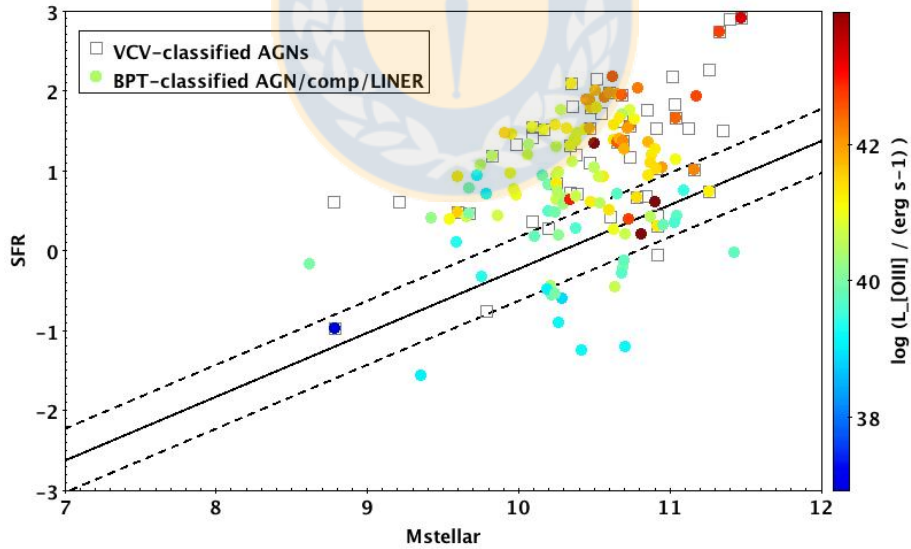


Figure 3.16 AGNs in the SFR- $M_*$  plane. Circles show AGNs classified by either using the BPT, HeII or WISE colours. These are coloured by their  $L_{[OIII]}$ . Squares show the AGNs classified by the VCV catalogue, not all of these objects show emission line measurements in the OSSY table. *Credits: Calderón Castillo, P.*

# 4

## Discussion and Conclusions

We have assembled a sample of 540 mergers in isolated environments. The galaxies forming part of the merger have been constrained to have similar redshift, which ensures we are including only galaxies that could merge (i.e. we exclude clear cases of fly-bys). The mergers have been classified by morphology and also we have classified the mergers according to their current phase in the merging process.

### 4.1 Multi-band Photometry

We have performed photometry in a semi-automated manner in order to extract the flux of the entire galaxy. We find this is necessary as the automated photometry from publicly available catalogues proves unreliable for this type of galaxy. Our semi-automated photometry has been performed in 11 bands, including ultraviolet (FUV and NUV from GALEX), optical ( $u$ ,  $g$ ,  $r$ ,  $i$  and  $z$  from SDSS), and near infrared (W1, W2, W3 and W4 from WISE).

We find that most of the galaxies show higher fluxes using our semi-automated photometry compared to the GALEX, SDSS, and AllWISE catalogs. This is a result of the larger apertures that we find are required in order to capture all of the galaxy's light in comparison to the fluxes from these catalogues in the literature. This demonstrates that automated methods are not efficient in extracting all of the light in merging galaxies, often missing the light in the outskirts where tidal features may be found, and breaking up the galaxy into individual objects instead of recognising they are from the same galaxy (e.g. star-forming regions). Also we find that radial corrections, performed by Chang et al. (2015, hereafter CHANG15), which are designed to correct for aperture effects, seem to result in over-estimating the flux for W1-3. This shows that corrections of this type may have poor accuracy in merging galaxies. These combined results have convinced us to pursue a less-automated approach to perform the photometry in order to make sure that we are measuring the light of the entire galaxy in all the filters mentioned above.

The differences in photometry results show no clear dependency on either morphology or merger stage. The only dependency is on the aperture size used when extracting the light from each source. Thus, an accurate aperture must be chosen for merging galaxies, in order to extract the entire light of the galaxy, including tidal tails and star-forming regions.

## 4.2 Stellar Masses and Star Formation Rates Estimates

Comparing the results for  $M_*$  and SFR using the same method (MAGPHYS) but varying the number of filters used as an input (GALEX+SDSS+WISE versus SDSS+WISE), the one-to-one relations are tight for most of the sample but it also can lead to differences of a factor of 10 for  $M_*$  and 15 for SFR for individual galaxies. This indicates that UV is clearly important to the SFR estimation as might be expected, but also it is significant for  $M_*$  estimations. When we compare our measured fluxes to CHANG15 fluxes, we find that our measurements are higher than theirs except for W1-3. This might be because of the aperture correction tend to over-correct the fluxes on these filters. This can cause MAGPHYS to fit an altered SED resulting in our measurements having lower  $M_*$  and higher SFR.

A similar outcome is shown when we compare the results from MPA-JHU tables to our  $M_*$  and SFR measurements. The difference in the results are likely linked to the photometry since they use optical colours to estimate the  $M_*$  and correct based on optical images to estimate the total SFR. These differences arise because their approach is designed for non-perturbed galaxies.

The comparison between our  $M_*$  estimates to NSA listed  $M_*$  proves tight for most of the sample, with a tendency for our estimates to be larger than theirs at the high- $M_*$  end.

We note that the scatter in  $M_*$  and SFR is smaller than the scatter seen when comparing fluxes. This suggests that the SED fitting is smoothing out some of the scatter seen in the fluxes, which could be partially related to the resolution of some of the filters that contribute the most to  $M_*$  and SFR estimations. However, it is important to note that even when the scatter appears to be small, the difference in photometry for some of the galaxies can lead to differences in  $M_*$  of a factor of 1000 and a factor of 10000 for SFR. This suggests that the previous values in the literature should be used with caution, and that an adequate photometry must be conducted for these types of galaxies before estimating  $M_*$  and SFR.

There is also no clear dependency on morphology or merger stage in the  $M_*$  and SFR estimates, which leads us to conclude that the major factor affecting our results is the photometry performed.

The  $M_*$  and SFR indicators based on optical colours seem to perform well for mergers in general, but mergers show a large scatter to these relations. Our results show lower  $\log(M_*/L_r)$  for the same colours compared to B03's relations. On the other hand, our  $M_*$  show a closer correlation

to T11's  $M_*$  indicator, which is also based in SED fitting of photometric data spanning from the UV to the far-infrared but using different photometry.

It is important to remark that these catalogs and indicators have been optimized for statistical studies. Thus, it is not surprising that they show issues for mergers' estimations.

### 4.3 WISE colours and sSFR

The WISE colour-colour diagram separates the morphologies of our sample as it is designed to do. However, we can see different morphologies in the various regions of the colour-colour diagram, suggesting that these galaxies go through colour changes when they are involved in a merging process, as previous studies found.

Overall, mergers appear to inhabit the same regions of the SFR- $M_*$  plane as unperturbed galaxies and a large fraction of our sample is located in the starburst region. How these mergers move on this plane as they pass through the merging process will be the focus of Chapter 3.

Finally, the estimation of sSFR from W1-W4 colours is only recommended for lenticular galaxies, as other morphologies show larger scatter. Instead, sSFR should be estimated using  $M_*$  from W1 (CL14) and SFR from W4 (CL14).

### 4.4 SF mode and SMBH activation during the Merger Process

Several simulations and observations have shown that mergers can raise their star formation rates (SFR) by 10-100 times the SFR of unperturbed galaxies at the same stellar mass ( $M_*$ ). We decided to study this enhancement using a more timeline-like approach, to try to better capture the chronological order of the merging process. For this, we used the  $M_*$ , SFR, and merger stages from the new catalogue of isolated merging systems. The  $M_*$  and SFR from this catalogue were estimated applying the SED fitting code MAGPHYS to the photometric data presented in Chapter 2. As we mentioned previously, the semi-automated photometry used in this work allows us to extract the entire light of merging galaxies, including faint tidal tails and bright star-forming regions, which were excluded by catalogues applying automated photometry. We then compared the SFR/ $M_*$  values of our galaxies to galaxies on the star-forming main sequence (MS) determined by CHANG+15. The distance of galaxies from the MS is described as the 'SF mode' and we use this parameter to study the SF enhancement during the merging process.

Our main results are as follows:

- Overall, merging galaxies show an SF mode according to their own morphology. For example, spiral and HD galaxies show high SF enhancement, with the highest values reached

by the HD galaxies, which show a median value of 1 dex above the MS limit. On the other hand, elliptical and lenticular galaxies show the lowest SF mode values. However, even the elliptical and lenticular galaxies show enhanced SF compared to their unperturbed counterparts. This could suggest that the merging process induces the transfer of cold gas between the merging galaxies before coalescence, or enhances SF in any gas that exists prior to the collision.

- In general, secondary merging galaxies show higher SF mode compared to their primary galaxy, whether they are involved in major or minor mergers. This suggests that the lower-mass galaxy seems to be more affected by the tidal forces during the interaction.
- In minor mergers, when a primary spiral has a HD galaxy as a secondary, the spiral's SF mode is generally higher than if the secondary is a spiral. This might suggest that, if the tidal interaction is sufficiently violent to convert a secondary spiral into a HD, the interaction is also strong enough to cause a more significant enhancement in the primary spiral itself.
- There is a weak trend increasing SF along the merger sequence, peaking at merger stage IVa. However, overall, the SF is enhanced since early merger stages throughout the merging process.
- After identifying AGNs using three different methods commonly used in the literature, we show that AGNs are more likely to be found at late stages. As the galaxies coalesce, the AGN accrete gas more rapidly, as shown by several simulations.
- AGN are found mainly at high SFR and  $M_*$  in the SFR- $M_*$  plane. This might suggest a positive feedback effect. However, the low luminosities found for our AGN suggest that these do not affect significantly the SFR of their hosting galaxy.

Our results suggest that the transfer of cold gas may possibly occur since very early stages in the merger sequence. This is observed in simulations, where a bridge of gas can temporarily link both galaxies during close passages (e.g. Weniger et al. 2009; Moster et al. 2011; Hwang & Park 2015). This bridge can transfer gas from one galaxy to the other or even, depending on the properties of the galaxies merging and the orbital parameters, the two galaxies can transfer gas to the other at the same time (Di Matteo et al., 2007). However, this bridge of gas can be compressed or even ionised depending on the presence of a hot halo in one or both of the galaxies involved in the merger (Moster et al., 2011; Hwang & Park, 2015). If this really is gas transfer, then it raises the possibility that interacting pairs could be used to constrain the hot gas halo content of galaxies. However, another possibility is that the tidal interactions may simply be inducing or enhancing

star formation in any small quantities of gas that exist within the pre-merger early-types. As deep-imaging observations of ellipticals show that some of these objects (some with merger remnant morphologies) are surrounded by gas (e.g. Young et al. 2018), suggesting that many ellipticals can still contain some gas provided from previous mergers and/or interactions with gas-rich galaxies.

In addition to the SF enhancement being observed since early merger stages, it is also interesting to note that this enhancement can be seen to last for the entire merging process. This is often not what is seen in many previous simulations of interacting galaxies, where SF peaks occur for short durations after the first or second passage and/or during the final coalescence (Park et al., 2017). This might be related to the sub-grid physics recipes used to model star formation and feedback which can act to rapidly suppress strong starbursts. It might also be related to the fact that many of these simulations were not conducted in a fully cosmological context, and thus could lack the cosmological inflow of gas necessary to sustain SF for longer periods of time. Perhaps, the new generation of cosmological simulations will have sufficient resolution to enable us to better understand the merger process, and to study the transfer of gas between interacting galaxies. Considering a starburst that lasts for a longer period could affect how we study merging galaxies and also might help to change some recipes used in future simulations.

Observations show that the fraction of interacting galaxies increases at higher redshifts. Thus, there were more merging systems in the past than what we find now. If mergers are so destructive to the prior galaxies, how do we not observe more galaxies with perturbations in the local Universe? Perhaps, merging processes help to increase the bulge growth and afterwards a disk is re-formed. Or, we are just lacking deep enough imaging to observe these perturbations, as shown by some deep observations of elliptical galaxies.

Another aspect to consider is the gas concentration when it is been funneled to the center of galaxies. Simulations predict this concentrations are very small. However, new cosmological simulations (FIRE) have found that with the new implementations in the code, these central star-forming regions are more extended than the ones shown by previous simulations. This can be tested using different wavelengths, e.g. UV and IR, measuring the size of the emission in these different wavelengths, we can estimate the sizes of the star-forming regions, and study how large the central gas concentrations are due to gas inflow.

Furthermore, as merging galaxies show such a steady and high SF enhancement since early merger stages, this raises the possibility that merger induced star formation could contribute more significantly to the growth in stellar mass of a galaxy than has previously been considered. Our very approximate calculations suggest that low-mass MS galaxies can at least double their stellar mass as a result of the SF enhancement (see Section 3.3.2). Therefore, this could place the merger process as an important factor in some galaxies' growth in the hierarchical/cosmological scenario.

# 5

## Future Work

Other interesting features to study are the **(i) stellar populations, (ii) radial metallicity, and (iii) concentration of the star formation**. Different colour diagrams allow us to study the different stellar populations of a galaxy, where we can learn from the prior stellar populations the galaxies had before the merger and the new populations formed by the merger. As the gas is funneled to the center to form stars, it also changes the radial metallicity of the galaxies. Enriching the center with metals, and leaving the outskirts more metal-poor. This can be study taking advantage of the most recent telescopes, with **integral field units (IFU)**. These instruments allow us to observe and study the spatial spectroscopy and light from a galaxy, giving us a more detailed view of the galaxy. Additionally, the size of the concentration of gas, predicted by simulations, can also be tested. Though, some current cosmological simulations (FIRE) have shown that the central star-forming regions are more extended than the sizes determined by previous simulations. **Measuring the sizes of the emission in already available UV/IR images and from future high-resolution observations**, we can also study the size of the star-forming regions. However, as shown in Chapter 2, the photometry in this type of object needs to be less-automated and to be cautious from all the problems associated to the photometry of mergers mentioned in this study.

The gas that is funneled to the center also feeds the central super-massive black hole (SMBH), activating it. This AGN can be identified using different methods, which depend on the angle that the AGN is being observed, how powerful it is, and if it is being blocked by dust within the galaxy. Thus, the three different methods we show here might be underestimating the **(iv) AGN fraction** shown at each merger stage. A more secure method to identify AGN is **observing the X-ray emission** of the galaxy. There have been a few surveys and I found that some of our merging galaxies were detected; hence, we consider this one of our next projects. This is a very interesting property since many observations predict the peak in accretion near the time of coalescence.

# 6

## Merging Systems in Isolated Environments. The Catalogue

### 6.1 Description of the Catalogue

We have assembled a catalogue of isolated merging systems. This catalogue contains 540 nearby ( $z < 0.1$ ) merging systems and it lists all the information we have used for our results. We show the same name for pairs and adding a 'b' to the name for the companion. Coordinates are centered in the individual merging galaxy. We present the morphology and merger stage as classified in this study. Fluxes are measured as explained in Chapter 2. Stellar masses ( $M_*$ ) and star formation rates (SFR) are listed in log-scale. This catalogue will be publicly available in the ViZiER website (<http://vizier.u-strasbg.fr>).

The columns of the catalogue are as follows:



Table 6.1 Columns description of the Catalogue. Credits: Calderón Castillo, P.

#	Name of Column	Units	Description
1	Name	String	Name is in the format PCC.# (for companion: PCC.# b)
2	RA	degrees	Right Ascension in decimal degrees
2	Dec	degrees	Declination in decimal degrees
3	z	float	Redshift
4	Morph	Integer	Morphology (0=Spiral, 1=Elliptical, 2=S0, 3=HD)
5	MrgStg	Integer	Merger Stage (1,2,3,4,5,6,7,8 = I,II,IIIa,IIIb,IIIc,IVa,IVb,V)
6	FUV	Jy	FUV flux
7	FUV_err	Jy	FUV flux error
8	NUV	Jy	NUV flux
9	NUV_err	Jy	NUV flux error
10	u	Jy	u flux
11	u_err	Jy	u flux error
12	g	Jy	g flux
13	g_err	Jy	g flux error
14	r	Jy	r flux
15	r_err	Jy	r flux error
16	i	Jy	i flux
17	i_err	Jy	i flux error
18	z	Jy	z flux
19	z_err	Jy	z flux error
20	W1	Jy	W1 flux
21	W1_err	Jy	W1 flux error
22	W2	Jy	W2 flux
23	W2_err	Jy	W2 flux error
24	W3	Jy	W3 flux
25	W3_err	Jy	W3 flux error
26	W4	Jy	W4 flux
27	W4_err	Jy	W4 flux error
28	W_flag	Integer	Photometry flag (0=ok, 1=two components within same aperture)
29	chi2	float	$\chi^2$ of the fit performed by MAGPHYS
30	logMst_Per2p5	$\log(M_*)$	Percentil 2.5% of the $\log(M_*)$
31	logMst_Per16	$\log(M_*)$	Percentil 16% of the $\log(M_*)$
32	logMst_Per50	$\log(M_*)$	Percentil 50% of the $\log(M_*)$
33	logMst_Per84	$\log(M_*)$	Percentil 84% of the $\log(M_*)$
34	logMst_Per97p5	$\log(M_*)$	Percentil 97.5% of the $\log(M_*)$
35	logSFR_Per2p5	$\log(M_* \text{yr}^{-1})$	Percentil 2.5% of the $\log(\text{SFR})$
36	logSFR_Per16	$\log(M_* \text{yr}^{-1})$	Percentil 16% of the $\log(\text{SFR})$
37	logSFR_Per50	$\log(M_* \text{yr}^{-1})$	Percentil 50% of the $\log(\text{SFR})$
38	logSFR_Per84	$\log(M_* \text{yr}^{-1})$	Percentil 84% of the $\log(\text{SFR})$
39	logSFR_Per97p5	$\log(M_* \text{yr}^{-1})$	Percentil 97.5% of the $\log(\text{SFR})$

# Bibliography

- Arp, H., *ApJS*, 14:1, November 1966.
- Assef, R. J., Stern, D., Kochanek, C. S., Blain, A. W., Brodwin, M., Brown, M. J. I., Donoso, E., Eisenhardt, P. R. M., Jannuzi, B. T., Jarrett, T. H., Stanford, S. A., Tsai, C.-W., Wu, J., & Yan, L., *ApJ*, 772:26, July 2013.
- Baldwin, J. A., Phillips, M. M., & Terlevich, R., *PASP*, 93:5–19, February 1981.
- Bell, E. F., McIntosh, D. H., Katz, N., & Weinberg, M. D., *ApJS*, 149:289–312, December 2003.
- Bertin, E. & Arnouts, S., *A&AS*, 117:393–404, June 1996.
- Brinchmann, J., Charlot, S., White, S. D. M., Tremonti, C., Kauffmann, G., Heckman, T., & Brinkmann, J., *MNRAS*, 351:1151–1179, July 2004.
- Bruzual, G. & Charlot, S., *MNRAS*, 344:1000–1028, October 2003.
- Butcher, H. & Oemler, Jr., A., *ApJ*, 226:559–565, December 1978.
- Catinella, B., Saintonge, A., Janowiecki, S., Cortese, L., Davé, R., Lemonias, J. J., Cooper, A. P., Schiminovich, D., Hummels, C. B., Fabello, S., Geréb, K., Kilborn, V., & Wang, J., *MNRAS*, 476:875–895, May 2018.
- Chang, Y.-Y., van der Wel, A., da Cunha, E., & Rix, H.-W., *ApJS*, 219:8, July 2015.
- Chung, A., van Gorkom, J. H., Kenney, J. D. P., & Vollmer, B., *ApJ*, 659:L115–L119, April 2007.
- Cluver, M. E., Jarrett, T. H., Hopkins, A. M., Driver, S. P., Liske, J., Gunawardhana, M. L. P., Taylor, E. N., Robotham, A. S. G., Alpaslan, M., Baldry, I., Brown, M. J. I., Peacock, J. A., Popescu, C. C., Tuffs, R. J., Bauer, A. E., Bland-Hawthorn, J., Colless, M., Holwerda, B. W., Lara-López, M. A., Leschinski, K., López-Sánchez, A. R., Norberg, P., Owers, M. S., Wang, L., & Wilkins, S. M., *ApJ*, 782:90, February 2014.
- da Cunha, E., Charlot, S., & Elbaz, D., *MNRAS*, 388:1595–1617, August 2008.
- Daddi, E., Dickinson, M., Morrison, G., Chary, R., Cimatti, A., Elbaz, D., Frayer, D., Renzini, A., Pope, A., Alexander, D. M., Bauer, F. E., Giavalisco, M., Huynh, M., Kurk, J., & Mignoli, M., *ApJ*, 670:156–172, November 2007.
- Darg, D. W., Kaviraj, S., Lintott, C. J., Schawinski, K., Sarzi, M., Bamford, S., Silk, J., Andreescu, D., Murray, P., Nichol, R. C., Rad-dick, M. J., Slosar, A., Szalay, A. S., Thomas, D., & Vandenberg, J., *MNRAS*, 401:1552–1563, January 2010.
- Di Matteo, P., Combes, F., Melchior, A.-L., & Semelin, B., *A&A*, 468:61–81, June 2007.
- Di Matteo, P., Bournaud, F., Martig, M., Combes, F., Melchior, A.-L., & Semelin, B., *A&A*, 492:31–49, December 2008.

- Di Matteo, T., Springel, V., & Hernquist, L., *Nature*, 433:604–607, February 2005.
- Diehl, R., Halloin, H., Kretschmer, K., Lichti, G. G., Schönfelder, V., Strong, A. W., von Kienlin, A., Wang, W., Jean, P., Knödseder, J., Roques, J.-P., Weidenspointner, G., Schanne, S., Hartmann, D. H., Winkler, C., & Wunderer, C., *Nature*, 439:45–47, January 2006.
- Dressler, A., *ApJ*, 236:351–365, March 1980.
- Elbaz, D., Daddi, E., Le Borgne, D., Dickinson, M., Alexander, D. M., Chary, R.-R., Starck, J.-L., Brandt, W. N., Kitzbichler, M., MacDonald, E., Nonino, M., Popesso, P., Stern, D., & Vanzella, E., *A&A*, 468:33–48, June 2007.
- Elbaz, D., Dickinson, M., Hwang, H. S., Díaz-Santos, T., Magdis, G., Magnelli, B., Le Borgne, D., Galliano, F., Pannella, M., Charnial, P., Armus, L., Charmandaris, V., Daddi, E., Aussel, H., Popesso, P., Kartaltepe, J., Altieri, B., Valtchanov, I., Coia, D., Dannerbauer, H., Dasyra, K., Leiton, R., Mazzarella, J., Alexander, D. M., Buat, V., Burgarella, D., Chary, R.-R., Gilli, R., Ivison, R. J., Juneau, S., Le Floch, E., Lutz, D., Morrison, G. E., Mullaney, J. R., Murphy, E., Pope, A., Scott, D., Brodwin, M., Calzetti, D., Cesarsky, C., Charlot, S., Dole, H., Eisenhardt, P., Ferguson, H. C., Förster Schreiber, N., Frayer, D., Giavalisco, M., Huynh, M., Koekemoer, A. M., Papovich, C., Reddy, N., Surace, C., Teplitz, H., Yun, M. S., & Wilson, G., *A&A*, 533:A119, September 2011.
- Ellison, S. L., Patton, D. R., Simard, L., & McConnachie, A. W., *AJ*, 135:1877–1899, May 2008.
- Ellison, S. L., Patton, D. R., Mendel, J. T., & Scudder, J. M., *MNRAS*, 418:2043–2053, December 2011.
- Ellison, S. L., Mendel, J. T., Patton, D. R., & Scudder, J. M., *MNRAS*, 435:3627–3638, November 2013.
- Flynn, C., Holmberg, J., Portinari, L., Fuchs, B., & Jahreiß, H., *MNRAS*, 372:1149–1160, November 2006.
- Font, A. S., Bower, R. G., McCarthy, I. G., Benson, A. J., Frenk, C. S., Helly, J. C., Lacey, C. G., Baugh, C. M., & Cole, S., *MNRAS*, 389:1619–1629, October 2008.
- Gehrels, N., *ApJ*, 303:336–346, April 1986.
- Gunn, J. E. & Gott, III, J. R., *ApJ*, 176:1, August 1972.
- Holincheck, A. J., Wallin, J. F., Borne, K., Fortson, L., Lintott, C., Smith, A. M., Bamford, S., Keel, W. C., & Parrish, M., *MNRAS*, 459:720–745, June 2016.
- Hopkins, P. F., Hernquist, L., Cox, T. J., Younger, J. D., & Besla, G., *ApJ*, 688:757–769, December 2008.
- Hwang, H. S., Elbaz, D., Lee, J. C., Jeong, W.-S., Park, C., Lee, M. G., & Lee, H. M., *A&A*, 522:A33, November 2010.
- Hwang, H. S., Elbaz, D., Dickinson, M., Charmandaris, V., Daddi, E., Le Borgne, D., Buat,

- V., Magdis, G. E., Altieri, B., Aussel, H., Coia, D., Dannerbauer, H., Dasyra, K., Kartaltepe, J., Leiton, R., Magnelli, B., Popesso, P., & Valtchanov, I., *A&A*, 535:A60, November 2011.
- Hwang, J.-S. & Park, C., *ApJ*, 805:131, June 2015.
- Jáchym, P., Palouš, J., Köppen, J., & Combes, F., *A&A*, 472:5–20, September 2007.
- Janowiecki, S., Catinella, B., Cortese, L., Sain-  
tonge, A., Brown, T., & Wang, J., *MNRAS*,  
466:4795–4812, April 2017.
- Jarrett, T. H., Cohen, M., Masci, F., Wright,  
E., Stern, D., Benford, D., Blain, A., Carey,  
S., Cutri, R. M., Eisenhardt, P., Lonsdale, C.,  
Mainzer, A., Marsh, K., Padgett, D., Petty,  
S., Ressler, M., Skrutskie, M., Stanford, S.,  
Surace, J., Tsai, C. W., Wheelock, S., & Yan,  
D. L., *ApJ*, 735:112, July 2011.
- Jarrett, T. H., Masci, F., Tsai, C. W., Petty,  
S., Cluver, M. E., Assef, R. J., Benford, D.,  
Blain, A., Bridge, C., Donoso, E., Eisenhardt,  
P., Koribalski, B., Lake, S., Neill, J. D., Seib-  
ert, M., Sheth, K., Stanford, S., & Wright, E.,  
*AJ*, 145:6, January 2013.
- Jarrett, T. H., Cluver, M. E., Magoulas, C.,  
Bilicki, M., Alpaslan, M., Bland-Hawthorn,  
J., Brough, S., Brown, M. J. I., Croom,  
S., Driver, S., Holwerda, B. W., Hopkins,  
A. M., Loveday, J., Norberg, P., Peacock,  
J. A., Popescu, C. C., Sadler, E. M., Taylor,  
E. N., Tuffs, R. J., & Wang, L., *ApJ*, 836:182,  
February 2017.
- Karim, A., Schinnerer, E., Martínez-Sansigre,  
A., Sargent, M. T., van der Wel, A., Rix, H.-  
W., Ilbert, O., Smolčić, V., Carilli, C., Pan-  
nella, M., Koekemoer, A. M., Bell, E. F., &  
Salvato, M., *ApJ*, 730:61, April 2011.
- Kauffmann, G., Heckman, T. M., White,  
S. D. M., Charlot, S., Tremonti, C., Brinch-  
mann, J., Bruzual, G., Peng, E. W., Seibert,  
M., Bernardi, M., Blanton, M., Brinkmann,  
J., Castander, F., Csábai, I., Fukugita, M.,  
Ivezic, Z., Munn, J. A., Nichol, R. C., Pad-  
manabhan, N., Thakar, A. R., Weinberg,  
D. H., & York, D., *MNRAS*, 341:33–53, May  
2003.
- Kewley, L. J., Groves, B., Kauffmann, G.,  
& Heckman, T., *MNRAS*, 372:961–976,  
November 2006.
- Larson, R. B. & Tinsley, B. M., *ApJ*, 219:46–59,  
January 1978.
- Larson, R. B., Tinsley, B. M., & Caldwell,  
C. N., *ApJ*, 237:692–707, May 1980.
- Lee, J. C., Hwang, H. S., & Ko, J., *ApJ*, 774:62,  
September 2013.
- McCarthy, I. G., Frenk, C. S., Font, A. S.,  
Lacey, C. G., Bower, R. G., Mitchell, N. L.,  
Balogh, M. L., & Theuns, T., *MNRAS*, 383:  
593–605, January 2008.
- Mihos, J. C. & Hernquist, L., *ApJ*, 425:L13–  
L16, April 1994a.
- Mihos, J. C. & Hernquist, L., *ApJ*, 431:L9–L12,  
August 1994b.

- Moore, B., Lake, G., & Katz, N., *ApJ*, 495:139–151, March 1998.
- Moster, B. P., Macciò, A. V., Somerville, R. S., Naab, T., & Cox, T. J., *MNRAS*, 415:3750–3770, August 2011.
- Noeske, K. G., Weiner, B. J., Faber, S. M., Papovich, C., Koo, D. C., Somerville, R. S., Bundy, K., Conselice, C. J., Newman, J. A., Schiminovich, D., Le Floch, E., Coil, A. L., Rieke, G. H., Lotz, J. M., Primack, J. R., Barmby, P., Cooper, M. C., Davis, M., Ellis, R. S., Fazio, G. G., Guhathakurta, P., Huang, J., Kassin, S. A., Martin, D. C., Phillips, A. C., Rich, R. M., Small, T. A., Willmer, C. N. A., & Wilson, G., *ApJ*, 660:L43–L46, May 2007.
- Oh, K., Sarzi, M., Schawinski, K., & Yi, S. K., *ApJS*, 195:13, August 2011.
- Pannella, M., Carilli, C. L., Daddi, E., McCracken, H. J., Owen, F. N., Renzini, A., Strazzullo, V., Civano, F., Koekemoer, A. M., Schinnerer, E., Scoville, N., Smolčić, V., Taniguchi, Y., Aussel, H., Kneib, J. P., Ilbert, O., Mellier, Y., Salvato, M., Thompson, D., & Willott, C. J., *ApJ*, 698:L116–L120, June 2009.
- Pannella, M., Elbaz, D., Daddi, E., Dickinson, M., Hwang, H. S., Schreiber, C., Strazzullo, V., Aussel, H., Bethermin, M., Buat, V., Charmandaris, V., Cibinel, A., Juneau, S., Ivison, R. J., Le Borgne, D., Le Floch, E., Leiton, R., Lin, L., Magdis, G., Morrison, G. E., Mullaney, J., Onodera, M., Renzini, A., Salim, S., Sargent, M. T., Scott, D., Shu, X., & Wang, T., *ApJ*, 807:141, July 2015.
- Park, J., Smith, R., & Yi, S. K., *ApJ*, 845:128, August 2017.
- Renzini, A. & Peng, Y.-j., *ApJ*, 801:L29, March 2015.
- Rhee, J., Smith, R., Choi, H., Yi, S. K., Jaffé, Y., Candlish, G., & Sánchez-Jánsen, R., *ApJ*, 843:128, July 2017.
- Rodighiero, G., Renzini, A., Daddi, E., Baronchelli, I., Berta, S., Cresci, G., Franceschini, A., Gruppioni, C., Lutz, D., Mancini, C., Santini, P., Zamorani, G., Silverman, J., Kashino, D., Andreani, P., Cimatti, A., Sánchez, H. D., Le Floch, E., Magnelli, B., Popesso, P., & Pozzi, F., *MNRAS*, 443:19–30, September 2014.
- Rodriguez-Gomez, V., Genel, S., Vogelsberger, M., Sijacki, D., Pillepich, A., Sales, L. V., Torrey, P., Snyder, G., Nelson, D., Springel, V., Ma, C.-P., & Hernquist, L., *MNRAS*, 449:49–64, May 2015.
- Salim, S., Rich, R. M., Charlot, S., Brinchmann, J., Johnson, B. D., Schiminovich, D., Seibert, M., Mallery, R., Heckman, T. M., Forster, K., Friedman, P. G., Martin, D. C., Morrissey, P., Neff, S. G., Small, T., Wyder, T. K., Bianchi, L., Donas, J., Lee, Y.-W., Madore, B. F., Miliard, B., Szalay, A. S., Welsh, B. Y., & Yi, S. K., *ApJS*, 173:267–292, December 2007.
- Sanders, D. B., Mazzarella, J. M., Kim, D.-C., Surace, J. A., & Soifer, B. T., *AJ*, 126:1607–1664, October 2003.

- Sartori, L. F., Schawinski, K., Treister, E., Trakhtenbrot, B., Koss, M., Shirazi, M., & Oh, K., *MNRAS*, 454:3722–3742, December 2015.
- Satyapal, S., Ellison, S. L., McAlpine, W., Hickox, R. C., Patton, D. R., & Mendel, J. T., *MNRAS*, 441:1297–1304, June 2014.
- Schiminovich, D., Wyder, T. K., Martin, D. C., Johnson, B. D., Salim, S., Seibert, M., Treyer, M. A., Budavári, T., Hoopes, C., Zamojski, M., Barlow, T. A., Forster, K. G., Friedman, P. G., Morrissey, P., Neff, S. G., Small, T. A., Bianchi, L., Donas, J., Heckman, T. M., Lee, Y.-W., Madore, B. F., Milliard, B., Rich, R. M., Szalay, A. S., Welsh, B. Y., & Yi, S., *ApJS*, 173:315–341, December 2007.
- Schlafly, E. F. & Finkbeiner, D. P., *ApJ*, 737: 103, August 2011.
- Schreiber, C., Pannella, M., Elbaz, D., Béthermin, M., Inami, H., Dickinson, M., Magnelli, B., Wang, T., Aussel, H., Daddi, E., Juneau, S., Shu, X., Sargent, M. T., Buat, V., Faber, S. M., Ferguson, H. C., Giavalisco, M., Koekemoer, A. M., Magdis, G., Morrison, G. E., Papovich, C., Santini, P., & Scott, D., *A&A*, 575:A74, March 2015.
- Schreiber, C., Pannella, M., Leiton, R., Elbaz, D., Wang, T., Okumura, K., & Labbé, I., *A&A*, 599:A134, March 2017.
- Shirazi, M. & Brinchmann, J., *MNRAS*, 421: 1043–1063, April 2012.
- Smith, R., Davies, J. I., & Nelson, A. H., *MNRAS*, 405:1723–1735, July 2010.
- Smith, R., Sánchez-Janssen, R., Fellhauer, M., Puzia, T. H., Aguerri, J. A. L., & Farias, J. P., *MNRAS*, 429:1066–1079, February 2013.
- Smith, R., Sánchez-Janssen, R., Beasley, M. A., Candlish, G. N., Gibson, B. K., Puzia, T. H., Janz, J., Knebe, A., Aguerri, J. A. L., Lisker, T., Hensler, G., Fellhauer, M., Ferrarese, L., & Yi, S. K., *MNRAS*, 454:2502–2516, December 2015.
- Springel, V. & Hernquist, L., *ApJ*, 622:L9–L12, March 2005.
- Stern, D., Assef, R. J., Benford, D. J., Blain, A., Cutri, R., Dey, A., Eisenhardt, P., Griffith, R. L., Jarrett, T. H., Lake, S., Masci, F., Petty, S., Stanford, S. A., Tsai, C.-W., Wright, E. L., Yan, L., Harrison, F., & Madsen, K., *ApJ*, 753:30, July 2012.
- Taylor, E. N., Hopkins, A. M., Baldry, I. K., Brown, M. J. I., Driver, S. P., Kelvin, L. S., Hill, D. T., Robotham, A. S. G., Bland-Hawthorn, J., Jones, D. H., Sharp, R. G., Thomas, D., Liske, J., Loveday, J., Norberg, P., Peacock, J. A., Bamford, S. P., Brough, S., Colless, M., Cameron, E., Conselice, C. J., Croom, S. M., Frenk, C. S., Gunawardhana, M., Kuijken, K., Nichol, R. C., Parkinson, H. R., Phillipps, S., Pimbblet, K. A., Popescu, C. C., Prescott, M., Sutherland, W. J., Tuffs, R. J., van Kampen, E., & Wijesinghe, D., *MNRAS*, 418:1587–1620, December 2011.
- Toomre, A. & Toomre, J., *ApJ*, 178:623–666, December 1972.

- van de Voort, F., Davis, T. A., Matsushita, S., Rowlands, K., Shabala, S. S., Allison, J. R., Ting, Y.-S., Sansom, A. E., & van der Werf, P. P., *MNRAS*, 476:122–132, May 2018.
- Varenius, E., Conway, J. E., Martí-Vidal, I., Aalto, S., Barcos-Muñoz, L., König, S., Pérez-Torres, M. A., Deller, A. T., Moldón, J., Gallagher, J. S., Yoast-Hull, T. M., Horellou, C., Morabito, L. K., Alberdi, A., Jackson, N., Beswick, R., Carozzi, T. D., Wucknitz, O., & Ramírez-Olivencia, N., *A&A*, 593: A86, September 2016.
- Veilleux, S., Kim, D.-C., & Sanders, D. B., *ApJS*, 143:315–376, December 2002.
- Véron-Cetty, M.-P. & Véron, P., *A&A*, 518:A10, July 2010.
- Vorontsov-Velyaminov, B. A., Noskova, R. I., & Arkhipova, V. P., *Astronomical and Astrophysical Transactions*, 20:717–959, December 2001.
- Weinzirl, T. *Probing Galaxy Evolution by Unveiling the Structure of Massive Galaxies Across Cosmic Time and Diverse Environments*. 2015.
- Weniger, J., Theis, C., & Harfst, S., *Astronomische Nachrichten*, 330:1019, December 2009.
- Whitaker, K. E., van Dokkum, P. G., Brammer, G., & Franx, M., *ApJ*, 754:L29, August 2012.
- Whitaker, K. E., Franx, M., Leja, J., van Dokkum, P. G., Henry, A., Skelton, R. E., Fumagalli, M., Momcheva, I. G., Brammer, G. B., Labbé, I., Nelson, E. J., & Rigby, J. R., *ApJ*, 795:104, November 2014.
- Wuyts, S., Förster Schreiber, N. M., van der Wel, A., Magnelli, B., Guo, Y., Genzel, R., Lutz, D., Aussel, H., Barro, G., Berta, S., Cava, A., Graciá-Carpio, J., Hathi, N. P., Huang, K.-H., Kocevski, D. D., Koekemoer, A. M., Lee, K.-S., Le Floc’h, E., McGrath, E. J., Nordon, R., Popesso, P., Pozzi, F., Riguccini, L., Rodighiero, G., Saintonge, A., & Tacconi, L., *ApJ*, 742:96, December 2011.
- Young, L. M., Serra, P., Krajnović, D., & Duc, P.-A., *MNRAS*, 477:2741–2759, June 2018.
- Yuan, H. B., Liu, X. W., & Xiang, M. S., *MNRAS*, 430:2188–2199, April 2013.





# A

## Morphology Classification



### A.1 Examples of morphology

In Sec. 2.3.1, we show the distribution of the galaxies morphology as classified in this study. Here we present an example of each morphology classification. Figure A.1 shows, from top to bottom, a spiral, an elliptical, a lenticular (S0) and a highly-disturbed galaxy, from our merger sample. Specifically, to be classified as an spiral, galaxies will have to show clear spiral arms not heavily perturbed. Ellipticals show red colours and round shapes with a bright nucleus. Lenticular galaxies show similar morphologies than ellipticals, but they all show a clear disk. Finally, highly-disturbed galaxies are all galaxies which can not be classified in any of the previous classes. These could show highly-perturbed spiral arms, various shells, tidal features, etc.

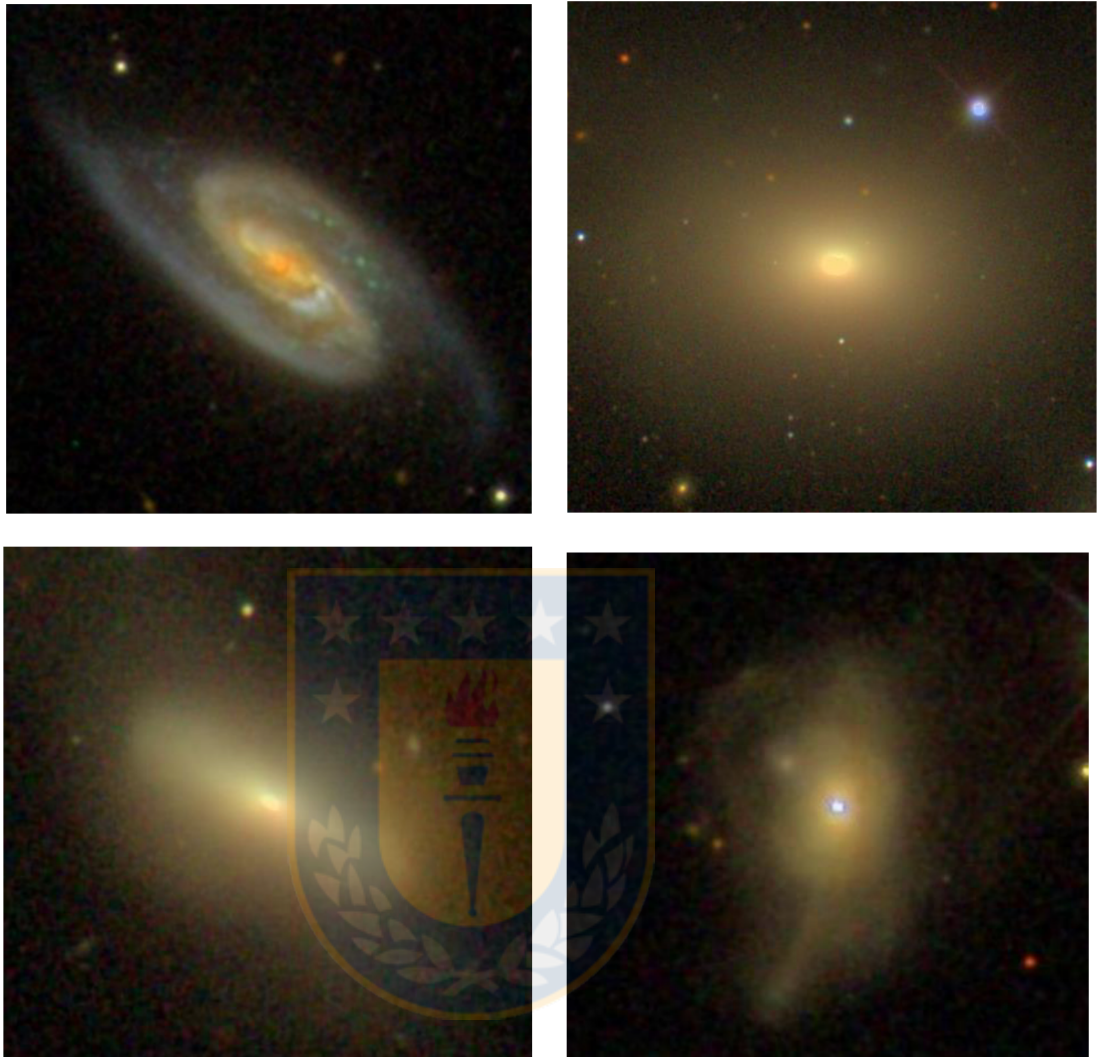


Figure A.1 Examples of the morphology classification: Spiral (top-left), Elliptical (top-right), Lenticular (bottom-left) and highly-disturbed (bottom-right) galaxies. *Credits: Images taken from SDSS*

# B

## Survey Parameters

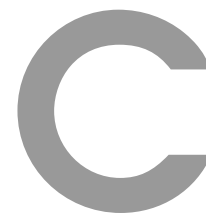
### B.1 Photometric Parameters used for the Photometry

To perform the photometry, we have searched for the relevant parameters from each survey. We have assembled a table (Table B.1) with the reference information to use these surveys.

Table B.1 Table of relevant parameters from Surveys. Relevant parameters of the filters and images used from the different surveys. *Credits: Calderón Castillo, P.*

Survey	Band	Effective wavelength	Zero point magnitude	Resolution (arcsec)	Sensitivity	Pixel Scale (arcsec/pixel)	$\Delta m$ ( $m_{AB} = m_{Vega} + \Delta m$ )
GALEX	FUV	1528 Å	18.82	4.2	20 (AIS <sup>1</sup> ) / 22.7 (MIS <sup>2</sup> ) / 24.8 (DIS <sup>3</sup> )	1.5	2.22
	NUV	2271 Å	20.08	5.3	21 / 22.7 / 24.4 (ABmag)	1.5	1.69
SDSS	u	3551 Å	22.5	1.3	22.0 (ABmag)	0.396	0.91
	g	4686 Å	22.5		22.2 (ABmag)	0.396	-0.08
	r	6165 Å	22.5		22.2 (ABmag)	0.396	0.16
	i	7481 Å	22.5		21.3 (ABmag)	0.396	0.37
	z	8931 Å	22.5		20.5 (ABmag)	0.396	0.54
WISE	W1	3.4 μm	20.73	6.1	0.08 mJy (16.5 Vegamag)	1.375	2.699
	W2	4.6 μm	19.56	6.4	0.11 mJy (15.5 Vegamag)	1.375	3.339
	W3	12 μm	17.60	6.5	1 mJy (11.2 Vegamag)	1.375	5.174
	W4	22 μm	12.98	12.0	6 mJy (7.9 Vegamag)	1.375	6.620

<sup>1</sup>All-sky <sup>2</sup>Medium, and <sup>3</sup>Deep Imaging Surveys from GALEX.



## Examples of Apertures

### **C.1 Examples of Apertures depending on different SExtractor parameters**

Here, we show more examples of the different apertures SExtractor calculates depending on the parameters  $\sigma$  and n-deblending (see Sec. 2.3.2). Each figure shows 3 examples for each galaxy using different  $\sigma$  and n-deblending, which are described in each caption. We show the best aperture at the bottom of each figure.

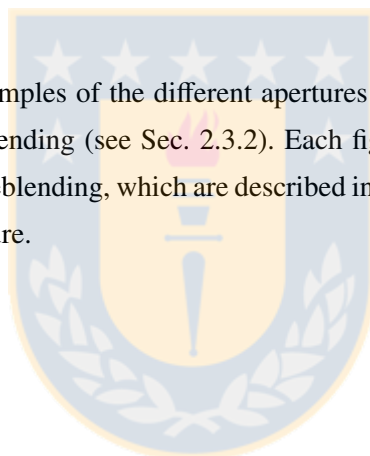




Figure C.1 Changing the sky-threshold and n-deblending II. SExtractor images showing apertures for, from top to bottom,  $\sigma = 1.5$ , n-deblending=32.  $\sigma = 5.0$ , n-deblending=32.  $\sigma = 3.0$ , n-deblending=2.

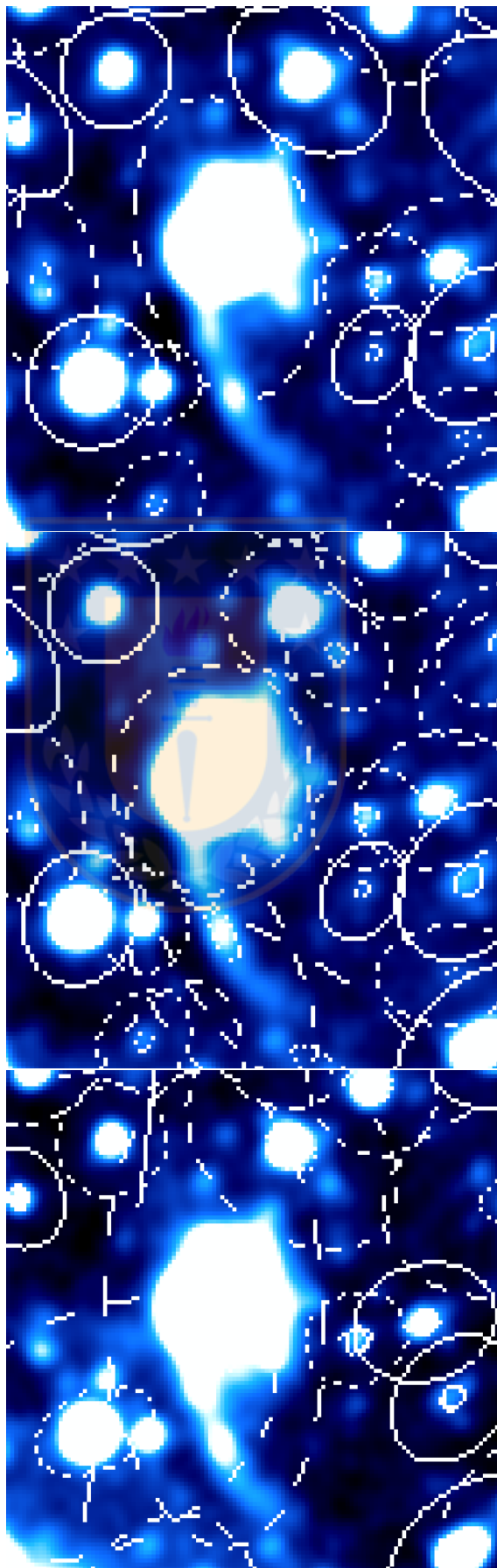


Figure C.2 Changing the sky-threshold and n-deblending III. SExtractor images showing apertures for, from top to bottom,  $\sigma = 1.5$ , n-deblending=2.  $\sigma = 1.5$ , n-deblending=32.  $\sigma = 1.5$ , n-deblending=4.

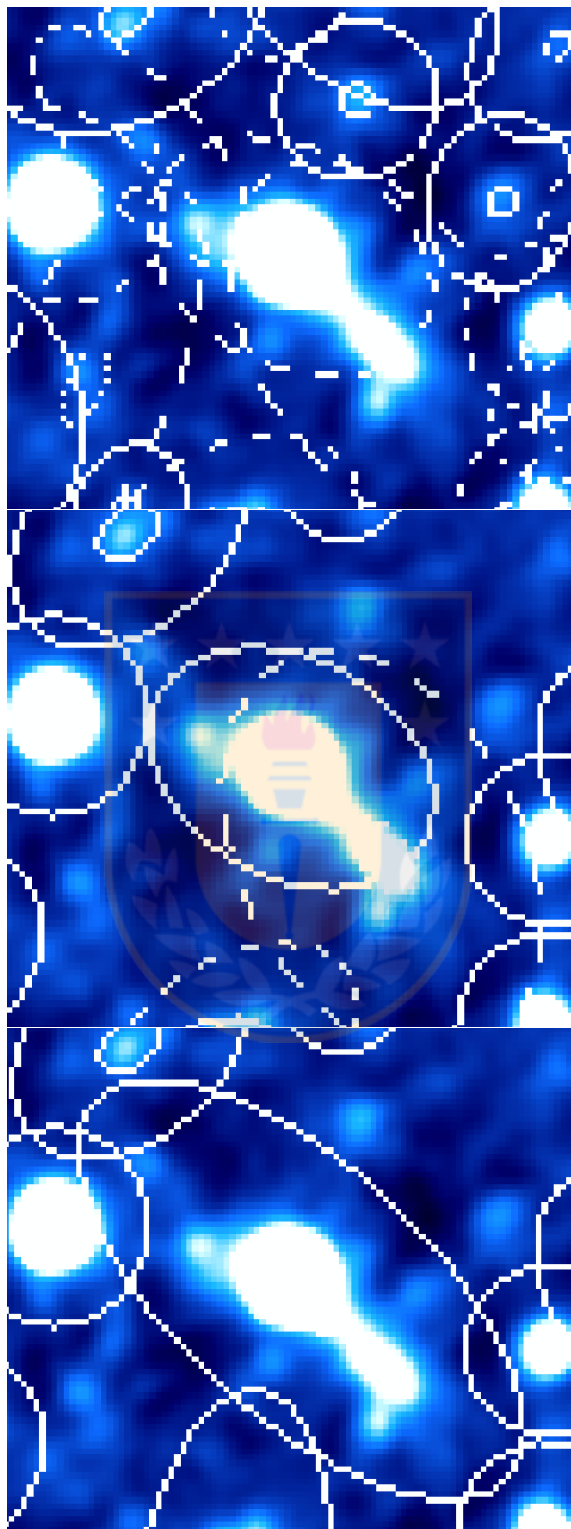


Figure C.3 Changing the sky-threshold and n-deblending IV. SExtractor images showing apertures for, from top to bottom,  $\sigma = 1.5$ , n-deblending=32.  $\sigma = 5.0$ , n-deblending=32.  $\sigma = 5.0$ , n-deblending=2.

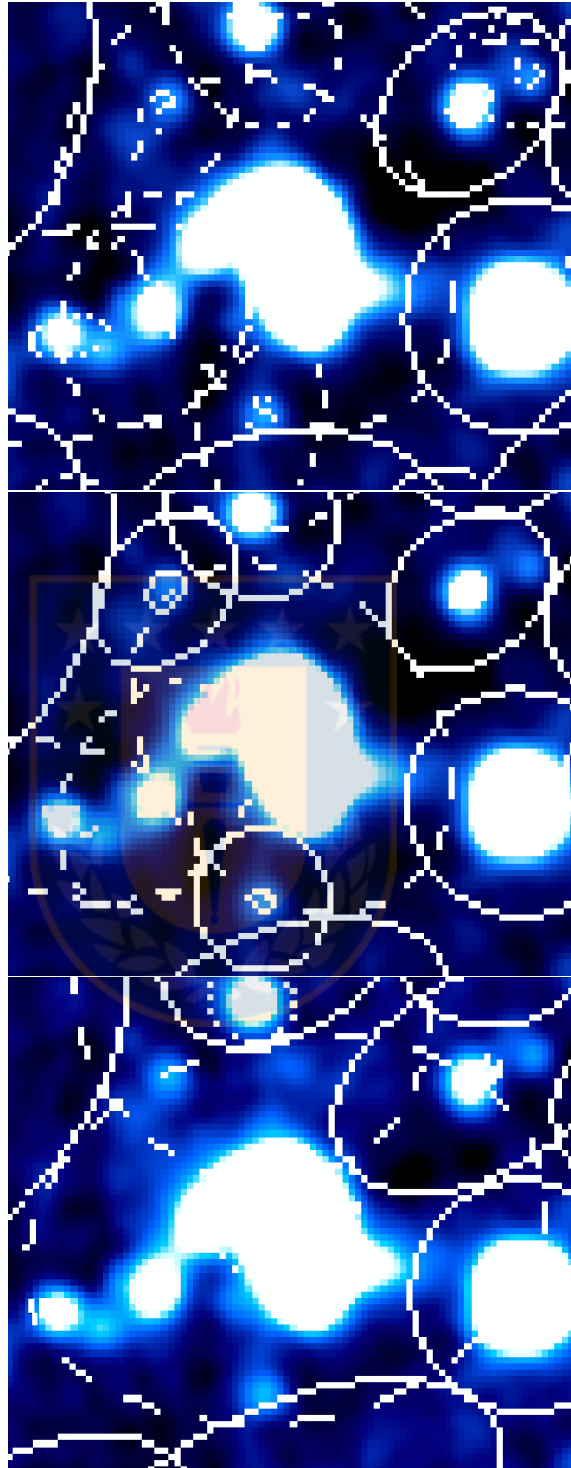


Figure C.4 Changing the sky-threshold and n-deblending V. SExtractor images showing apertures for, from top to bottom,  $\sigma = 1.5$ , n-deblending=32.  $\sigma = 3.0$ , n-deblending=32.  $\sigma = 3.0$ , n-deblending=4.



# D

## Testing for dependence on the Flux differences with Catalogues

### D.1 Testing for dependencies

In Sec. 2.3.2, we showed the comparison between our measured GALEX NUV fluxes and the GALEX GR6/GR7 catalog, the SDSS DR13 r-band fluxes of our measurements and the values listed by CHANG15, and our measured WISE W1 fluxes and the catalogued values shown in AllWISE tabulated as gmag. Here we coloured the comparisons in order to look for any dependencies in morphology, merger stage or photometry flag. The photometry flag shows whether the apertures, measured by our semi-automated method, are completely separated or joined (both galaxies are within the same aperture).

Figure D.1 shows the fluxes we measured from GALEX NUV (top panels), SDSS r-band (middle panels), and WISE W1 images (bottom panels) compared to the ones catalogued by GALEX, SDSS, and AllWISE. They are coloured by morphology (left panels), merger stage (middle panels), and photometry flag (right panels). The correlations do not show a clear dependency on any of these parameters. However, spirals and highly-disturbed galaxies show a larger scatter. The scatter in the SDSS (middle-middle panel) is dominated by merging galaxies at merger stage IIIb, where a large fraction of the merging galaxies are either spiral or highly-disturbed. This leads to the conclusion that differences in these values are related mainly to the photometry performed.

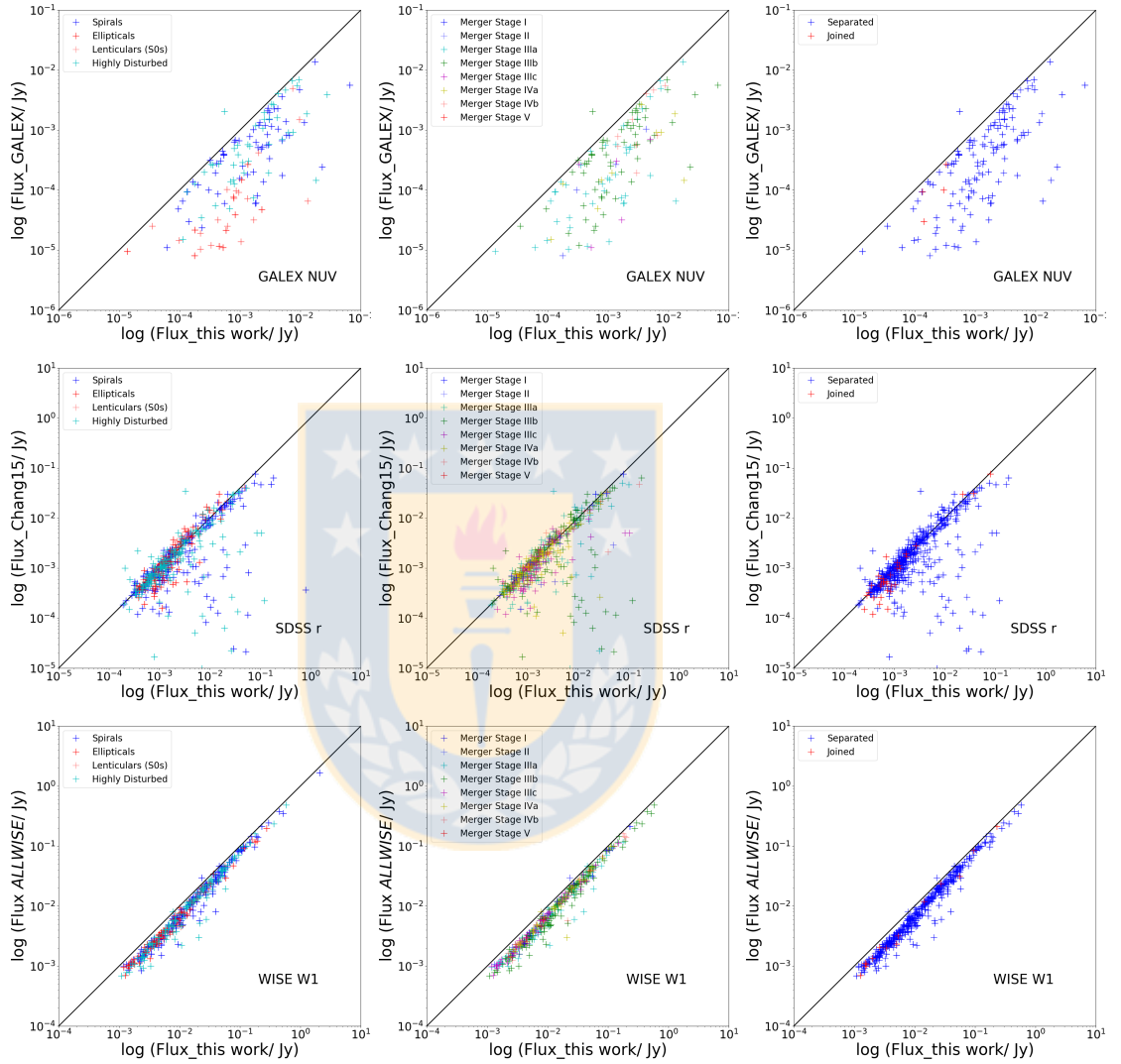


Figure D.1 Flux comparison to catalogues coloured by morphology. Comparison between our GALEX NUV (top panels), SDSS r-band (middle panels), and WISE W1 (bottom panels) measured fluxes and GALEX, SDSS, and AllWISE catalogued values. Coloured by morphology (left panels), merger stage (middle panels), and photometry flag (right panels). *Credits: Calderón Castillo, P.*

# E

## MAGPHYS SED fits

### E.1 MAGPHYS SED fits

Some examples of fitted SEDs are shown in Figures E.1 and E.2. The figures show six examples of MAGPHYS SED fit results. Each row shows the SED fits of the same object, using all the filters (GALEX, SDSS and WISE) on the left and the SED fits using SDSS+WISE only on the right. The top panel of each fit shows the photometric points in red, the best SED fit in black and the unattenuated SED in blue. The reduced chi-squared ( $\chi^2$ ) of the fit is shown on the top-right corner of each main panel. The panel below shows the residual between the fit and the photometric points. In the lower panels of each fit, we show four probability distribution functions (PDFs) of some of the parameters estimated by MAGPHYS. From left to right, we show the PDFs of the  $M_*$ , the sSFR, the SFR and the dust mass ( $M_{\text{dust}}$ ).

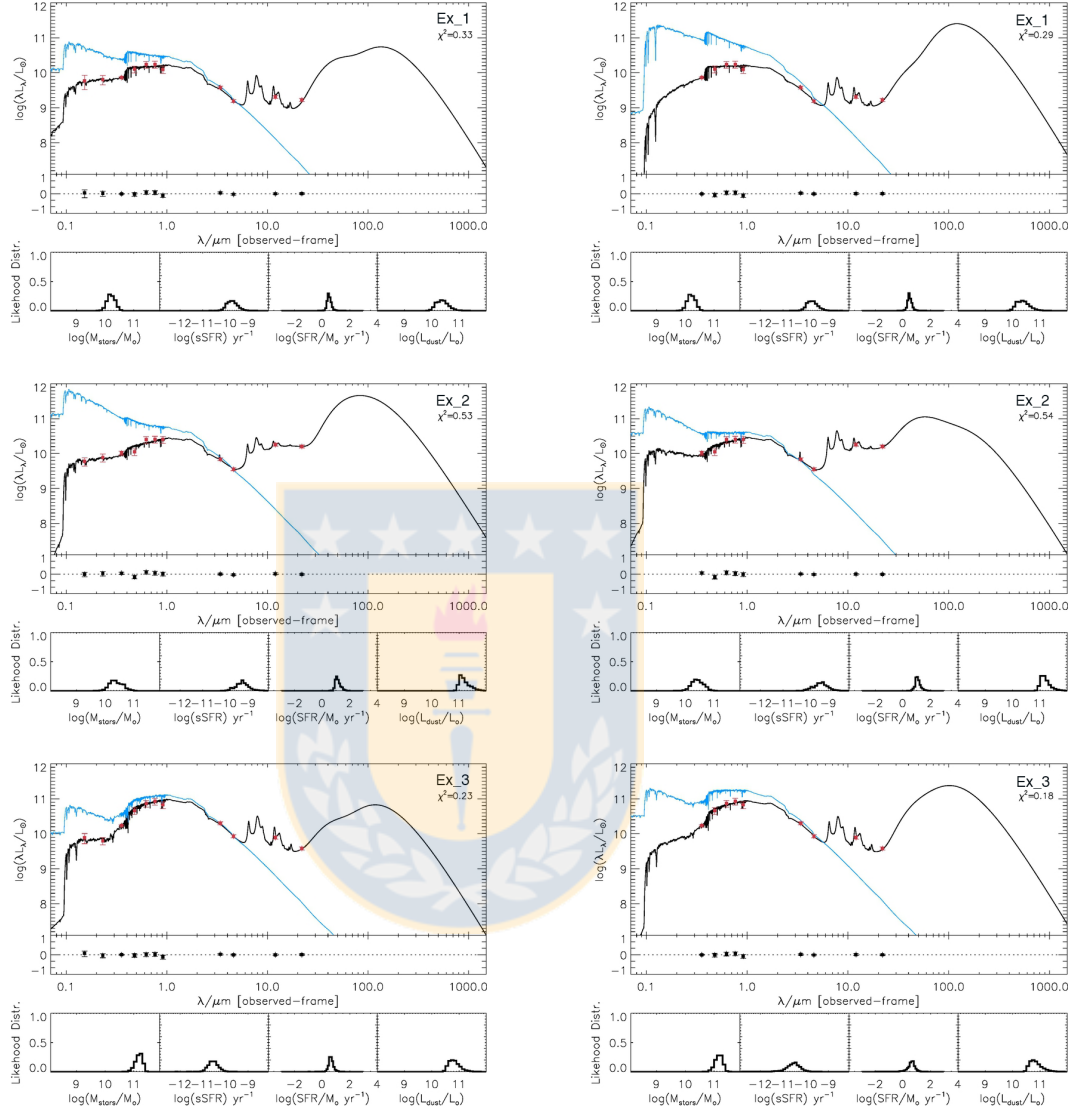


Figure E.1 Examples of SED fittings using MAGPHYS, for some of our mergers using GALEX+SDSS+WISE filters (left) and using SDSS+WISE only (right). We show the SED fits for the same object in each row. In the upper panel, the red points show our photometric data, the black curve shows the best fitted SED to the photometry, and the blue curve shows the unattenuated SED. On the top-right corner, the  $\chi_r^2$  of the fit is shown. The middle panel shows the residuals of the SED fit. In the lower part, there are four small panels showing the PDFs of the different parameters estimated by MAGPHYS. In this case, we show the PDFs of the  $M_*$ , sSFR, SFR and  $M_{\text{dust}}$  of each fit. *Credits: Calderón Castillo, P.*

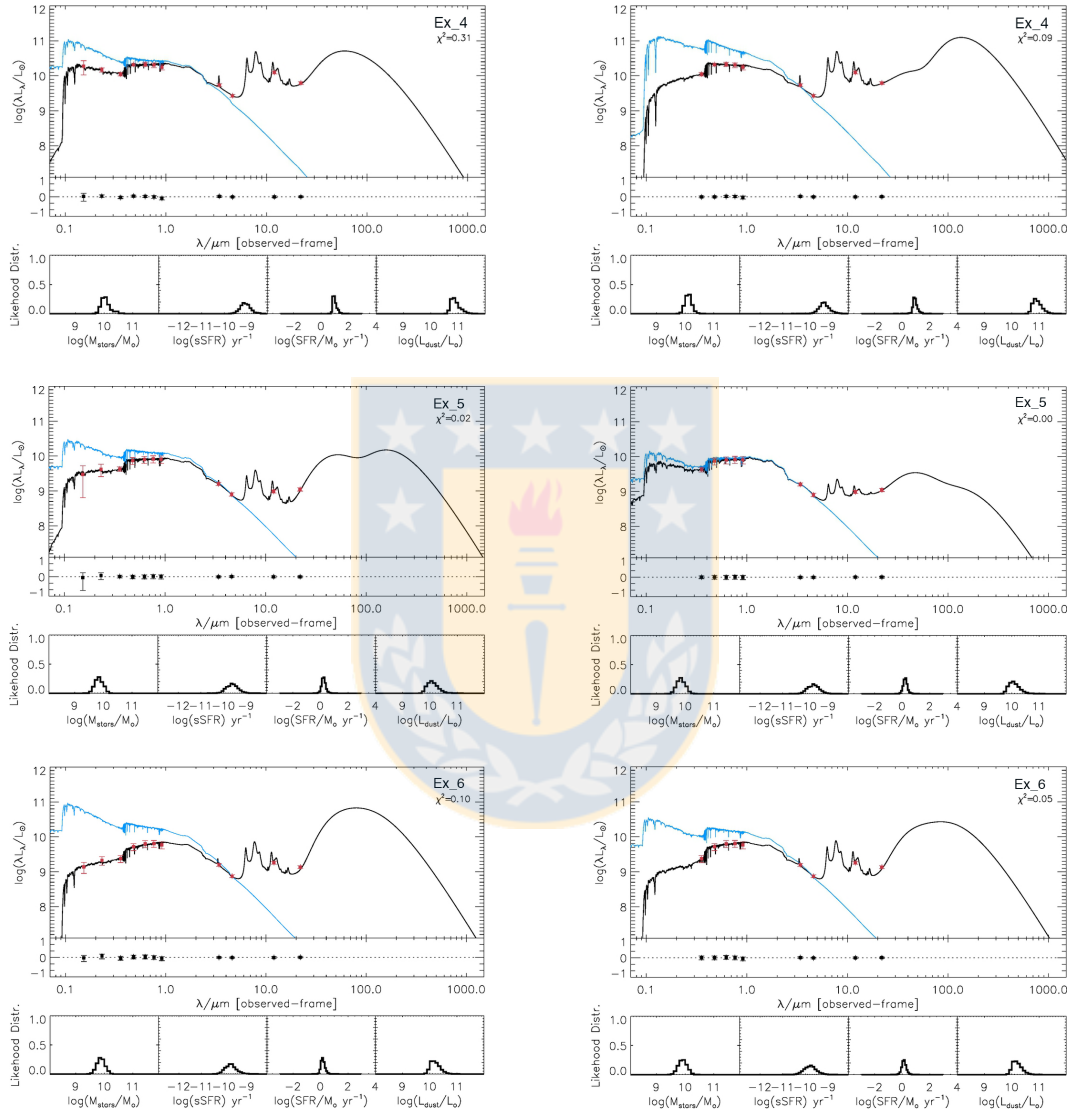


Figure E.2 Examples of SED fittings using MAGPHYS... continued, as explained in Fig. E.1.  
Credits: Calderón Castillo, P.

# F

## Testing for dependencies in $M_*$ and SFR differences with Catalogues

### F.1 Testing for dependencies

We present comparisons between our estimates of  $M_*$  and SFR to the estimates made by CHANG+15 (shown in Sec. 2.3.4) coloured by different parameters to look for any dependencies. Figure F.1 shows the comparison between our  $M_*$  (top) and SFR (bottom) results and CHANG15's  $M_*$  and SFR, coloured by merger stage (left panel) and photometry flag (right panel). We can see that the correlations do not show any dependency in merger stage or photometry flag.

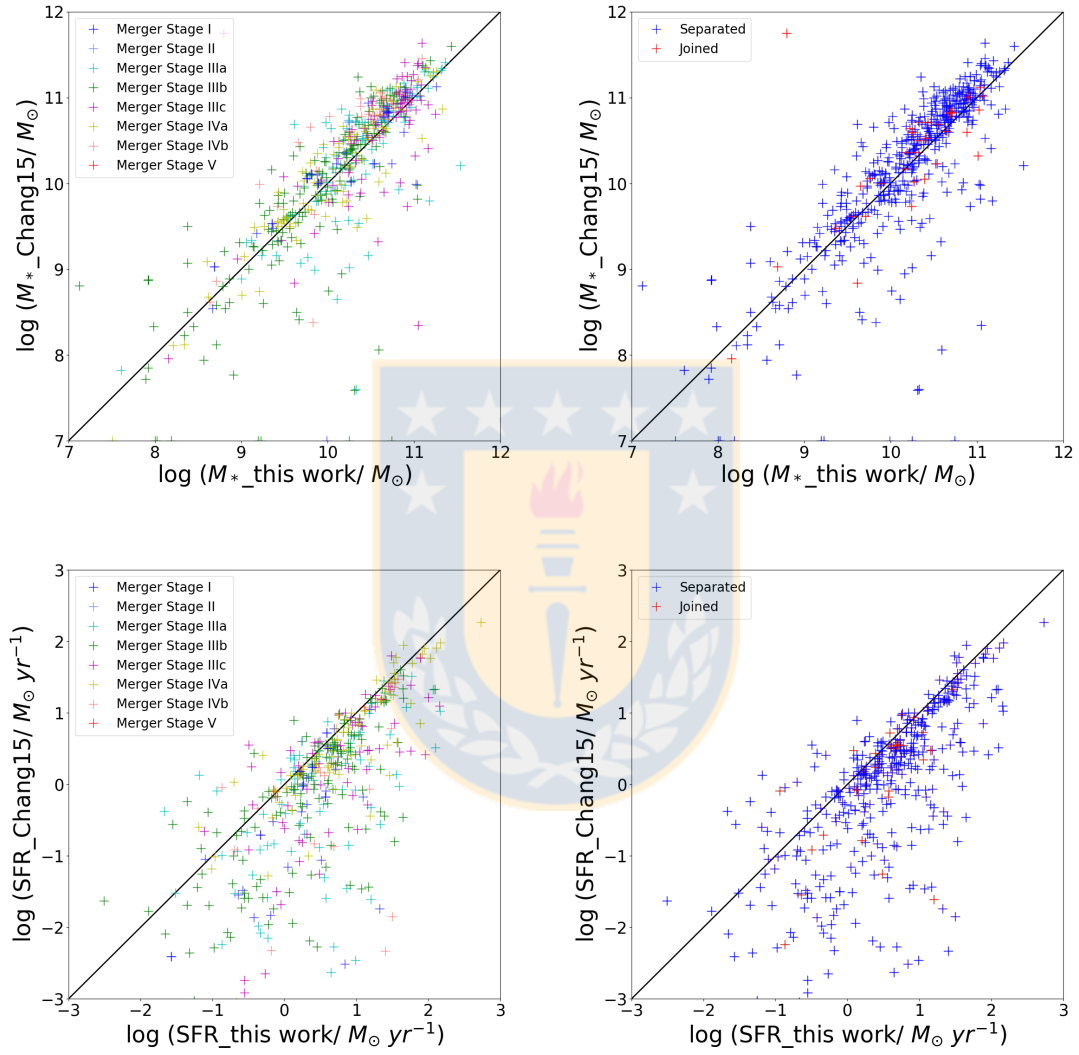


Figure F.1  $M_*$  and SFR comparison to CHANG15 coloured by merger stage and photometry flag. Comparison between the  $M_*$  (top panels) and SFR (bottom panels) estimated by MAGPHYS using the SDSS+WISE filters only and CHANG15's results, coloured by merger stage (left panels) and photometry flag (right panels). Credits: Calderón Castillo, P.



## Testing for SF mode dependence on Stellar Mass

### G.1 Stellar Mass bins



To identify any dependence of the SF mode on stellar mass, we have separated the mergers into three stellar mass bins. The stellar mass bins are calculated from the stellar mass of the system (primary's plus secondary's stellar masses). The low-mass bin shows stellar masses:  $\log(M_*/M_\odot) < 9.5$ , the medium-mass bin shows stellar masses within the range:  $9.5 < \log(M_*/M_\odot) < 10.5$ , and the high-mass bin shows stellar masses:  $10.5 < \log(M_*/M_\odot)$ .

Similar to the bottom panel of Fig. 3.4, Fig. G.1 shows the SF mode distribution for each merger stage coloured by late-(blue) and early-(orange) type, and separated by stellar mass bin. From top to bottom: low-, medium-, and high-stellar mass bin.

We notice the lack of early-type galaxies at low-mass mergers, as there are not mergers with early-type galaxies at these stellar masses in our parent sample. As we increase the stellar mass bin, early-type mergers appear but there is no strong difference on the trends seen in either of the three stellar mass bins.



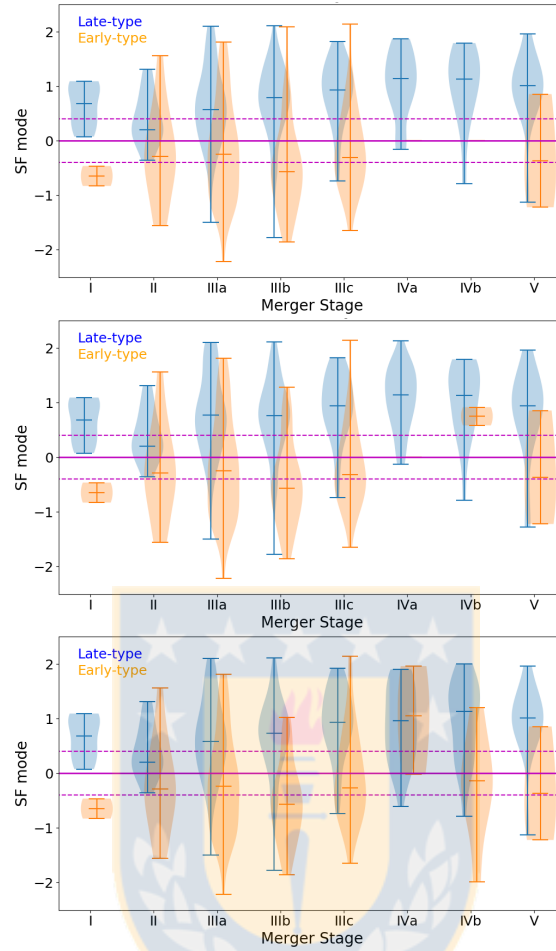


Figure G.1 SF mode at each merger stage separated by  $M_*$  bin. SF mode distribution for each merger stage, coloured by late-(blue) and early-(orange) type. The different sub-panels show the mergers separated by stellar mass bin: low- $M_*$  (top), medium- $M_*$  (middle), and high- $M_*$  (bottom). Credits: Calderón Castillo, P.

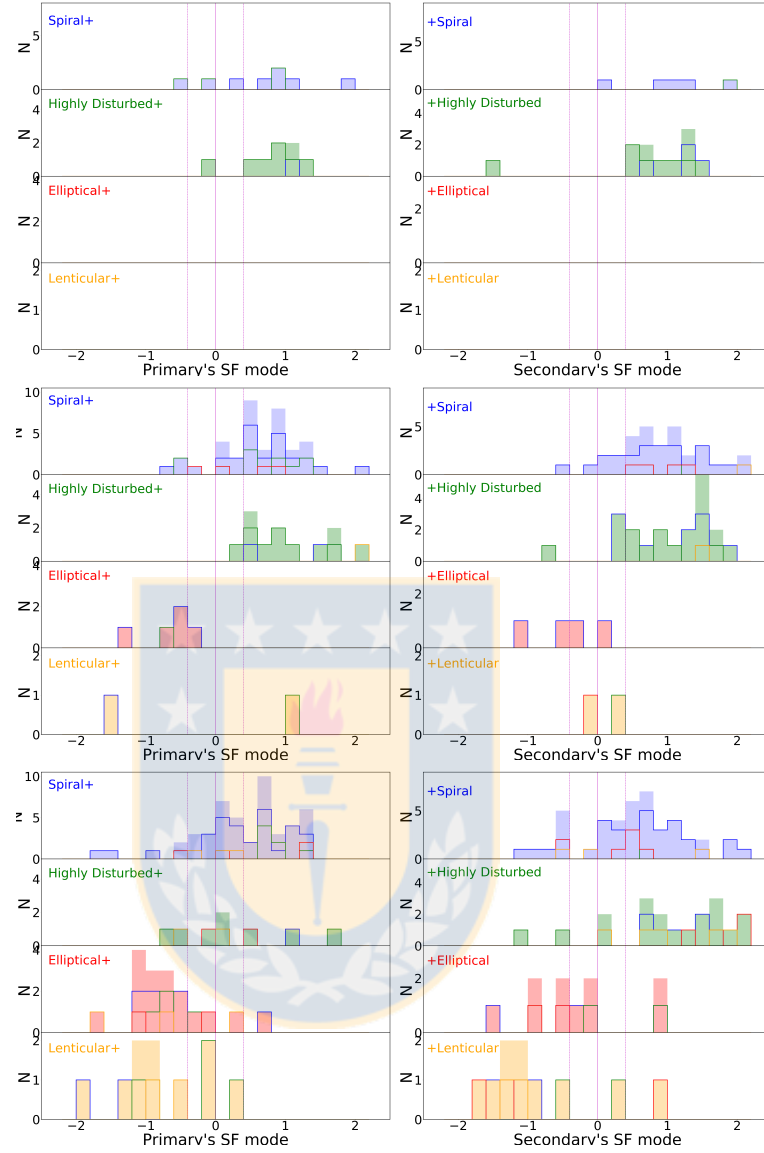


Figure G.2 SF mode for Primary and Secondary separated by  $M_*$  bin. SF mode distribution for the primary (left panels) and secondary (right panels) component, separated by morphology. Top panels show the mergers with low- $M_*$ , middle panels show the mergers with medium- $M_*$ , and the bottom panels show the mergers with high- $M_*$ . Credits: Calderón Castillo, P.



## Testing for dependence on the Stellar Mass ratio of the merging galaxies

### **H.1 Major and Minor Mergers**

Similar to Figure 3.7 but separated by major and minor mergers. Figure H.1 shows the comparison between the SF mode of the primary and the SF mode of the secondary component. Big-unfilled symbols show the morphology of the primary and the small-filled symbols show the morphology of the secondary component as shown in the legend. Major and minor mergers are shown in the left and right panels, respectively. There is no clear dependency on the stellar mass ratio between the components affecting the SF mode for mergers with components of the same morphology. Thus, our results in Sec. 3.3.3 are not affected by the stellar mass ratio between the merger components.

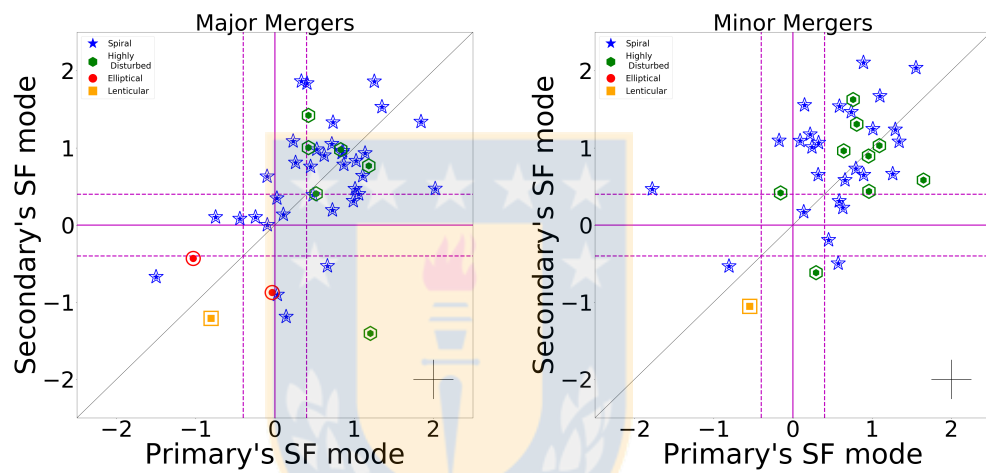


Figure H.1 Primary's SF mode compared to Secondary's SF mode for Major and Minor mergers. Comparison of the SF mode of the primary and the SF mode of the secondary of mergers with components of the same morphology. left and right panels show major and minor mergers, respectively. Coloured symbols show the morphology of the primary as unfilled symbols and the morphology of the secondary as filled symbols. Morphologies are presented in the legend. The solid- and dashed-magenta lines show the MS and the black line shows the one-to-one relation. Credits: Calderón Castillo, P.



# Comparison of AGN Identifiers

## I.1 Comparison of AGN Identifiers

As mentioned previously, we have used three different methods to identify AGNs in mergers. These three methods do not identify the same mergers as they measure different properties of the AGN. In order to show how different these methods perform for mergers, we show where the AGNs identified by one method locate in the other methods diagrams.

Figure I.1 shows the AGNs identified using the BPT-NII in the BPT-NII (top), the HeII diagram (right), and in the WISE diagram (bottom). BPT-NII-selected AGNs are almost completely in the AGN area of the HeII diagram, but they are spread all over the WISE diagram.

Figure I.2 shows the AGNs identified using the BPT-SII in the BPT-SII (top), the HeII diagram (right), and in the WISE diagram (bottom). BPT-SII-selected AGNs are almost completely in the AGN area of the HeII diagram, but they are spread all over the WISE diagram, similar to the BPT-NII-selected AGNs.

Figure I.3 shows the AGNs selected using the HeII diagram in the HeII diagram (top-left), the BPT-NII (top-right), the BPT-SII (bottom-left), and in the WISE diagram (bottom-right). HeII-selected AGNs are spread all over the three other diagrams.

Figure I.4 shows the AGNs selected using the WISE diagram in the WISE diagram (top-left), the BPT-NII (top-right), the BPT-SII (bottom-left), and in the HeII diagram (bottom-right). WISE-selected AGNs are spread all over the three other diagrams, similar to HeII-selected AGNs, except that there are many more objects selected as AGN using HeII compared to WISE-selected AGNs.

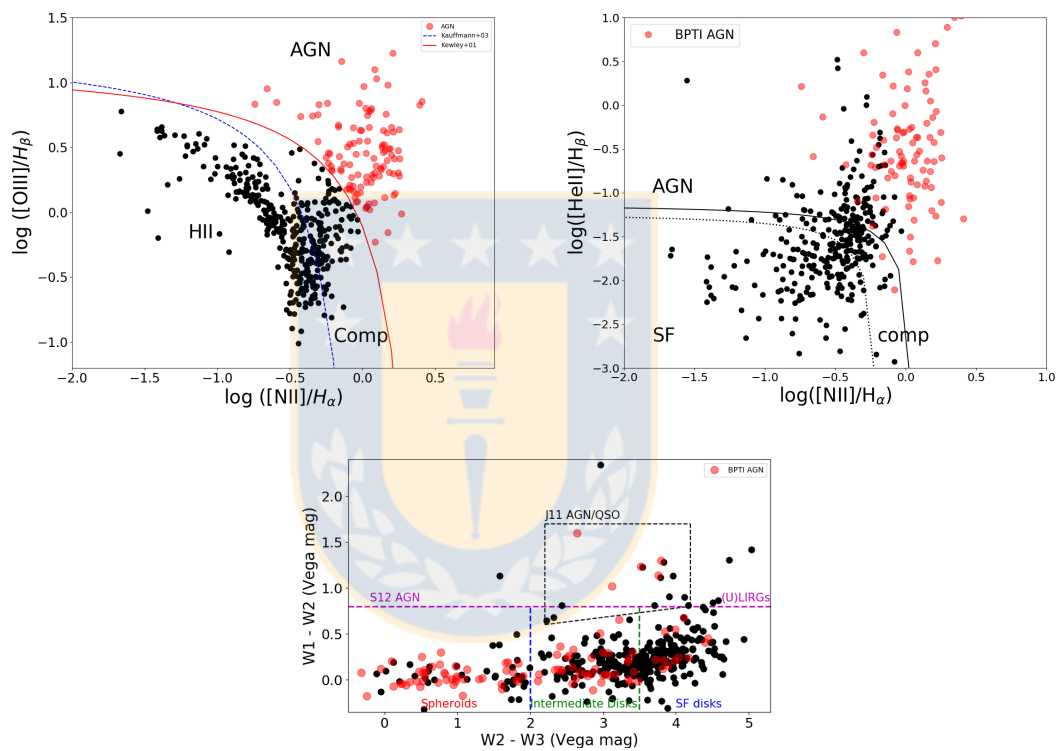


Figure I.1 BPT-NII-identified AGN on different diagrams. BPT-NII-classified AGNs (red circles) shown in the BPT-NII (top), HeII (right) and WISE (bottom) diagram. Credits: Calderón Castillo, P.

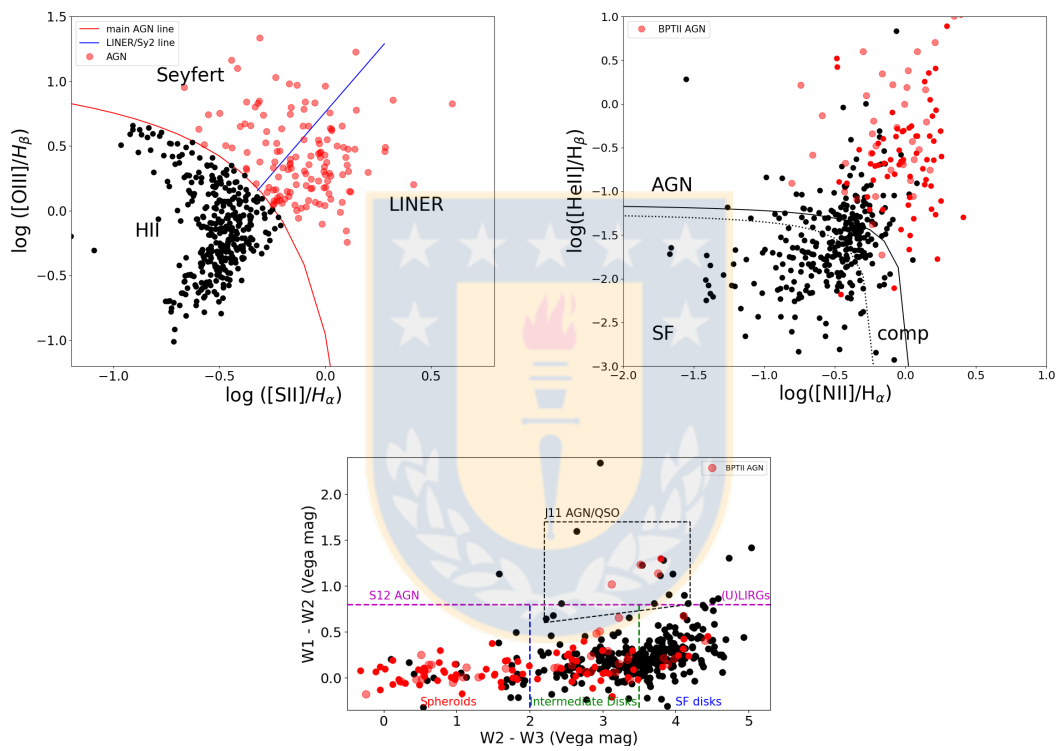


Figure I.2 BPT-SII-identified AGN on different diagrams. BPT-SII-classified AGNs (red circles) shown in the BPT-SII (top), HeII (right) and in the WISE (bottom) diagram. *Credits: Calderón Castillo, P.*

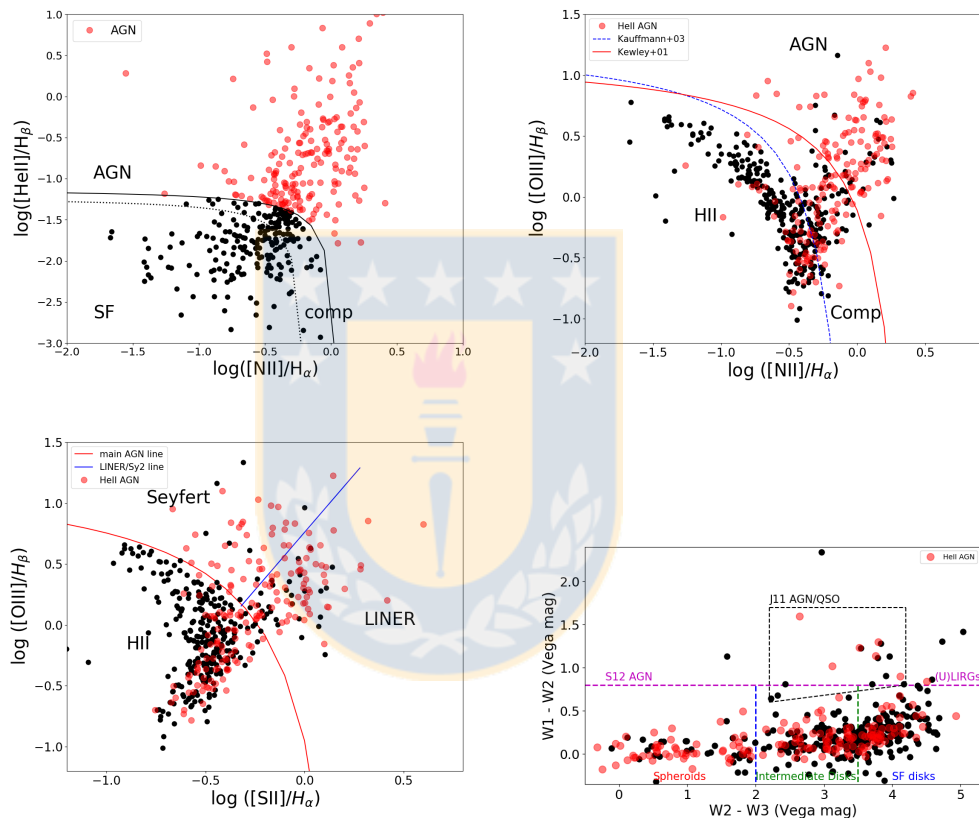


Figure I.3 HeII-identified AGN on different diagrams. HeII-classified AGNs (red circles) shown in the HeII (top-left), BPT-NII (top-right), BPT-SII (bottom-left), and in the WISE (bottom-right) diagram. Credits: Calderón Castillo, P.



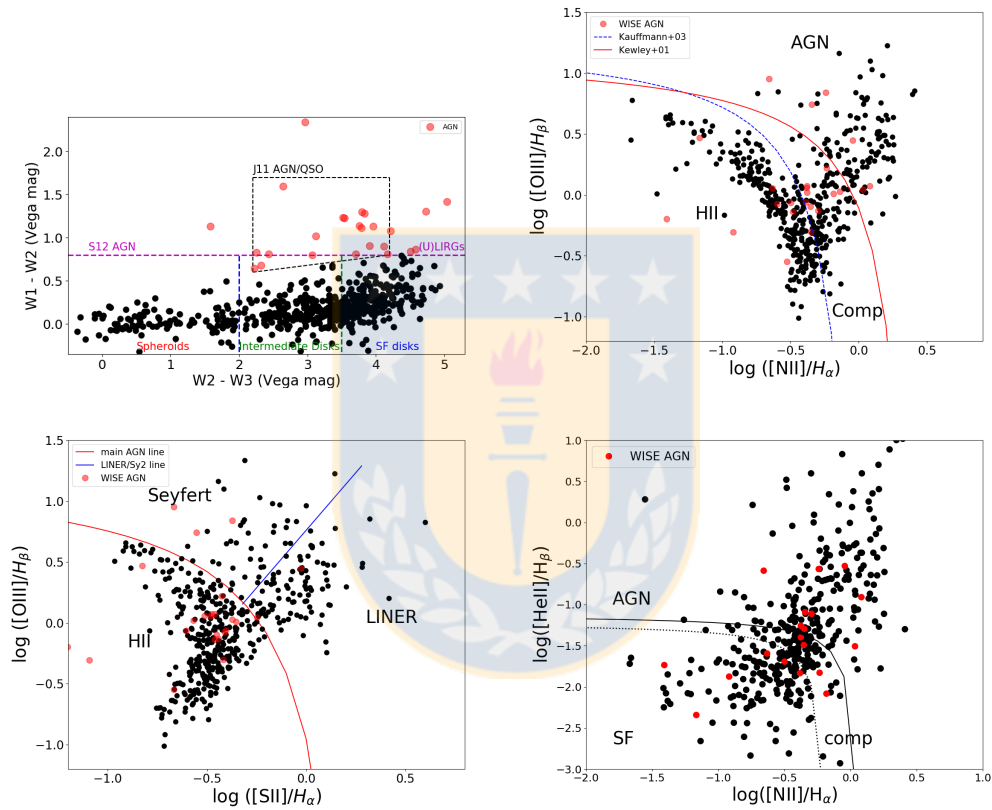


Figure I.4 WISE-identified AGN on different diagrams. WISE-classified AGNs (red circles) shown in the WISE CCD (top-left), BPTI (top-right), BPTII (bottom-left), and HeII (bottom-right) diagram. Credits: Calderón Castillo, P.